POLY(IONIC LIQUID) BLOCK COPOLYMERS AS SOLID POLYMER ELECTROLYTES FOR LITHIUM ION BATTERIES

A Dissertation

by

TZU-LING CHEN

Submitted to the Office of Graduate and Professional Studies of
Texas A&M University
in partial fulfillment of the requirements for the degree of

DOCTOR OF PHILOSOPHY

Chair of Committee,	Yossef A. Elabd
Committee Members,	Jodie L. Lutkenhaus
	Micah J. Green
	Jaime C. Grunlan
Head of Department,	Arul Jayaraman

August 2020

Major Subject: Chemical Engineering

ABSTRACT

Lithium ion batteries are currently the leading commercial technology for portable electronic devices and electric vehicles. However, shortcomings associated with its liquid-based electrolytes, such as leakage, flammability, toxicity, instability, and insufficient overall storage capacity, have limited the progress of the lithium ion batteries. Replacing liquid-based electrolytes with solid polymer electrolytes (SPEs) can alleviate many of these shortcomings, while offering other attractive properties, such as thin-film forming ability and flexibility. Of the SPEs that have been explored for lithium ion batteries, poly(ionic liquid) (PIL) block copolymers are one of the more intriguing materials, which allow for significant changes in physical properties with only subtle changes in chemistry. In this study, SPEs based on PIL block copolymers were developed and investigated for lithium ion batteries. Specifically, structure-property relationships of PIL block copolymer SPEs were systematically explored in relation to ion transport, self-assembled morphology, chemical, thermal, electrochemical stability, and battery performance.

A series of styrene-based PIL diblock copolymers and their analogous PIL homopolymers were synthesized with various ion pairs. This study explores the effect of lithium salt concentration and cation/anion chemistry on the physical, transport, morphological, and electrochemical properties. The result show that the cation/anion chemistry has a significant impact on transport properties, where significant property differences were observed with subtle chemical changes to cation/anion type.

In addition to binary polymer/salt SPE blends, ternary SPE blend was prepared consisting of a PIL multiblock copolymer, ionic liquid (IL), and lithium salt. Two different cations in the PIL block were investigated to understand the influence of cation structure. The results demonstrate that the PIL multiblock SPEs have high potential for lithium ion batteries with outstanding thermal and electrochemical stabilities, as well as high ionic conductivities. Additionally, the influence of IL concentration on ion transport mechanism and electrochemical stability in these ternary SPEs was investigated. Results show that the IL resides in the PIL phase-separated domains and increases the continuous conductive matrix for ion transport, as well as contributes to mechanical percolation. Lithium ion battery with this ternary SPE shows stable cycling performance over 100 cycles under room temperature. The results demonstrate the ion solvation and transport phenomena in ternary SPEs as well as enable the design of new SPEs for room temperature solid-state lithium ion batteries.

Overall, this work elucidated the chemistry-property findings of PIL block polymer SPEs and provides avenues to design and control the SPE with attainable high ionic conductivity and improved stability for the future solid-state lithium ion batteries.

ACKNOWLEDGEMENTS

First and foremost, I would like to thank my advisor, Dr. Yossef A. Elabd for his advice, knowledge, and mentorship during my time here at Texas A&M University while in his research group for the past six years. The constant guidance, encouragement, and attention to details he provided during the time spent together allowed me to become the person and researcher I am today. I thank all past and present members of the Elabd research group for their assistance in the lab and with providing great feedback and conversations, especially Dr. Monica Hwang and Rui Sun. I really appreciate to have them together in this journey. The friendships made with them will never be forgotten.

I thank the members of my dissertation committee for taking the time to meet and review my work. I thank Dr. Carl Willis, Stacy Shingleton and Dr. Bert Krutzer from Kraton Performance Polymers, LLC for their knowledge and synthesis of the materials for my work. I thank Dr. Frederick L. Beyer from Army Research Laboratoy for helping me on X-ray scattering studies.

Lastly, I must thank all my family members and my friends (Chia-Chuan Chen, Hung-Yi Liu, and Liang-Yuan Chiu) who supported me through all the good and rough times over the past six years.

CONTRIBUTORS AND FUNDING SOURCES

Contributors

This work was supervised by a dissertation committee consisting of Professor Yossef A. Elabd, Professor Jodie L. Lutkenhaus, Professor Micah J. Green of the Department of Chemical Engineering and Professor Jaime C. Grunlan of the Department of Mechanical Engineering.

The small-angle X-ray scattering experiments and data analyzed for Chapter 3 and 4 were provided by Dr. Brian Morgan and Dr. Fredrick L. Beyer (U.S. Army Research Laboratory). The pulsed-field gradient nuclear magnetic resonance and self-diffusion coefficient analysis depicted in Chapter 4 were conducted by Dr. Kee Sung Han and Dr. Vijayakumar Murugesan (Pacific Northwest National Laboratory). The synthesis and characterization of diblock copolymers in Chapter 2 were conducted by Patrick M. Lathrop (Elabd Research Group). The pentablock terpolymer precursors in Chapters 3 and 4 were provided by Kraton Polymers, LLC. The homopolymers in Chapter 2, brominated and quaternized pentablock terpolymers in Chapters 3 and 4 were prepared by Rui Sun (Elabd Research Group).

 All other work conducted for the dissertation was completed by the author/student (T.-L.C.) independently.

TABLE OF CONTENTS

LIST OF FIGURES

LIST OF TABLES

CHAPTER I

INTRODUCTION

1.1 Lithium Ion Batteries

Greenhouse gas emissions from internal combustion engines (*e.g.*, passenger cars, trucks, aircraft) contribute to 36.7 % of all greenhouse gas emissions and have increased by 7.5 % over the past five years.[1] This has increased the demand for vehicle electrification (*e.g.*, electric vehicles (EVs), hybrid vehicles (HEVs), and plug-in hybrid electric vehicles (PHEVs)) and the development of more efficient and reliable electrochemical energy storage devices. Since the first commercial rechargeable lithium ion battery released in 1991,[2] lithium ion batteries have been widely used in portable electronics and now are becoming more prevalent in EVs.

However, to utilize lithium ion batteries in EVs, stricter battery safety is required with a wider operational temperature range, which is still limited by the use of flammable organic liquid electrolytes (*e.g.* propylene carbonate (PC), ethylene carbonate (EC), dimethyl carbonate (DMC), ethylmethyl carbonate (EMC),[3] *etc.*). During battery charge-discharge cycles, organic liquid electrolytes result in undesirable solid electrolyte interface (SEI) formation, as well as uncontrollable side reactions with electrodes, and lead to damage and malfunction in the battery along with thermal runaway or explosions.[4] Improving battery safety requires solid polymer electrolytes (SPEs) in lithium ion batteries, which removes the flammable liquid component and creates a stronger mechanical barrier to dendritic lithium formation and short-circuiting.[5-7] Compared with organic liquid

electrolyte solvents, SPEs benefits include: (1) sufficient electrochemical stability, (2) minimal solvent leakage, (3) improved mechanical properties, and (4) prevention of excessive dendritic growth.

Figure 1.1 depicts a conventional lithium ion battery and a lithium ion battery with a SPE (*i.e.*, solid-state battery). The operation of a lithium ion battery is based on the intercalation-deintercalation of Li^+ ions between the electrode materials *via* the ionic conductive electrolyte, while the electrons move *via* the external circuit. Following are the overall reactions of the lithium ion battery with graphite as the anode and lithium cobalt oxide ($LiCoO_2$) as the cathode. Many other electrodes have been used in lithium ion batteries as well.[8-9]

Anode: *6C (graphite)* $+ xLi^+ + xe^- \longleftrightarrow Li_xC_6$ (1.1)

Cathode: $LiCoO_2 \longleftrightarrow Li_{1-x}CoO_2 + xLi + xe^-$ (1.2)

Overall: $6C + LiCoO_2 \longleftrightarrow Li_{1-x}CoO_2 + Li_xC_6$ (1.3)
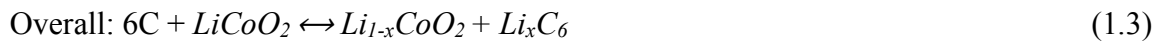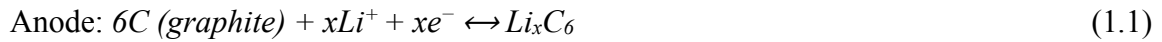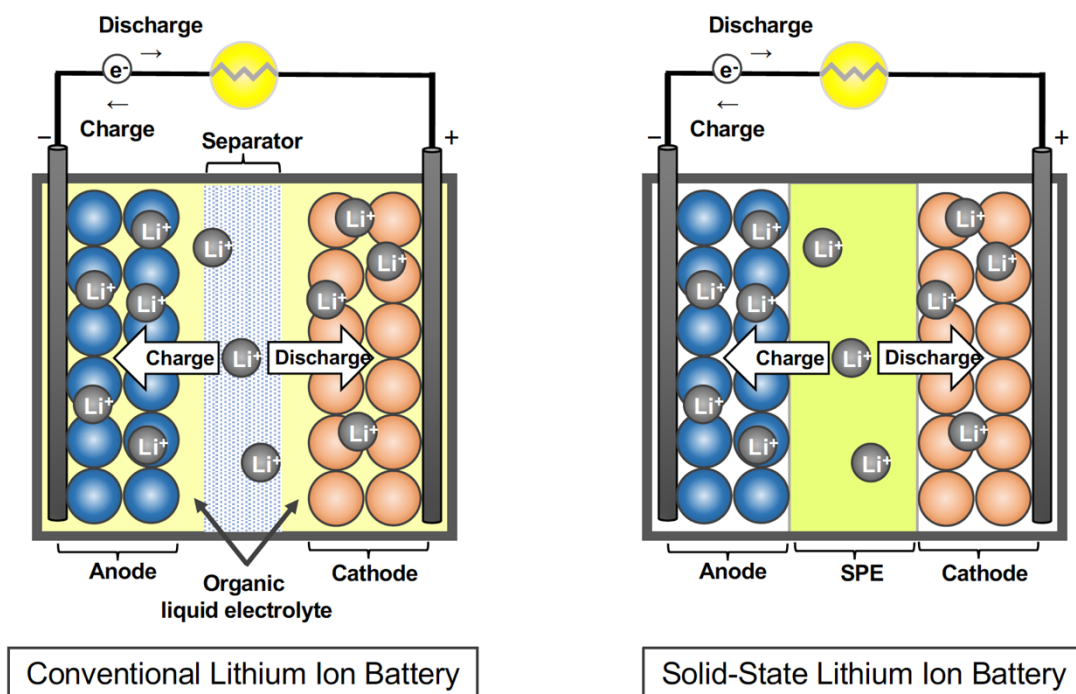
Figure 1.1 Schematic of conventional lithium ion battery (left) and solid-state lithium ion battery (right).

Generally in a solid-state battery, the SPE serves as both the electrolyte and separator (shown in Figure 1.1) and performs three functions: (1) enables Li^+ transport between the electrodes, (2) blocks electron transport between the electrodes, and (3) provides mechanical rigidity to prevent direct contact between the electrodes.[10] The "ideal" SPE for a solid-state battery would possess the high ionic conductivity of a liquid (for high overall storage capacity, energy, and power), high electrochemical stability (for improved power density, stability, and cyclability), the mechanical properties of a solid (for improved stability and cyclability), and the formability of a thermoplastic (for good processability and flexibility). However, compared with liquid electrolytes, SPEs usually

have orders of magnitude lower ionic conductivity (*ca.* $10^{-2} - 10^{-3}$ S cm^{-1} for normal liquid electrolytes *versus* $10^{-5} - 10^{-7}$ S cm^{-1} for SPEs at ambient temperature).[11] Additionally, the macromolecular structure of SPEs also leads to poor contact with electrodes, low cation mobility, and interfacial instability, which results in unstable cycling performance and low capacity.

Since the first SPE was discovered in 1973 (*i.e.*, alkali metal salt /poly(ethylene oxide) (PEO) complex),[12] researchers have synthesized and characterized new materials based on various chemistries to improve both the ionic conductivity and the electrochemical stability of SPEs. Developing the fundamental understanding of ion transport mechanisms, ion association-dissociation, and chemical structure correlations are key factors in SPE research with the goal of providing valuable insights into the design of enhanced SPEs for lithium ion batteries. SPEs, such as conventional PEO-based electrolytes, block copolymer-based electrolytes, and poly(ionic liquids) (PILs) will be briefly introduced in the following section.

1.2 Solid Polymer Electrolytes for Lithium Ion Batteries

Conventional SPEs are formed by adding lithium salts, such as lithium hexafluorophosphate (LiPF$_6$),[13-14] lithium perchlorate (LiClO$_4$),[15-16] lithium tetrafluoroborate (LiBF$_4$),[14, 17] and lithium bis(trifluorosulfonyl)imide (Li-TFSI),[18-20] to PEO. PEO has a significant solubility for lithium salts, comparatively low glass transition temperature (T$_g$ $\approx$ −60 ºC), relatively low dielectric constant (ε_r $\approx$ 5) in comparison with many other polymers; therefore, PEO-based SPEs have been the most extensively studied

SPE.[7] However, the crystalline phase of PEO interferes with ion transport and affects the ionic conductivity at temperatures below its melting temperature (*ca.* 65 °C) resulting in low ionic conductivity (*ca.* < 10^{-4} S cm^{-1}) at room temperature.[21-22] In the PEO matrix, ionic mobility occurs predominantly in the amorphous phase of PEO and is highly dominated by PEO chain segmental motion.[23-24] Above the melting temperature, the ionic conductivity increases but also exhibits lower robustness (*i.e.,* mechanical modulus). Approaches to suppress crystallinity, such as adding additives (*e.g.*, plasticizers[25-27] and nanofillers[28-30]) can result in deterioration of mechanical properties, while other methods, such as grafting and crosslinking result in a decrease of conductivity.[31-32]

One approach to prevent crystallization and improve the mechanical properties is to incorporate a mechanical reinforcement *via* a block copolymer architecture (*i.e.,* addition of another chemistry in a block copolymer, such as polystyrene (PS) and poly(methyl methacrylate) (PMMA)[33] with PEO). In pursuit of orthogonal properties, such as high mechanical modulus and high ionic conductivity, block copolymers with two functional polymers covalently linked on the backbone have also been investigated as SPEs.[34] SPEs composed of block copolymers incorporating lithium salts can induce microphase separation and create a variety of different nanostructures (*e.g.*, body-centered cubic spheres, hexagonally packed cylinders, lamellae, bicontinuous network) that are beneficial for ion transport (*i.e.*, provides mechanical rigidity in a highly conductive ordered nanostructured morphology). PEO based block copolymer SPEs, such as polystyrene-block-poly(ethylene oxide) (PS-*b*-PEO or SEO),[35-37] and poly(ε-caprolactone)-block-poly(ethylene oxide) (PCL-*b*-PEO)[38] have resulted in various nanoscale morphologies.

5

One example that has been widely studied is PS-*b*-PEO block polymer (SEO) doped with lithium salts; while in such SPEs the PS block provides mechanical stiffness, and the PEO block solvates and transports ions from lithium salts.[39-47] Epps and coworkers[46-47] explored lithium salt-doped SEO and showed that the geometry of the conducting channels and their orientation can highly affect the conductivity, specifically the continuity of conducting channel across the gain boundary between block copolymer domains was an important factor contributing to overall ion conduction. Although some of the morphologies can benefit ion transport, most of the PEO-based block copolymer SPEs still suffer from insufficient ionic conductivity, due to the non-monotonic trend of conductivity as a function of salt concentration[35, 39] (*i.e.*, limitation on conductivity), and the relatively higher glass transition temperature (T_g) (*i.e.*, $10 - 20$ ºC) when salt-doped. Recently, a new class of materials referred to as poly(ionic liquids) (PILs) has garnered significant interest as SPEs, which will be introduced and discussed in the following section.

1.3 Poly(Ionic Liquids) and Poly(Ionic Liquid) Block Copolymers

PILs are polymeric form of ILs, where IL moieties are covalently attached to each unit of the polymer chain and neutralized by mobile counterions.[48] PILs are a novel class of materials and have been extensively studied for a wide-range of electrochemical devices, such as lithium batteries, dye-sensitized solar cells, fuel cells, supercapacitors, light-emitting electrochemical cells, and field effect transistors.[49-50] Similar to ILs, PILs possess a number of unique physicochemical properties, such as high ionic conductivity, high

chemical, and thermal stability, nonvolatility, nonflammability, and a widely tunable chemical platform, which allows for significant changes in physical properties with only subtle changes in chemistry.[51]

The structural parameters of PILs that influence the ion conductivity, include types of IL monomers (backbone), cations, anions, as well as the spacer length between the backbone and the cation. The following section focuses on the discussion of several cation/anion chemistries that affect the PIL properties.

1.3.1 Cation and Anion Chemistries in PILs

One of the promising advantages enabling the versatility of PILs is their tunable properties, which can be manipulated by the numerous cation and anion chemistries that are available.[52-53] While the PILs share similar features as ILs, the choice of cation and anion types play an important role in determining ion dynamics and ionic conductivity. In PILs, the ion association and dissociation can be influenced by both the charge delocalization and the interaction energy between the ion pairs.

The cation nature and the polymer side-chain length both play an important role in determining ionic conductivity.[54-55] PILs with quaternary ammonium and *N*-heterocyclic ring cations (*e.g.*, imidazolium, pyridinium, and pyrrolidinium) with different side-chain length have been investigated regarding ionic conductivity.[56-58] The change of side alkyl chain from methyl to butyl group results in the improvement of conductivity from one to two orders of magnitudes in different cation systems.[59-61] PILs with imidazolium cation have attracted extensive attention due to its delocalized positive charge on the aromatic

ring and exhibits higher ionic conductivity compared to pyrrolinium, pyrrolidinium, tetraalkylammonium and piperidinium.[50] Recently, pyrrolidinium-based PILs have shown to be mechanically and electrochemically stable polymer electrolytes for lithium ion batteries with a wider cathodic limit potential compared to imidazolium-based PILs (-3.2 V *versus* -2.5 V).[62-63] Study conducted by Mecerreyes *et al.*[64] also showed that pyrrolidinium-based PILs possess an electrochemical window up to 7.0 V *versus* Li/Li$^+$.

In both ILs and PILs, counter-ion (*i.e.*, for polycation-type PIL, the anions) characteristics direct the physical properties and the Coulombic interactions among ions, as well as the segmental mobility. Anion exchange is an efficient method to modify the *N*-vinylimidazolium-based IL monomers with desiring anion group.[65-66] To date, extensive studies have demonstrated the influence of anion types on the PIL conductivity.[67] Mecerreyes and co-workers[68] compared the conductivities of poly(1-ethyl-3-vinylimidazolium) PILs with various anions: tetrafluoroborate (BF$_4^-$), hexafluorophosphate (PF$_6^-$) and bis(trifluoromethanesulfonimide) (TFSI$^-$). Elabd and co-workers[66] studied PILs with poly(1-[(2-methacryloyloxy) ethyl]-3-butylimidazolium and various fluoride-containing anions (*e.g.*, TFSI$^-$, BF$_4^-$, PF$_6^-$, and trifluoromethanesulfonate (TfO$^-$)). Both of the studies showed that the TFSI$^-$ anion has relatively higher ionic conductivity due to its highly delocalized and lower coordinative properties. Recent works by Zhou *et al.*[60, 69] and Forsyth *et al.*[70] showed that PILs with bis(fluorosulfonyl)imide (FSI$^-$), which is an analog to TFSI$^-$, but with a smaller size and lower T$_g$, can have better compatibility with electrodes and good electrochemical stability with lithium metal, *i.e.*, FSI$^-$ is a promising anion candidate for PILs.

Additionally, in PIL systems, ion transport is governed by a polymer chain segmental dynamics assisted by hopping mechanism and ion pair association.[71] Studies conducted by Winey *et al.*[56] investigated the ion conduction of PILs with different cation/anion chemistries and quantified the correlation lengths between cation-to-cation, anion-to-anion, and side group-to-side group *via* X-ray scattering. Their results revealed that ionic conductivity decreased one order of magnitude, while the cation-to-cation spacing increased 3-fold, suggesting a strong correlation between cation-cation spacing and intermolecular anion hopping. In another study,[72] they compared electron-rich trisaminocyckipropenium (TAC) cation-based PILs with different counterions (chloride (Cl^-), $TFSI^-$, and pentacarboxycyclopentadienyl ($CPDE^-$)). The CPDE-based PIL showed 4 orders of magnitude lower conductivity compared to that of the Cl-based and TFSI-based PILs at their respective glass transition temperatures due to the high segmental rearrangement and the larger molecular volume of the CPDE anion. Both studies highlight the significant change in ion transport by simply manipulating the chain lengths and ion types (*i.e.*, ion-pair interactions) in PILs.

1.3.2 Conductivity-Morphology Relationship in PIL Block Copolymers

PIL block copolymers are promising candidates as SPEs for lithium ion batteries, which combine the properties of both ionic liquids (ILs) and block copolymers (Figure 1.2). Due to the requirements of robustness and processability, PIL block copolymers incorporate another functional polymer block and allow for orthogonal properties to exist, such as high mechanical modulus, high ionic conductivity, flexibility, and processability. As

mentioned above, the block copolymer also self assembles into a variety of different nanostructures that are beneficial for ion transport. Several researchers have investigated the salt-doped block copolymer SPEs and reported that the lithium salts mostly reside in one block (*e.g.,* PEO,[35-37] poly(oligo(oxyethylene)methacrylate) (POEM),[73-74] and poly(methyl methacrylate) (PMMA)[75-76]), resulting in a change of morphology, as well as the conducting pathway. The first PIL block copolymer was reported by Waymouth and coworkers,[77] with imidazolium-functionalized PS diblock copolymers. After that, investigators have explored PIL block copolymer properties, such as chemical structure, morphology, ion transport, and mechanical properties. Elabd and co-workers[78] studied the conductivity-morphology relationships in several PIL diblock copolymers, poly(styrene-*b*-1-((2-acryloxy)ethyl)-3-butylimidazolium bis(trifluoromethansulfonyl)imide (poly(S-b-AEBIm-TFSI)),[79] poly(methyl methacrylate-*b*-1-((2-acryloxy)ethyl)-3-butylimidazolium bis(trifluoromethansulfonyl)imide (poly(MMA-b-MEBIm-TFSI)),[80] and poly(styrene-*b*-4-vinylbenzyl hexylimidazolium bis(trifluoromethansulfonyl)imide (poly(S-b-VBHexIm-TFSI)) by varying the PIL composition. All the results showed that the PIL block copolymers with strong microphase separation reveal one to two orders of magnitude higher conductivity than PIL block copolymers with weaker microphase separation, suggesting that connectivity and orientation of conducting microdomain plays an important role on ion conduction.

Although many studies have investigated the morphology and physicochemical properties of PIL block copolymers, only few studies explored them as SPEs in actual lithium batteries (*i.e.,* binary salt/PIL block copolymer or ternary salt/IL/PIL block

copolymers). The sections below highlight recent literature on SPEs based on PIL and PIL block copolymers.
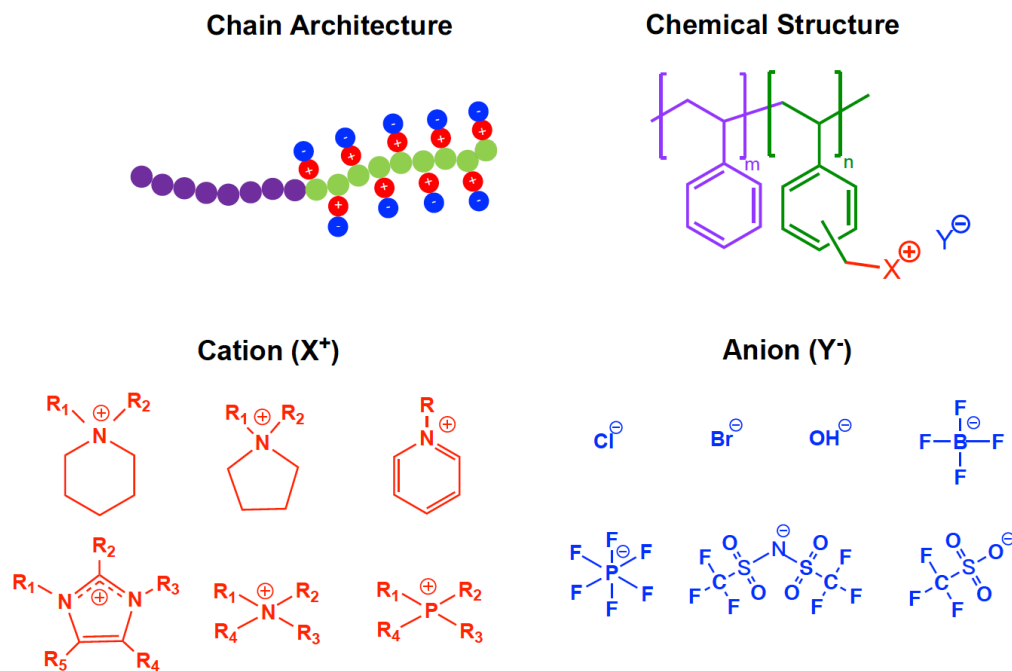
Figure 1.2 PIL block copolymer: (upper left) illustration of polymer chain architecture, (upper right) example chemical structure, (lower left) example cations, (lower right) example anions.

1.4 PIL and PIL Block Copolymers as SPEs

In general, the application of PIL and PIL block copolymers in lithium ion batteries requires a blend of polymer with lithium salt. Therefore, understanding of the ion association-dissociation and physicochemical properties in such binary/ternary system is important for the design of reliable SPEs for lithium ion batteries. Currently, investigators have studied several SPEs based on PIL and PIL block copolymers with improved ionic

conductivity and promising battery performance. Yang et al.[81] prepared a series of guanidinium-based PILs due to the low viscosity and broad electrochemical window of guanidinium-based ILs. The guanidinium-based PIL with BF_4^- showed an ionic conductivity value of 1.3×10^{-4} S cm^{-1} at 30 °C. Zhang et al.[60, 69, 82] synthesized PILs with different cations and pendent groups along with FSI$^-$. The PILs with FSI$^-$ and lithium salt reached ionic conductivity up to 10^{-5} S cm^{-1} at 30 °C, which is one to two orders of magnitude higher than that of corresponding TFSI$^-$ containing PILs. He et al.[83] used imidazolium-functionalized norbornene and benzene-functionalized norbornene to synthesized PIL block copolymer, poly(5-norbornene-2-methylbenzoate-b-5-norbornene-2-carboxylate-1-hexyl-3-methylimidazolium bis[(trifluoromethyl)sulfonyl]amide), P(NPh-b-NIm-TFSI). The composite electrolyte prepared from blending P(NPh-b-NIm-TFSI) with Li-TFSI and nanosilica achieved ionic conductivity value of 7.7×10^{-5} S cm^{-1} at 25 °C. Very recently, Zhang et al.[84] synthesized PIL block copolymer, poly(N-(1-vinylimidazolium-3-butyl)-ammonium bis(trifluoromethanesulfonyl)imide)-b-poly(poly(ethylene glycol) methyl ether methacrylate) (PVIMTFSI-b-PPEGM), and its corresponding all-solid electrolyte (PVIMTFSI-b-PPEGM/Li-TFSI). The electrolyte was tested in a lithium iron phosphate (LiFePO$_4$)/Li battery with a discharge capacity of 136 mAh g^{-1} at 0.1 C at 60 °C.

In pursuit of high ionic conductivity, ILs can also be added as the plasticizers in the polymer electrolyte mixture due to its low glass transition temperature and high chemical affinity with the PILs. Appetecchi et al.[62] prepared a ternary SPE based on poly(diallyldimethylammonium) bis(trifluoromethanesulfonyl)imide PIL and 1-butyl-1-

methylpyrrolidinium bis(trifluoromethylsulfonyl)imide (PYR_{14}-TFSI) IL with Li-TFSI salt. The SPE with 60 wt% IL exhibited a promising ionic conductivity of 0.5 mS cm^{-1} and cycling performance in a $LiFePO_4$/Li battery with a discharge capacity above 140 mAh g^{-1} at C/5 at 40 ºC. Li *et al.*[85] studied a SPE composed of poly((4-vinylbenzyl)trimethylammonium bis(trifluoromethylsulfonyl)imide) (PVB-TFSI) PIL, *N,N*-diethyl-*N*-methyl-*N*-(2-methoxyethyl)ammonium bis(trifluoromethylsulfonyl)imide (DEME-TFSI) IL, Li-TFSI, and silica. The SPE with 60 wt% (IL to PIL) exhibited a high ionic conductivity value of 0.758 mS cm^{-1} and cycling performance in a $LiFePO_4$/Li battery with a discharge capacity above 130 mAh g^{-1} at C/10 at 60 ºC.

Although literature on lithium ion batteries with SPEs based on binary and ternary based PIL homopolymer blends are increasing, there are limited SPE studies based on PIL block copolymers. One recent example of a PIL block copolymer SPE, includes the work of Nykaza *et al.*,[86] where they produced ternary SPEs with poly(methyl methacrylate-*b*-1-[(2-methacryloyloxy)undecyl]-3-butylimidazolium bis(trifluoromethane)sulfonamide) (poly(MMA-*b*-MUBIm-TFSI)), 1-ethyl-3-methylimidazolium bis(trifluoromethylsulfonyl)imide (EMIm-TFSI) IL, and Li-TFSI. The resulting SPEs possessed ionic conductivities as high as 1 mS cm^{-1} at 25 °C and 10 mS cm^{-1} at 105 °C, as well as a maximum discharge capacity of 112 mAh g^{-1} at 0.1 C over 100 cycles at room temperature in the $LiCoO_2$/lithium titanate ($LiTi_5O_{12}$) battery. Very recently, Goujon *et al.*[87] prepared mechanically robust SPEs consisting of poly(styrene-*b*-1-((2-acryloyloxy)ethyl)-3-butylimidazolium bis(trifluoromethanesulfonyl)imide) (S-PIL$_{64-16}$) PIL block copolymer, *N*-propyl-*N*-methylpyrrolidinium bis(fluorosulfonyl)imide

(C3mpyrFSI) IL and Li-FSI salt. The addition of IL to the pristine PIL block copolymer achieved one order of magnitude increase in ionic conductivity at 50 ºC. The cycling performance in a LiFePO$_4$/Li battery reached a capacity of 167 mAh g^{-1} for the first cycle at C/20 at 50 ºC. Examples of lithium battery performances of PILs and PIL block copolymers as SPEs are summarized in Table 1.1.

Table 1.1 Examples of lithium battery performances of PILs and PIL block copolymers as SPEs.

SPE	σ (S cm^{-1})	Cell type	Cell performance	Operating temperature (ºC)	Ref.
PDDA-TFSI/ PYR$_{14}$-TFSI/Li-TFSI	0.5 mS cm^{-1} (40 ºC)	Li/LFP	140 mAh g^{-1} at C/5	40 ºC	[62]
PVE-TFSI/BMMIM-TFSI/Li-TFSI	1.07 mS cm^{-1} (60 ºC)	Li/LFP	146 mAh g^{-1} at C/10 after 100 cycles	60 ºC	[88]
PVB-TFSI/DEME-TFSI/Li-TFSI	0.76 mS cm^{-1} (60 ºC)	Li/LFP	134 mAh g^{-1} at C/10 after 50 cycles	60 ºC	[85]
PDADMA-TFSI/EMIM-TFSI/Li-TFSI	3.4 mS cm^{-1} (25 ºC)	Li/LFP	169.3 mAh g^{-1} at C/10 after 40 cycles	22 ºC	[89]
PDADMA-TFSI/P$_{12}$-FSI/Li-TFSI	0.15 mS cm^{-1} (25 ºC)	Li/LFP	160 mAh g^{-1} at C/5 after 150 cycles	80 ºC	[90]
PMMA-b-PMUBIm-TFSI) /EMIM-TFSI/Li-TFSI	1.0 mS cm^{-1} (25 ºC)	LTO/LCO	112 mAh g^{-1} at C/10	25 ºC	[86]

Table 1.2 Examples of lithium battery performances of PILs and PIL block copolymers as SPEs continued.

SPE	σ (S cm-1)	Cell type	Cell performance	Operating temperature (°C)	Ref.
PVIMTFSI-b-PPEGMA/ Li-TFSI	1.5 mS cm^{-1} (80 °C)	Li/LFP	136 mAh g^{-1} at C/10 after 100 cycles	60 °C	84
S-PIL$_{64-16}$/ PYR$_{13}$-FSI/Li-FSI	6.6 $\times 10^{-3}$ mS cm^{-1} (50 °C)	Li/LFP	163 mAh g^{-1} at C/20	50 °C	87

Even though these studies demonstrate the potential of PIL block copolymer electrolytes as SPEs and separators in lithium batteries, a thorough understanding of the role of chemical structure, lithium salt, and IL composition on physicochemical properties, and specifically the battery performance and stability is still lacking. Additionally, most of the SPE studies only discuss a single chemical structure, specifically, there is little information and research on the comparison of more than two different chemical structures and compositions. The impact of SPE chemistry (*e.g.*, backbone composition, cation/anion structure, salt/IL composition) on ion transport properties and lifetime stability in lithium ion batteries is still unexplored.

1.5 Investigations of Ion Transport in PIL-based SPEs

In battery electrolytes, charge transport not only represents the common factors, *i.e.*, conductivity and mobility, but also include intrinsic processes, such as ion association and

solvation. In the literature, ion interactions (*i.e.*, ion association and dissociation) and transport properties of SPEs primarily have focused on neutral polymers systems (*e.g.*, PEO and SEO as polymer hosts). Studies conducted by Passerini *et al.*[91] analyzed Li^+ coordination at ternary SPE (*i.e.*, PEO + PYR$_{14}$-TFSI + Li-TFSI) *via* Raman spectroscopy and pulsed-field gradient nuclear magnetic resonance (PFG-NMR). The interactions between $Li^+/TFSI^-$ and Li^+/ether oxygen (EO) were quantified by Raman spectroscopy, while the Li^+ mobility was quantified by PFG-NMR. In very recent work, Balsara and coworkers[92] investigated the transport mechanisms in both solid-state salt-doped neutral homopolymer (PEO) and microphase separated block copolymer (SEO) *via* electrochemical methods. The method combined transport parameters from three different measurements to quantify the transference number of polymer electrolytes (*i.e.*, ionic conductivity, mutual salt diffusion coefficient, and cation transference number). Their work developed a framework to investigate the non-ideal, concentrated SPE in a rechargeable battery and enable predictions of the ion transport of any block copolymer electrolyte system.

In spite of the various fundamental studies of ion coordination in neutral polymer SPEs, a thorough study of ion interactions in PIL-based SPEs has yet to be pursued. Compared to neutral polymers, PILs have cations or anions covalently bound to the polymer backbone with mobile counterions. The knowledge gained from studies on neutral polymer SPEs (ion-ion interactions and their coordination with mobile Li^+) cannot simply be transferred to PIL SPEs.

Studies conducted by Ganesan *et al.*[93-95] used atomistic molecular dynamic simulations to investigate the ion transport mechanisms in PIL block copolymers and IL/PIL blends. Their results suggested that the anion-cation correlation and ion transport mechanisms are significantly different from those in neutral polymers. Additionally, there is experimental difficulty regarding high-concentrated solid-state SPEs that limit transport properties measurements.[96] Reliable experimental methods and a systematic investigation are required to elucidate ion transport mechanisms in PIL-based SPEs. Further understanding of ion interactions in SPEs and their influence on battery performance are required for designing reliable SPEs for future lithium batteries.

1.6 Outline and Summary

In this study, SPEs based on PIL block copolymers were developed and investigated for lithium ion batteries. PIL diblock and multiblock copolymers with various cation/anion chemistry and salt/IL composition were studied and compared in relation to ion transport, self-assembled morphology, chemical, thermal and electrochemical stability, as well as battery performance.

In Chapter II, a series of styrene-based PIL diblock copolymers and their analogous PIL homopolymers were synthesized with various covalently attached cations (methylimidazolium (MIm^+) and methylpyrrolidinium ($MPyr^+$)) and counter-anions ($TFSI^-$ and FSI^-). Electrolytes were prepared by mixing the polymer with the corresponding salts (Li-TFSI and Li-FSI) under various salt concentrations. The impacts

of lithium salt concentration and cation/anion chemistry were explored in regards to ion transport, morphology, and electrochemical stability.

Chapter III focuses on a PIL ABCBA pentablock terpolymer (PILPTP) as lithium ion conducting ternary SPEs. The ABCBA pentablock terpolymer was brominated and quaternized to covalently attach two different cations (MIm$^+$ and MPyr$^+$) to form two different TFSI-exchanged PILPTPs (MPyr-TFSI and MIm-TFSI). SPEs were then fabricated by immersing transparent PILPTP thin films into a 1 M Li-TFSI/IL mixture to form ternary blend SPEs. The impacts of different cations (imidazolium and pyrrolidinium) were investigated to understand the influence of cation structure (specifically saturated *versus* unsaturated heterocyclic structure) on the electrochemical stability, ion conductivity, thermal stability, and mechanical properties.

In Chapter IV, the similar lithium ion conducting ternary PILPTP SPEs as Chapter III were investigated with the goal of understanding the influence of IL concentration on ion transport mechanisms and electrochemical stability. The impact of imidazolium-based IL (*i.e.*, EMIm-TFSI) is explored in regards to ion transport, morphology, mechanical properties, electrochemical stability, and battery performance.

Chapter V concludes with a summary of the contributions of this dissertation towards the insights of the various factors (*i.e.*, cation/anion chemistry, salt/IL concentration, and backbone composition) in the PIL block polymer SPEs, which can enable the design of new SPEs with both high ionic conductivity and improved stability for future lithium batteries, as well as proposed directions for future work.

CHAPTER II

LITHIUM ION TRANSPORT IN POLY(IONIC LIQUID) DIBLOCK COPOLYMER ELECTROLYTES: IMPACTS OF SALT CONCENTRATION AND CATION AND ANION CHEMISTRY

2.1 Introduction

In battery electrolytes, the transference number is defined as the number of moles of lithium transferred by migration per Faraday of charge.[7] SPEs with low lithium cation transference number are unfavorable due to the buildup of high concentration gradient during cycling and leads to precipitation at the anode, voltage loss, high interfacial resistance, or even battery failure. While the ionic conductivity and diffusion coefficient are relatively easier to obtain, measuring an accurate transference number in the SPE is usually more difficult. The conventional Bruce-Vincent method[97] is frequently used for measuring the transference number of polymer electrolytes due to its simplicity. However, it was designed for binary ideal dilute electrolyte systems, which assumes that ions are fully-dissociated, *i.e.,* without ion association in the electrolyte. Therefore, the non-ideal nature and high salt concentration of most SPEs could result in an overestimation when using the Bruce-Vincent method. Accordingly, Newman and Blasara[92, 98-100] developed a galvanostatic polarization method to measure the transference number for non-ideal, concentrated polymer electrolytes. The method combines transport parameters from three different measurements to quantify the transference number of polymer electrolytes: ionic conductivity from impedance spectroscopy, mutual salt diffusion coefficient from

restricted diffusion, and cation transference number from the Bruce-Vincent method, which provides a more realistic transference number for SPEs.

As mentioned in Chapter I, investigating ion transport properties in the salt-doped PIL block copolymer SPE requires the consideration of both salt concentration effects and cation/anion correlations. However, to the best of our knowledge, a thorough study of ion conduction in salt-doped PIL block copolymer SPEs for lithium ion batteries is absent in the literature.

In this study, we prepared a series of styrene-based PIL diblock copolymers and their analogous PIL homopolymers with various covalently attached cations (MIm$^+$ and MPyr$^+$) and counter-anions (TFSI$^-$ and FSI$^-$). SPEs were prepared by mixing the polymer with corresponding salt (Li-TFSI or Li-FSI) over a wide range of salt concentrations. The impacts of lithium salt concentration and cation/anion chemistry were explored in relation to ion transport, morphology, and electrochemical stability. The ion transport measurements (*i.e.*, salt diffusion coefficient and lithium transference number) were inspired by Newman and Balsara.[92, 98-99, 101]

2.2 Experimental Methods

2.2.1 Materials

Bis(fluorosulfonyl)imide lithium salt (Li-FSI; 98.0%) was used as received from TCI America. Acetone (ACS reagent, ≥99.5%), bis(trifluoromethylsulfonyl)imide lithium salt (Li-TFSI; 99.95%), were used as received from Sigma-Aldrich. Lithium ribbon (0.38 mm

× 23 mm, 99.9%) was purchased from Sigma-Aldrich and stored in argon-filled glove box (mBraun) before use. CR2032 coin cell cases (20 mm diameter × 3.2 mm thickness) with O-rings for battery research, stainless steel spacers for CR2032 cells (15.5 mm diameter × 0.5 mm thickness, 15.5 mm diameter × 0.2 mm thickness), and stainless steel wave springs for CR2032 cases (1.2 mm height × 0.3mm thickness) were used as received from MTI Corporation. Mylar PET release liner substrates (Grade 26965, 0.0762 mm) were used as received from LOPAREX. Deionized (DI) water with resistivity *ca.* 16 MΩ cm was used as appropriate.

2.2.2 Polymer Synthesis and Characterization

The PIL diblock copolymers, poly(S-*b*-VBMIm-TFSI) [VBMIm-TFSI = vinylbenzylmethylimidazolium bis(trifluoromethylsulfonyl)imide], poly(S-*b*-VBMIm-FSI) [VBMIm-FSI = vinylbenzylmethylimidazolium bis(fluorosulfonyl)imide], poly(S-*b*-VBMPyr-TFSI) [VBMPyr-TFSI = vinylbenzylmethylpyrrolidinium bis(trifluoromethylsulfonyl)imide], and poly(S-*b*-VBMPyr-FSI) [VBMPyr-FSI = vinylbenzylmethylpyrrolidinium bis(fluorosulfonyl)imide] were synthesized and characterized using methods described in Appendix A (Table 2.1). The PIL homopolymers, poly(VBMIm-TFSI), poly(VBMIm-FSI), poly(VBMPyr-TFSI), and poly(VBMPyr-FSI), were synthesized and characterized using method described in ref [102]. The volume fractions corresponding to the PIL composition in each PIL diblock copolymer were calculated using this equation:

$$\phi_{c,PIL} = x_{PIL} \frac{MW_{IL}}{MW_{cp}} \frac{\rho_{cp}}{\rho_{IL}} \tag{2.1}$$

where x_{PIL} is the PIL composition (mole fraction) in the PIL diblock copolymer determined from NMR, MW_{cp} is the average molecular weight of the repeat unit of the copolymer, and MW_{IL} is the molecular weight of IL monomeric unit ($MW_{VBMIm-TFSI}$ = 479.42 g mol^{-1}, $MW_{VBMIm-FSI}$ = 379.40 g mol^{-1}, $MW_{VBMPyr-TFSI}$ = 482.46 g mol^{-1}, and $MW_{VBMPyr-FSI}$ = 382.45 g mol^{-1}). The ρ_{cp} is the density of the copolymer, which is given by:

$$\frac{1}{\rho_{cp}} = \frac{w_{PS}}{\rho_{PS}} + \frac{w_{IL}}{\rho_{IL}} \tag{2.2}$$

where w_{PS} and w_{IL} are the weight fraction of polystyrene (PS) and PIL, respectively; and ρ_{PS} and ρ_{IL} are the densities of PS (ρ_{PS} = 1.04 g cm^{-3}) and PIL. The ρ_{IL}s were calculated similar to a procedure developed by Shreeve et al.[103] with $\rho_{VBMIm-TFSI}$ = 1.273 g mol^{-1}, $\rho_{VBMIm-FSI}$ = 1.404 g mol^{-1}, $\rho_{VBMPyr-TFSI}$ = 1.377 g mol^{-1}, and $\rho_{VBMPyr-FSI}$ = 1.246 g mol^{-1}.

Table 2.1 Chemical structure, sample name, acronym, lithium salt concentration r, and conducting volume fraction ϕ_c of PIL diblock copolymer SPEs.
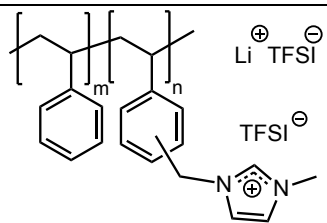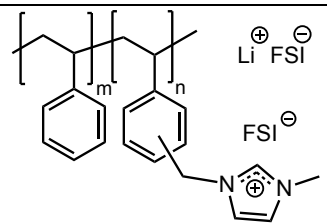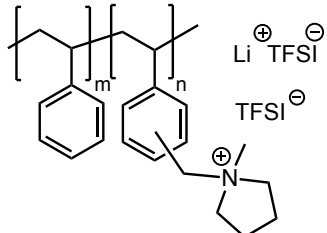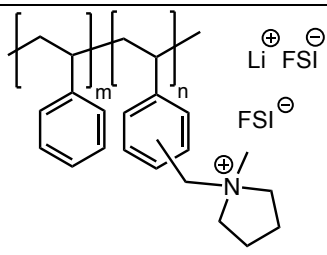
Chemical Structure / Sample Name	Acronym	[a] r	[b] ϕ_c
poly(S-*b*-VBMIm-TFSI) + Li-TFSI	MIm-TFSI+Li-TFSI-0.1	0.1	0.780
	MIm-TFSI+Li-TFSI-0.2	0.2	0.788
	MIm-TFSI+Li-TFSI-0.4	0.4	0.802
	MIm-TFSI+Li-TFSI-0.5	0.5	0.807
	MIm-TFSI+Li-TFSI-0.6	0.6	0.812
	MIm-TFSI+Li-TFSI-0.8	0.8	0.820
poly(S-*b*-VBMIm-TFSI) + Li-FSI	MIm-FSI+Li-FSI-0.5	0.5	0.770
poly(S-*b*-VBMPyr-TFSI) + Li-TFSI	MPry-TFSI+Li-TFSI-0.5	0.5	0.810

Table 2.1 Chemical structure, sample name, acronym, lithium salt concentration r, and conducting volume fraction ϕ_c of PIL diblock copolymer SPEs continued.

Chemical Structure / Sample Name	Acronym	[a] r	[b] ϕ_c
poly(S-*b*-VBMPyr-FSI) + Li-TFSI	MPyr-FSI+Li-FSI-0.5	0.5	0.773

[a] r = [Li]/[PIL] (mol/mol)
[b] ϕ_c = volume fraction of PIL block + salt

2.2.3 Polymer Electrolyte Preparation

The salt-doped PIL diblock copolymer SPEs were first dissolved in acetone at a concentration of 0.43 g mL^{-1} and mixed with the desired proportions of corresponding lithium salts (Li-TFSI or Li-FSI) to obtain various salt concentrations with molar ratio of lithium ions to PIL moieties, r = [Li]/[PIL]. The SPEs used in this study are listed in Table 2.1. The mixture was then mixed for 3 h at room temperature. The free-standing SPEs were then fabricated by casting the mixture solution onto a silicon-coated Mylar PET film using an automatic film applicator (Elcometer 4340) with doctor blade at gauge height and speed of *ca.* 500-800 μm and 60 mm s^{-1}, respectively, under ambient conditions. Polymer solutions were partially covered and allowed to evaporate under ambient conditions for 6

h and then further dried under vacuum for 24 h. The SPE films were then annealing at *ca.* 80-100 °C for two days. The final film thicknesses for ionic conductivity measurement were *ca.* 50-70 μm, while the film thicknesses for lithium symmetric cells were *ca.* 80-110 μm; measured with a digital micrometer (Mitutoyo; ± 0.001 mm accuracy). The films were stored inside an argon-filled glovebox (mBraun) with both water and oxygen concentrations < 5 ppm and environmental pressure between 1-8 mbar. A previous study[104] showed that all of the salt resides in the PIL domain. Therefore, we assume the volume fraction of the conducting phase is the volume of PIL plus salt. The volume fraction of the conducting phase can be determined using

$$\phi_c = \frac{\frac{w_{salt}}{w_{cp}}\frac{\rho_{cp}}{\rho_{salt}}+\phi_{c,PIL}}{1+\frac{w_{salt}}{w_{cp}}\frac{\rho_{cp}}{\rho_{salt}}} \tag{2.3}$$

where ρ_{salt} is the density of lithium salt, w_{salt} and w_{cp} are lithium salt and block copolymer weights in the SPE, respectively. $\phi_{c,PIL}$ is the PIL volume fraction from Equation 2.1. The volume fraction of the conducting phase of the studied SPEs are listed in Table 2.1.

2.2.4 Thermal and Morphological Characterization

Differential scanning calorimetry (DSC) experiments were performed using a differential scanning calorimeter (Q200, TA Instruments) over the temperature range of -140 to 200 °C with the heating rate of 10 °C min^{-1} under nitrogen environment using a heat/cool/heat method. DSC samples were prepared in an argon-purged glovebox (both

water and oxygen concentrations < 5 ppm). Glass transition temperatures (T_gs) were determined from the second thermogram heating cycle by the midpoint method.

Small-angle X-ray scattering (SAXS) data were collected using a Rigaku SMAX-3000 instrument. A rotating copper anode (MicroMax-007HFM, Rigaku) operated at 40 kV and 30 mA was used to generate characteristic Cu X-rays with a wavelength (λ) of 1.542 Å. The X-rays were focused, monochromated, and collimated using a Confocal Max-Flux double-focusing optic and subsequent pinhole collimation. The samples were characterized at a sample-to-detector distance of 1.5 m using a Gabriel-type 2D multi-wire detector. Distance calibrations were performed using silver behenate. SAXS data was collected under vacuum at room temperature with exposure times ranging from 1800 to 3600s. The raw data were corrected for transmission and background noise, then averaged azimuthally to give intensity as a function of momentum transfer magnitude, I(q), where $q = 4\pi (\sin \theta)/\lambda$ and 2θ is the scattering angle. The q range was from 0.007 Å^{-1} to 0.300 Å^{-1}. The intensities were reported in arbitrary units (a.u.).

2.2.5 Electrochemical Characterization

All cells for electrochemical characterization were prepared inside an argon-purged glovebox under room temperature with water and oxygen levels below 5 ppm, respectively. Ionic conductivity was measured with an impedance analyzer (Solartron 1260) and potentiostat/galvanostat (Solartron 1287) inside the glovebox *via* electrochemical impedance spectroscopy. A two-electrode cell was used for ionic conductivity measurements, where samples were sandwiched between two stainless steel

solid blocking electrodes (surface area = 1.2161 ± 0.0015 cm^2) within a sealable Teflon custom-made cell. Impedance scans (Nyquist plots) were measured at 10 mV amplitude over a frequency range of 1 MHz to 1 Hz at open circuit potential at a temperature range of 28 to 97 °C controlled by a heating tape (BriskHeat; XtremeFLEXSDC) and a digital temperature controller with J type thermocouple (OMEGA, Model 650). Samples were equilibrated for at least 1.5 h at each temperature followed by five measurements at the equilibrium condition. Ionic conductivity was calculated by using the following equation: $\sigma = L/AR$, where L and A is the thickness and cross-section area of the SPE, respectively; resistance, R, was determined from the equivalent circuit regression from the Nyquist plot.[105]

Symmetric lithium metal cells were used for restricted diffusion and steady-state transference number measurements. SPE films with thicknesses in the range of 80-110 μm were punched into disks (12 mm in diameter) without any additional preparation before use. Test cells were assembled by sandwiching the samples between two lithium ribbons (8 mm dia.) in a CR2032 coin cell. The coin cells were pressed twice using an electric coin cell crimping machine (MTI Corp., MSK-160D) under argon environment at room temperature to ensure a proper seal. Restricted diffusion and steady-state transference number measurements were conducted using an impedance analyzer (Solartron 1260) and potentiostat/galvanostat (Solartron 1287) under room temperature. Testing procedures were similar to those developed by Newman and Balsara[92, 99] and conducted under room temperature. After assembling, the cells were conditioned for 3 charge/discharge cycles at 0.02 mA cm^{-2} current density for 2 h each. The conditioning cycles ensured that a stable

interfacial layer was formed. Restricted-diffusion measurements were then performed by polarizing cells for 12 min at current density of 0.15 mA cm^{-2}. The open circuit voltage of the cell, U, were monitored at a time interval of 1 s during relaxation for 6 h after interrupting the current. The mutual salt diffusion coefficient, D, was calculated from the slope of negative natural logarithm of U (-ln(U)) *versus* time using the following equation:

$$-\frac{dlnU}{dt} = \frac{\pi^2 D}{L^2}$$
(2.4)

where L is the thickness of the SPE film.

A similar procedure was used for steady-state transference number measurements. AC impedance was measured after the conditioning cycles with an amplitude of 10 mV over a frequency range of 6 MHz to 0.1 Hz. Potentiostatic polarization with amplitude at 10 mV was applied to the testing cell for at least 4 h and monitored until a steady-state current was reached. The equation used to calculate the steady-state transference number, t_{s-s}, is defined by Bruce and Vencent[97]:

$$t_{s-s} = \frac{i_{ss}(\Delta V - i_\Omega R_{i,0})}{i_\Omega(\Delta V - i_{ss}R_{i,ss})}$$
(2.5)

where ΔV is the applied potential, i_{ss} is the current measured at steady-state, $R_{i,0}$ and $R_{i,ss}$ are the initial and steady-state interfacial resistance measured by EIS before and after the polarization, respectively. i_Ω is the initial current calculated using the following equation:

$$i_\Omega = \frac{\Delta V}{R_{i,0} + R_{b,0}}$$
(2.6)

where $R_{i,0}$ and $R_{i,ss}$ are the interfacial and bulk electrolyte resistance measured by EIS prior to polarization, respectively.

The concentration cells were prepared by placing the testing SPE film with the reference SPE film between two lithium ribbons (8 mm dia.). SPE films with different salt concentrations were then pressed and aligned together with the reference SPE film. Both SPE films were sandwiched between the lithium electrodes as Li/SPE-r_1/SPE-r_2/Li and assembled in the stainless-steel solid block within a sealable Teflon custom-made cell. The cell was rested at room temperature for 20 h before the open circuit voltage, U, was measured using potentiostat/galvanostat (Solartron 1287) at time intervals of 1 s for 5 h. The cells were fabricated at a fixed salt concentration (r = [Li]/[PIL] = 0.2 (mol/mol)) as the reference SPE and at various salt concentrations of r = 0.1 to 1.6 as second SPE film. Two to three concentration cells were prepared and measured for each concentration.

The cyclability and stability with lithium metal were evaluated using a battery tester (MACCOR, 4200M) *via* lithium stripping and plating. The test cell was assembled by sandwiching the SPE film between two lithium ribbons (12 mm dia.) using similar assembly process as described above. After assembling, the symmetrical Li/SPE/Li cells were transferred to the battery tester and held at open circuit voltage (OCV) for 24 h prior to testing. The cells were then examined under constant current (0.02 mA cm^{-2}, reversed polarization every 1h) at 70 °C. The interfacial resistance evolution was collected *via* electrochemical impedance spectroscopy with an impedance analyzer every 10th polarization cycle at 10 mV amplitude at a frequency range of 100 kHz to 1 Hz. The obtained spectra were then regressed to an equivalent circuit model described in our previous work.[104]

2.3 Results and Discussion

Figure 2.1 shows the DSC thermograms (glass transition temperatures, T_g, indicated with arrows) for MIm-TFSI+Li-TFSI SPEs with different r (Figure 2.1a) and SPEs with different cation/anion chemistries at r = 0.5 (Figure 2.1b). The values of T_g for the neat PIL diblock copolymers, poly(S-*b*-VBMIm-TFSI) (MIm-TFSI), poly(S-*b*-VBMIm-FSI) (MIm-FSI), poly(S-*b*-VBMPyr-TFSI) (MPyr-TFSI), and poly(S-*b*-VBMPyr-FSI) (MPyr-FSI) are reported in Figure 2.2. In Figure 2.1a, all MIm-TFSI+Li-TFSI SPEs exhibit two T_gs (indicative of phase separation), where the higher T_g is at *ca.* 76-84 °C and this corresponds to polystyrene ($T_{g, PS}$), while the lower T_g corresponds to the PIL ($T_{g, PIL}$). As lithium salt content increases in the MIm-TFSI+Li-TFSI SPEs, the depression of $T_{g, PIL}$ from 30 °C to 12 °C can be observed, while the values of $T_{g, PS}$ are almost unaffected (*ca.* 77 °C), suggesting that the salt mainly resides in the conductive PIL domain. This could be due to the high chemical affinity of salts towards the PIL block compared to the other block, producing SPEs with micro-separated conductive and non-conductive microdomains. The phase selectivity and $T_{g, PIL}$ depression corroborate with other reports on block copolymers with addition of salt, where the salts are selective for one block.[106-107] As seen in Figure 2.1a, the values of $T_{g, PIL}$ decreased from 30 °C for neat polymer (MIm-TFSI) to 16 °C (r = 0.4) with addition of lithium salt, indicating the plasticizing effect of Li-TFSI. However, when the concentration of Li-TFSI is in the range of r > 0.4, the values of $T_{g, PIL}$ only marginally decreased with increasing salt (*e.g.* $T_{g, PIL}$ = 16 °C at r = 0.4 *versus* $T_{g, PIL}$ = 12 °C at r = 0.8). This might due to the restricted segmental motion or the formation of ion aggregates under the higher salt concentration that begins to hinder

chain mobility. This result can also be observed in other polymer/salt mixtures at high salt concentrations.[35] In Figure 2.1b, SPEs with different cation/anion chemistries also exhibit two T_gs, where the higher T_g corresponds to the polystyrene ($T_{g, PS}$) and the lower T_g corresponds to the PIL ($T_{g, PIL}$). The lowest $T_{g, PIL}$ appears at -7 °C for MIm-FSI+LI-FSI-0.5, while MPyr-TFSI+LI-TFSI-0.5 and MPyr-FSI+LI-FSI-0.5 show $T_{g, PIL}$ higher than room temperature at 35 °C and 49 °C, respectively.

Comparing Figure 2.2 with Figure 2.1b, the neat polymers (Figure 2.2) with MIm^+ exhibit lower $T_{g, PIL}$ than that of polymers with $MPyr^+$ (*i.e.*, $T_{g, PIL}$ = 30 °C for MIm-TFSI *versus* $T_{g, PIL}$ = 72 °C for MPyr-TFSI, and $T_{g, PIL}$ = 47 °C for MIm-FSI *versus* $T_{g, PIL}$ ≃ 104 °C for MPyr-FSI). This would be attributed to the delocalized positive charge on the imidazolium ring compared with the localized positive charge on the pyrrolidinium ring that results in the thermodynamic difference, which can also be seen in both ILs and PILs.[108-109] However, interesting to note that in Figure 2.1b, the FSI salt-doped PIL diblock copolymers have a more significant depression of $T_{g, PIL}$ than that of TFSI salt-doped PIL diblock copolymers (*i.e.*, $T_{g, PIL}$ changes from = 47 °C to -7 °C from MIm-FSI to MIm-FSI+Li-FSI-0.5; $T_{g, PIL}$ changes from = 30 °C to 16 °C from MIm-TFSI to MIm-TFSI+Li-TFSI-0.5; $T_{g, PIL}$ changes from = 72 °C to 35 °C for MPyr-TFSI to MPyr-TFSI+Li-TFSI-0.5; $T_{g, PIL}$ change from = 104 °C to 49 °C for MPyr-FSI to MPyr-FSI+Li-FSI-0.5), suggesting that Li-FSI exhibits a greater plasticizing effect compared to Li-TFSI. Similar trends are also reported in the literature.[110-111] The evidence of two distinct T_gs for all the SPEs suggest an ordered microphase separation morphology and can be confirmed with SAXS (Figure 2.3).
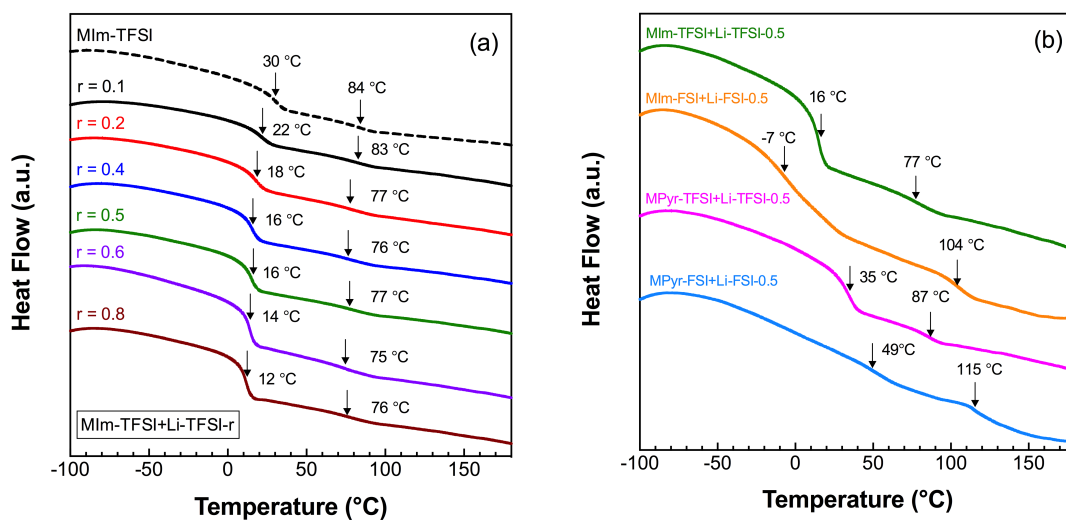
Figure 2.1 Differential scanning calorimetry profiles for all materials. (a) from top to bottom shown are the MIm-TFSI and MIm-TFSI+Li-TFSI-r at different r = [Li]/[PIL] (mol/mol) as indicated and (b) PIL diblock copolymer SPEs with different cation and anion chemistry at r = 0.5.
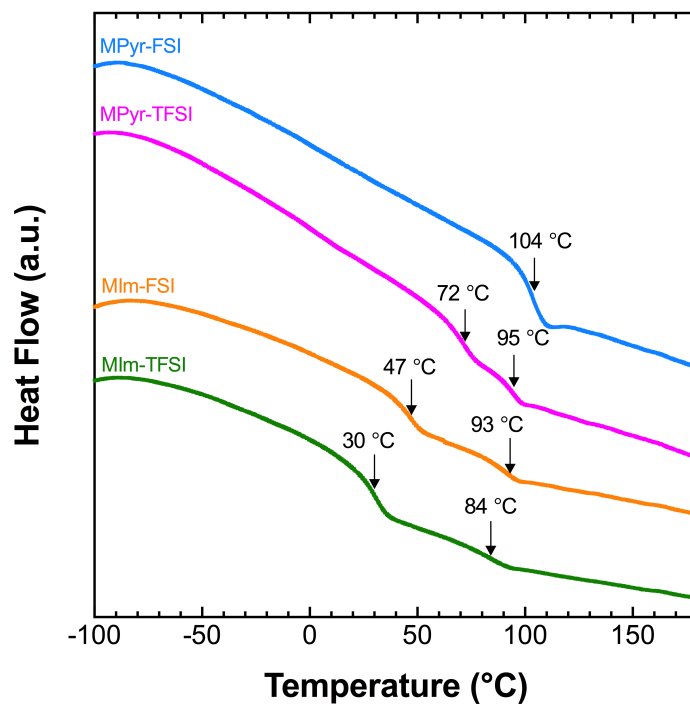
Figure 2.2 Differential scanning calorimetry profiles for neat PIL diblock copolymers.

Figure 2.3 shows the SAXS data for MIm-TFSI and MIm-TFSI+Li-TFSI-r SPEs at r = 0.2, 0.4, 0.5 (Figure 2.3a), and SPEs with different cation/anion chemistries at r = 0.5 (Figure 2.3b). From Figure 2.3a, MIm-TFSI+Li-TFSI-r SPEs show three to four distinct scattering peaks, suggestive of strong periodic microphase separation between the PS and PIL domains, which is in good agreement with the T_g profiles in Figure 2.1a. Additionally, the estimated peak assignments at q*, $\sqrt{4}$ q*, $\sqrt{7}$ q*, and $\sqrt{12}$ q* suggesting the morphology of cylinders on a hexagonal lattice with PS as the cylindrical domain based on the volume fractions in Table 2.1. A weakly ordered hexagonal packed cylinder (HEX) morphology was also observed in the literature for PIL diblock copolymer with similar PS-*b*-PVBmIm-TFSI compositions (*i.e.*, ϕ_c = 0.79).[112] It should be noted that MIm-TFSI+Li-TFSI-0.4 and MIm-TFSI+Li-TFSI-0.5 SPEs possess a stronger $\sqrt{7}$ q* peak than MIm-TFSI and MIm-TFSI+Li-TFSI-0.2 SPEs. The average interdomain spacing, d*, can be directly calculated from the position of the primary scattering maximum, q*, with Bragg's law: d* = 2π/q* (listed in Table 2.2). From Figure 2.3a and Table 2.2, all SPEs remain identical at the positions of the primary scattering peak, q* with relatively constant domain spacings *ca.* 15.8 nm. Therefore, the increasing salt concentration in the MIm-TFSI-based SPE resulted in minimal effects on both $T_{g, PIL}$ (Figure 2.1a) and morphology.

Figure 2.3b shows SAXS profiles of MIm-TFSI+Li-TFSI-0.5, MIm-FSI+Li-FSI-0.5, MPyr-TFSI+Li-TFSI-0.5, and MPyr-FSI+Li-FSI-0.5. The profiles of all samples have three to four distinct scattering peaks, indicative of periodic microphase separation. With the exception of MPyr-FSI+Li-FSI-0.5, there is no observed shift in the primary peak (q*) for MIm-TFSI+Li-TFSI-0.5, MIm-FSI+Li-FSI-0.5, MPyr-TFSI+Li-TFSI-0.5 and the

average interdomain spacing, d*, also remains similar within 0.2 nm variance (*ca.* 15.6 −

15.8 nm; Table 2.2). The estimated peak assignments of MIm-FSI+Li-FSI-0.5 also shows

q*, √4 q*, and √12 q*, suggesting the same PS-rich cylindrical morphology, while the

MPyr-TFSI+Li-TFSI-0.5, and MPyr-FSI+Li-FSI-0.5 show the relatively weaker peak

assignments of q*, √4 q*, √7 q*, and √12 q*. Interestingly, the primary peak of MPyr-

FSI+Li-FSI-0.5 shifts to higher q* and results in a much lower domain spacing (13.86

versus 15.79 nm) compared with others. The difference in domain spacing may due to the

interaction energy of the cation/anion pairs.
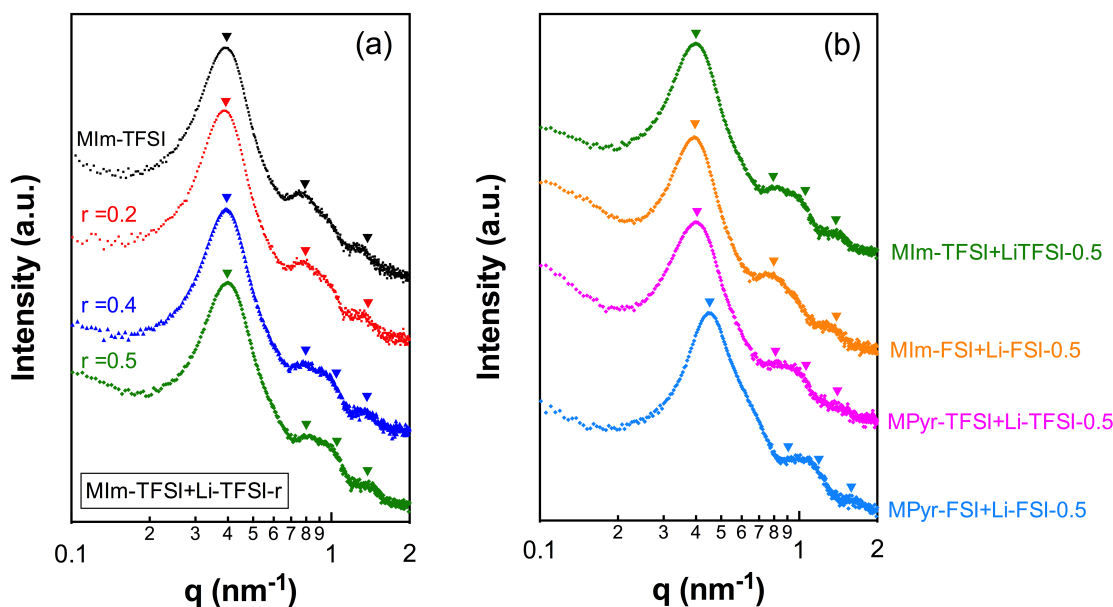
Figure 2.3 Small-angle X-ray scattering (SAXS) profiles at room temperature of (a) MIm-TFSI, MIm-TFSI+Li-TFSI-r SPEs, at r = [Li]/[PVBMIm-TFSI] (mol/mol) = 0.2, 0.4, 0.5, and (b) PIL diblock copolymer SPEs with different cation and anion chemistries as indicated at r = [Li]/[PIL] (mol/mol) = 0.5. Triangle symbols represent the values of a hexagonal packed cylinder (HEX) morphology, at q/q* ratios of √1, √4, √7, and √12.

Table 2.2 SAXS domain spacing, d*, of the studied PIL diblock copolymer SPEs in Figure 2.3

Sample name	d* (nm)
MIm-TFSI	15.86
MIm-TFSI+Li-TFSI-0.2	15.86
MIm-TFSI+Li-TFSI-0.4	15.86
MIm-TFSI+Li-TFSI-0.5	15.71
MIm-FSI+Li-FSI-0.5	15.79
MPyr-TFSI+Li-TFSI-0.5	15.64
MPyr-FSI+Li-FSI-0.5	13.86

Figure 2.4 shows the temperature-dependent (28 to 97 °C) ionic conductivity under a dry condition (in an argon-filled glove box) for PIL homopolymer SPEs (Figure 2.4a) and their analogous PIL diblock copolymer SPEs (Figure 2.4b) with different cation/anion chemistries at r = 0.5. In Figure 2.4a, the homopolymer SPE, poly(VBMIm-TFSI), with the MIm^+ and $TFSI^-$, has the highest conductivity (7.5×10^{-6} S cm^{-1} at 37 °C). Surprisingly, the ionic conductivity of its analogous PIL diblock copolymer SPE in Figure 2.4b exhibits a nearly three orders of magnitude decrease (5.3×10^{-9} S cm^{-1} at 37 °C). Contrastingly, the conductivity data between PIL homopolymer and PIL diblock copolymer SPEs with MIm^+/FSI^- and $MPyr^+/FSI^-$ ion pairs show relatively similar conductivities ($\sigma = 1.88 \times 10^{-6}$ S cm^{-1} for poly(VBMIm-FSI)-0.5 *versus* $\sigma = 2.11 \times 10^{-6}$ S cm^{-1} for MIm-FSI+Li-FSI-0.5 at 29 °C, and $\sigma = 1.10 \times 10^{-7}$ S cm^{-1} for poly(VBMPyr-FSI)-0.5 *versus* $\sigma = 7.82 \times 10^{-8}$ S

cm^{-1} for MPyr-FSI+Li-FSI-0.5 at 29 °C). For PIL homopolymer SPEs, the ion transport mechanism is governed by both segmental dynamics assisted hopping and the ion pair dissociation-association process.[95] The presence of non-conductive block (PS) in the PIL diblock copolymer SPEs could reduce the intramolecular hopping and increase the ion association relaxation time, leading to the lower ion mobility (ionic conductivity).[93] However, surprisingly, we observed relatively similar conductivity in the PIL diblock copolymers with MIm$^+$/FSI$^-$ and MPyr$^+$/FSI$^-$ ion pairs compared to their PIL homopolymer analogs at the same salt concentration. Similar results were observed for other PIL block copolymers that exhibit nanoscale morphology, which contribute to significantly different transport mechanisms and accelerates transport, while the PIL homopolymers exhibit no microphase separation.[113-114] Additionally, the FSI$^-$ has a smaller anion size comparing with TFSI$^-$ (*i.e.*, V_{FSI^-} = 178 Å^3 *versus* V_{TFSI^-} = 248 Å^3),[103, 115] as well as a relatively weaker interaction energy with cations (*i.e.*, stabilization energy in Li-FSI complex = -134.3 kcal/mol *versus* stabilization energy in Li-TFSI complex = -137.2 kcal/mol, calculated by the supermolecular method in ref [111]) which can be beneficial for anion motion and diffusivity in the present study. The ion transport mechanism and the correlation between cation/anion in the PIL diblock copolymer SPEs will be examined in more depth with Figures 2.5 and 2.7.
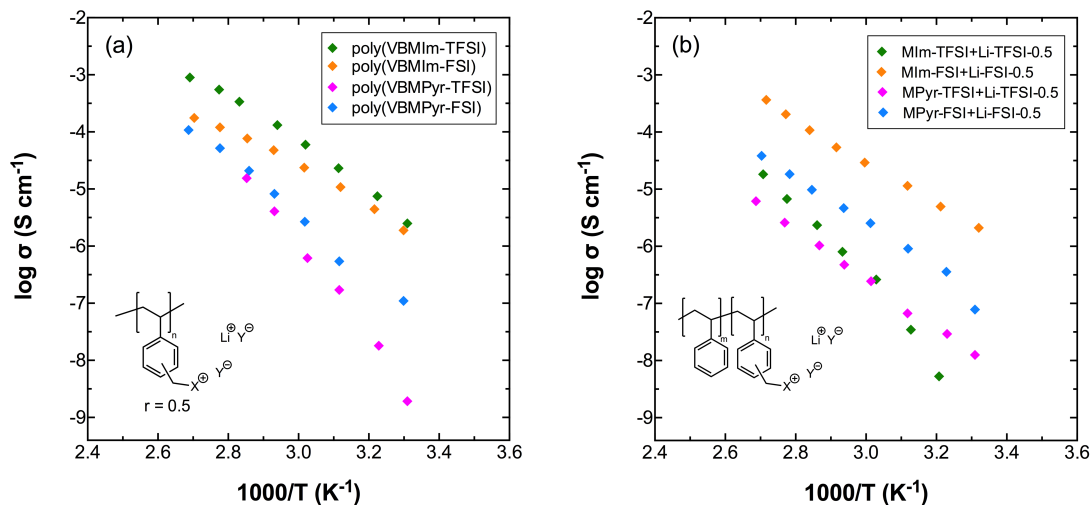
Figure 2.4 Temperature-dependent dry (H$_2$O < 5 ppm) ionic conductivity of the (a) PIL homopolymer SPEs and (b) PIL diblock copolymer SPEs with different cation/anion chemistry at r = [Li]/[PIL] (mol/mol) = 0.5.

Figure 2.5 shows the temperature-dependent ionic conductivity for SPEs with different cation/anion chemistries at r = 0.5. Conductivity profiles of MIm-FSI+Li-FSI-0.5, MPyr-TFSI+Li-TFSI-0.5, and MPyr-FSI+Li-FSI-0.5 were regressed to Arrhenius equation:

$$\sigma(T) = \sigma_0 \exp\left(-\frac{E_a}{RT}\right) \tag{2.7}$$

where E$_a$ is the activation energy related to the potential barrier of the displacement of the charge carrier. The MIm-TFSI+Li-TFSI-0.5 was regressed to the VFT equation[116-117]:

$$\sigma(T) = \sigma_0 \exp\left(-\frac{b}{T-T_0}\right) \tag{2.8}$$

where σ_0 (S cm^{-1}) is the infinite temperature conductivity, which is proportional to the free ion concentration, b (K) is a constant related to the pseudo-activation energy required for segmental motion of the polymer chain, and T$_0$ (K) is the Vogel temperature, which corresponds to a temperature at which ion motion first occurs and is typically ~ 50 K

below the measured T_g of the polymer. The inset indicates the conductivity profile of MIm-FSI+Li-FSI-0.5 regressed to both VFT and Arrhenius equations. The VFT model accounts for the relaxation and segmental motion of polymer chains, while the Arrhenius model accounts for the thermal hopping frequency. Those two types of conductivity behaviors can be found for the same type of polymer electrolyte, depending on the predominant elementary conductivity process. From the inset, the Arrhenius regression represents a reasonable fit with minor deviations for the MIm-FSI+Li-FSI-0.5 within the full temperature range (29 to 95 ºC), while the VFT regression appears to significant deviation under higher temperatures (79 to 95 ºC). Similar comparisons of regression result can also be observed for MPyr-TFSI+Li-TFSI-0.5 and MPyr-FSI+Li-FSI-0.5 SPEs (Figure 2.6).

Comparing Figures 2.4 and 2.5, one observes SPEs have stronger Arrhenius behavior (*i.e.*, MIm-FSI+Li-FSI-0.5 and MPyr-FSI+Li-FSI-0.5) also show minimal difference in ionic conductivity between PIL homopolymer and PIL block copolymer SPEs. These suggest that the ion hopping mechanism in the MIm-FSI+Li-FSI-0.5 and MPyr-FSI+Li-FSI-0.5 SPEs exhibits enhanced ion transport and is independent of the change in the conducting volume fraction (*e.g.*, from 100% for homopolymer to 77.5 % for MIm-FSI+Li-FSI-0.5), as well as shows the potential of being decoupled from polymer segmental relaxation. While in MIm-TFSI+Li-TFSI-0.5, however, the segmental dynamics of polymer chains are dampened by the coordination of non-conducting PS block compared with poly(VBMIm-TFSI) SPEs and will be discussed in more detail in Figure 2.8.

38
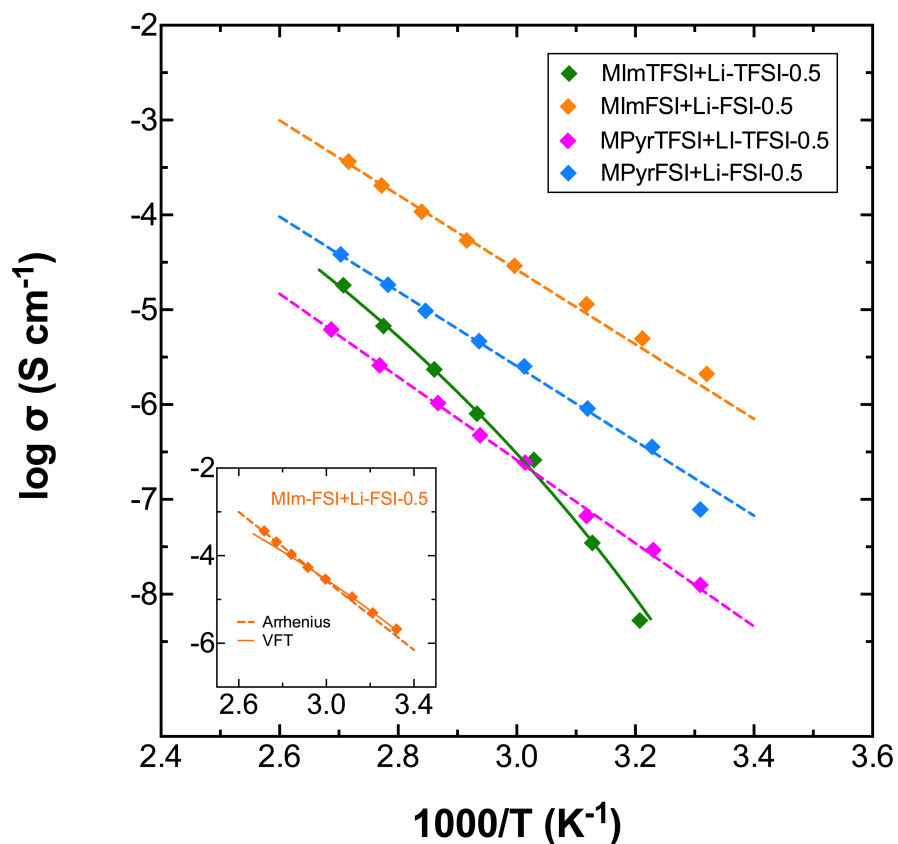
Figure 2.5 Temperature-dependent dry (H_2O < 5 ppm) ionic conductivity of the PIL diblock copolymer SPEs with different cation/anion chemistry at r = 0.5. Data of MIm-FSI+Li-FSI-0.5, MPyr-TFSI+Li-TFSI-0.5, and MPyr-FSI+Li-FSI-0.5 regressed to Arrhenius equation (dash line) and MIm-TFSI+Li-TFSI-0.5 regressed to VFT equation (solid line). The inset indicates the conductivity profile of MIm-FSI+Li-FSI-0.5 regressed to both VFT (solid line) and Arrhenius (dash line) equations.
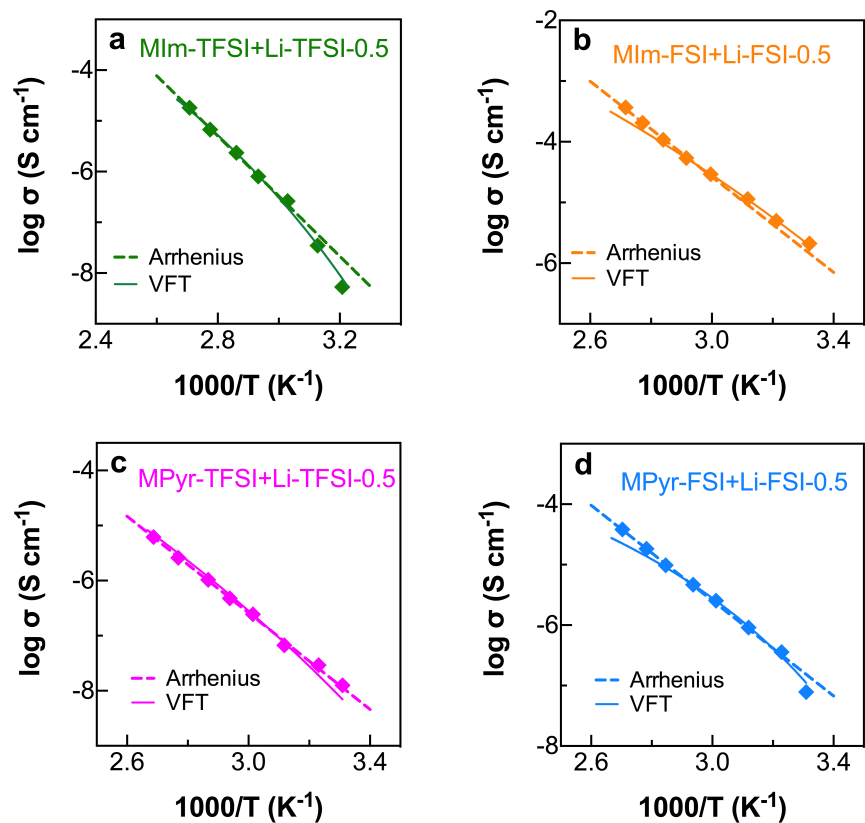
Figure 2.6 Comparison of conductivity profiles regressed to both VFT (solid line) and Arrhenius (dash line) equations for (a) MIm-TFSI+Li-TFSI-0.5, (b) MIm-FSI+Li-FSI-0.5, (c) MPyr-TFSI+Li-TFSI-0.5, and (d) MPyr-FSI+Li-FSI-0.5.

In order to elucidate the impact of cation/anion correlation on ionic conductivity, conductivity *versus* reduced temperature, $T_{g, PIL}/T$ was plotted in Figure 2.7. In salt-doped PIL block copolymer SPEs, the ionic conductivity depends on the ion hopping of the counterions (*i.e.*, anions) and these dynamics are correlated to not only the polymer chain segmental motion, but also the charge delocalization and the cation-anion interactions. Plotting the T_g-independent conductivity is a method to de-emphasize the contribution of segmental motion and emphasize the factors of cation-anion interactions, which the latter

also strongly affect ion transport in this system. The T_g-independent conductivity of MIm-TFSI+Li-TFSI-0.5 displays a steeper slope than that of others, suggesting a different ion transport mechanism. Interestingly, MPyr-FSI+Li-FSI-0.5 exhibits the highest T_g-independent conductivity, especially when it approaches to $T_{g,\text{PIL}}$ (*i.e.,* $\sigma(T_{g,\text{PIL}}) \sim 5.3 \times 10^{-9}$ S cm^{-1}). Comparisons between the ion pairs reveal interesting phenomena that the SPE with MPyr$^+$ exhibits higher T_g-independent conductivity than SPE with MIm$^+$, while the SPE with FSI$^-$ exhibits higher T_g-independent conductivity than SPE with TFSI$^-$. This result recalls the previous discussion in Figure 2.4 that the smaller ion size and weaker interaction energy of FSI$^-$ can be beneficial in the PIL diblock copolymers.

Previous work by Watanabe *et al.*[118] used ionic conductivities measured *via* AC impedance and pulsed-gradient spin-echo (PGSE) NMR method to quantify the ionicity (ion-ion interactions) in ionic liquids, revealing the stronger ion-ion interaction of imidazolium based IL compared with that of pyrrolidinium IL. Another study by Winey *et al.*[56] also illustrated the strong correlation of ionic conductivity and the hopping energy barrier (anion-anion hopping distance). Therefore, for the present system with similar morphologies, the lower ion interactions for both MPyr$^+$ and FSI$^-$ ions might be the factor that influences the T_g-independent conductivity. Results in Figure 2.7 emphasize the significant contribution of cation-anion interactions in ionic conductivity for the salt-doped PIL block copolymer SPEs.
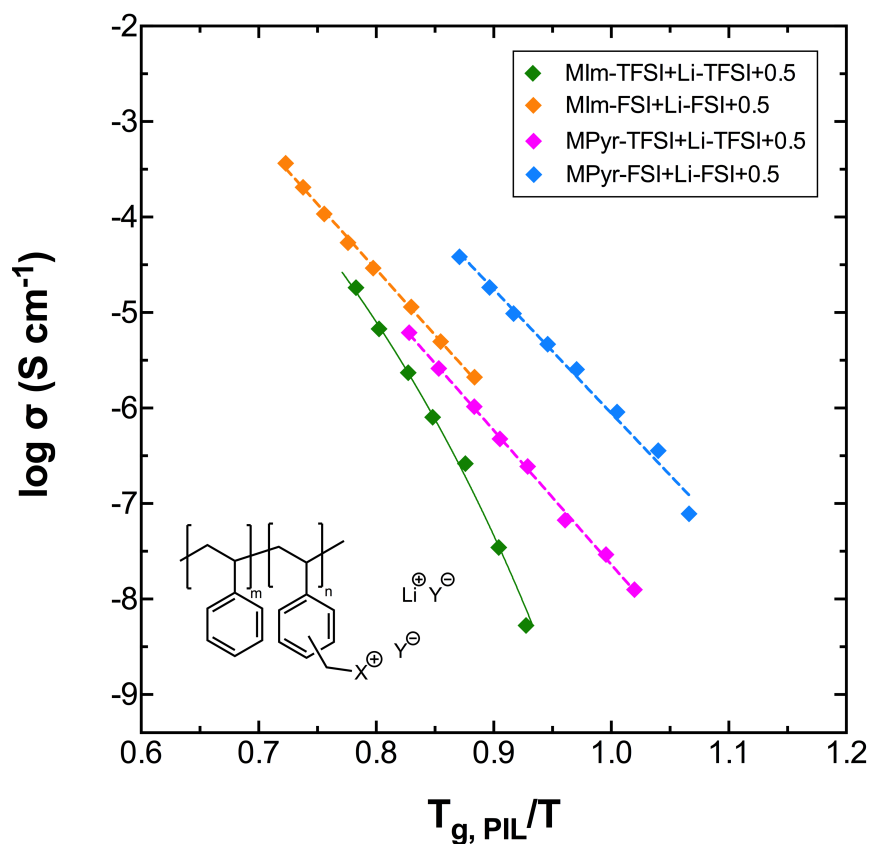
Figure 2.7 Ionic conductivity *versus* $T_{g, PIL}/T$ of the PIL diblock copolymer SPEs with different cation/anion chemistries at r = 0.5. Data of MIm-FSI+Li-FSI-0.5, MPyr-TFSI+Li-TFSI-0.5, and MPyr-FSI+Li-FSI-0.5 regressed to Arrhenius equation (dash line) and MIm-TFSI+Li-TFSI-0.5 regressed to VFT equation (solid line).

Figure 2.8 shows the temperature-dependent ionic conductivity of the PIL homopolymer SPEs, poly(VBMIm-TFSI)+Li-TFSI-r (Figure 2.8a) and their analogous PIL diblock copolymer SPEs, MIm-TFSI+Li-TFSI-r (Figure 2.8b) with r = [Li]/[PVBMIm-TFSI] (mol/mol) = 0.1−0.8. The comparisons between the ionic conductivity of PIL homopolymer and PIL diblock copolymer SPEs reveal an interesting departure from each other. In Figure 2.8a, the PIL homopolymer SPE conductivity shows a non-monotonic

trend as a function of r with the maximum conductivity at r = 0.5 (2.5×10^{-6} cm^{-1} at 29 ℃). The r = 0.5 SPE is three orders of magnitude higher than r = 0.8 at 29 ℃ (*i.e.*, 2.5×10^{-6} S cm^{-1} *versus* 2.9×10^{-9} S cm^{-1}). In Figure 2.8b, however, the conductivity of PIL diblock copolymer SPEs shows a trend that almost collapses onto one single curve. The decrease of conductivity in MIm-TFSI+Li-TFSI-r compared with its analogous homopolymer SPEs ($\sigma = 7.47 \times 10^{-6}$ S cm^{-1} for poly(VBMIm-TFSI)-0.5 *versus* $\sigma = 5.30 \times 10^{-9}$ S cm^{-1} for MIm-TFSI+Li-TFSI-0.5 at 37 ℃) exhibits a significant difference compared to the other PIL diblock copolymer SPEs (Figure 2.4). Note that all PIL diblock copolymer SPEs in the present study exhibit microphase separation morphologies; the factors that result in this different trend in MIm-TFSI+Li-TFSI-r may be attributed to (1) the higher ion interaction between MIm$^+$/TFSI$^-$, (2) the larger ion size of TFSI$^-$ that could be hindered by the non-conducting domain and affects the diffusion of ions, and (3) the segmental motion dominated ion transport mechanism of MIm-TFSI+Li-TFSI-r SPE, which will be examined in more detail in Figure 2.9.
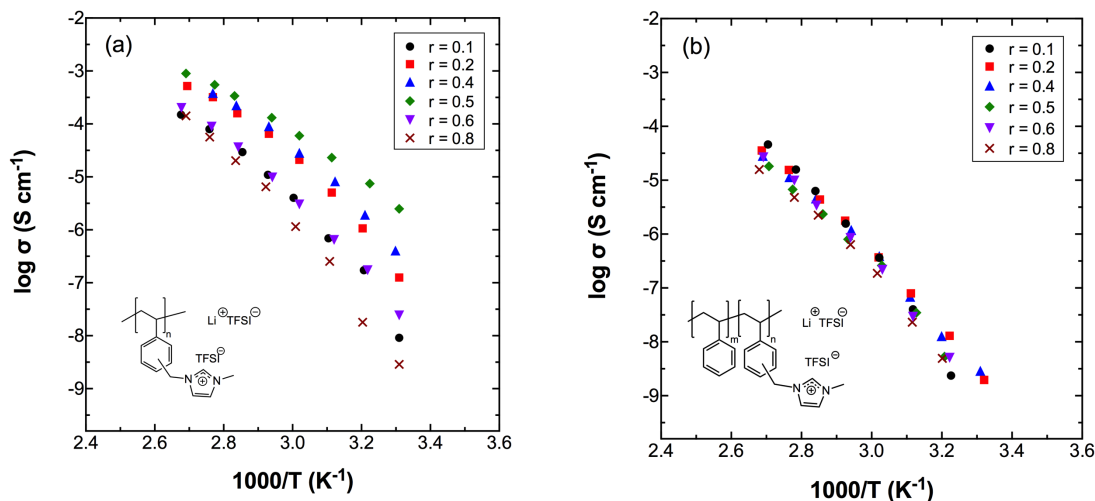
Figure 2.8 Temperature-dependent dry (H_2O < 5 ppm) ionic conductivity of the (a) poly(VBMIm-TFSI) SPEs and (b) MIm-TFSI+Li-TFSI-r SPEs at different r = [Li]/[PVBMIm-TFSI] (mol/mol).

Figure 2.9 shows the temperature-dependent ionic conductivity for MIm-TFSI+Li-TFSI-r SPEs and their regressions to VFT equation. The inset indicates the conductivity profile of MIm-TFSI+Li-TFSI-0.5 regressed to both VFT and Arrhenius equations. The resulting VFT fitting parameters are listed in Table 2.3. From the inset, the VFT regression represents a reasonable fit with minor deviation (R^2 = 0.9983) for the MIm-TFSI+Li-TFSI-0.5 over the full temperature range (29 to 97 ºC), while the Arrhenius regression appears to moderately deviate at lower temperatures (29 to 48 ºC). These deviations in regressions between the Arrhenius and VFT equations can be observed for all MIm-TFSI+Li-TFSI-r SPEs. This result indicates that in MIm-TFSI+Li-TFSI-r SPEs, ion motion is strongly dictated by polymer segmental dynamics (VFT equation) over the full temperature range and less dependent on ion hopping mechanism (Arrhenius equation).

The transition in the dominant transport mechanism from ion hopping to segmental motion between the homopolymer (poly(VBMIm-TFSI)-r) and block copolymer (MIm-TFSI+Li-TFSI-r) SPEs suggests the significant influence of transport mechanism in ion conduction performance.

Overall, the ionic conductivity results indicate that (1) the ion hopping mechanism has the potential of being decoupled from polymer segmental relaxation in the present PIL diblock copolymer SPE, (2) FSI$^-$ containing SPEs can have higher conductivity due to the smaller ion size and lower association energy with cations, and (3) the conductivity can be simply controlled *via* manipulating the ion pair chemistry of PILs.
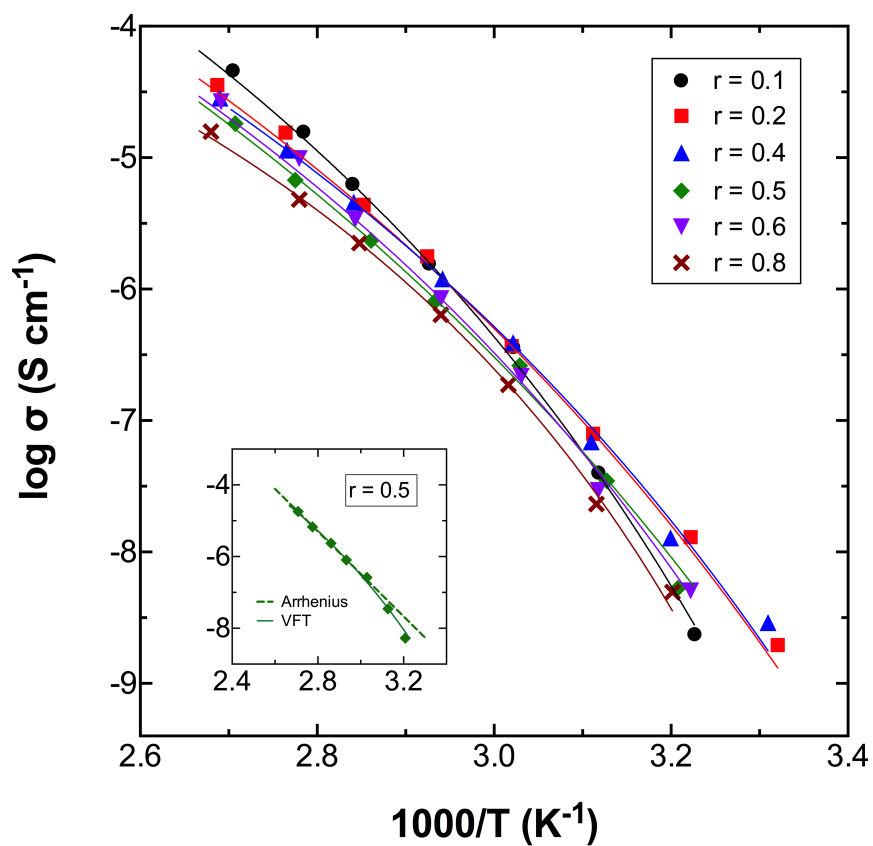
Figure 2.9 Temperature-dependent dry (H_2O < 5 ppm) ionic conductivity of the MIm-TFSI+Li-TFSI-r SPEs. Data regressed to VFT equation (solid lines). The inset indicates the conductivity profile of MIm-TFSI+Li-TFSI-0.5 regressed to both VFT (solid line) and Arrhenius (dash line) equations.

Table 2.3 VFT regression results for MIm-TFSI+Li-TFSI-r SPEs.

r	σ_0 (mS cm^{-1})	b (K)	T_0 (K)	[a] $T_{g, PIL}$ (K)	$T_{g, PIL}-T_0$ (K)
0.1	4.9	1423	246.8	295.15	48.35
0.2	3.0	1650	226.6	291.15	64.55
0.4	5.0	1793	223.3	289.15	66.85
0.5	30.0	2397	203.1	289.15	86.05
0.6	1.2	1404	240.0	287.15	47.15
0.8	1.0	1569	231.3	285.15	53.86

[a] PIL block T_g measured from DSC.

Figure 2.10 shows the parameters for calculating the transference numbers of MIm-TFSI+Li-TFSI-r SPEs *via* galvanostatic polarization. Figure 2.10a-c shows the ionic conductivity at 40 °C, salt diffusion coefficient (D), and steady-state transference number (t_{s-s}) for MIm-TFSI+Li-TFSI-r SPEs as a function of salt concentration r, respectively. In Figure 2.10a, the ionic conductivity measured *via* EIS exhibits a non-monotonic relationship as a function of r with the maximum conductivity (1.3×10^{-8} S cm^{-1}) at r *ca.* 0.2-0.4. This result is consistent with neutral block copolymer-salt mixtures (*e.g.*, SEO/lithium salt) in the literature.[35] Figure 2.10b shows the salt diffusion coefficient (D), measured by restricted-diffusion measurement as a function of r. The salt diffusion coefficient is a mutual diffusion coefficient relevant to ion transport in electrolyte.[92] The SPE also exhibits a maximum value of 7.04×10^{-9} cm^2 s^{-1} at r = 0.2, and the trend corresponds with conductivity in Figure 2.10a. In Figure 2.10c, steady-state transference

number, t_{s-s}, based on Bruce-Vincent method of ideal dilute electrolytes, are calculated by Equation 2.5 and is shown as a function of salt concentration, r. The t_{s-s} reaches a maximum *ca.* 0.88 at r = 0.4, and begins to decrease with the increase of r. Similar behavior in conductivity at 40 °C, salt diffusion coefficient, and steady-state transference number in Figure 2.10a-c indicates the strong correlation between conductivity and ion transport.

Figure 2.10d represents concentration potential, U, as a function of the logarithm of the salt molality, ln m. m is defined as the moles of salt per kg of PIL domain and calculated from the salt concentration (r) by Equation 2.9:

$$m = \frac{r}{MW_{IL}} \tag{2.9}$$

where $MW_{IL} = MW_{VBMIm-TFSI} = 0.47942$ kg mol^{-1}. The concentration potential, U, was measured in concentration cells using a reference electrode with salt molality equal to 0.417 mol kg^{-1} (*i.e.*, r = 0.2) under room temperature. The regression curve in Figure 2.10d was determined by third-order polynomial fit to obtain the function of:

$$U = -40.64 - 36.72(lnm) - 10.07(lnm)^2 - 4.278(lnm)^3 \tag{2.10}$$

Equation 2.10 is used to determined dU/dln m, in order to calculate the transference number, t^0_+ at Equation 2.11. The dU/dln m is calculated by taking the derivative of Equation 2.10.
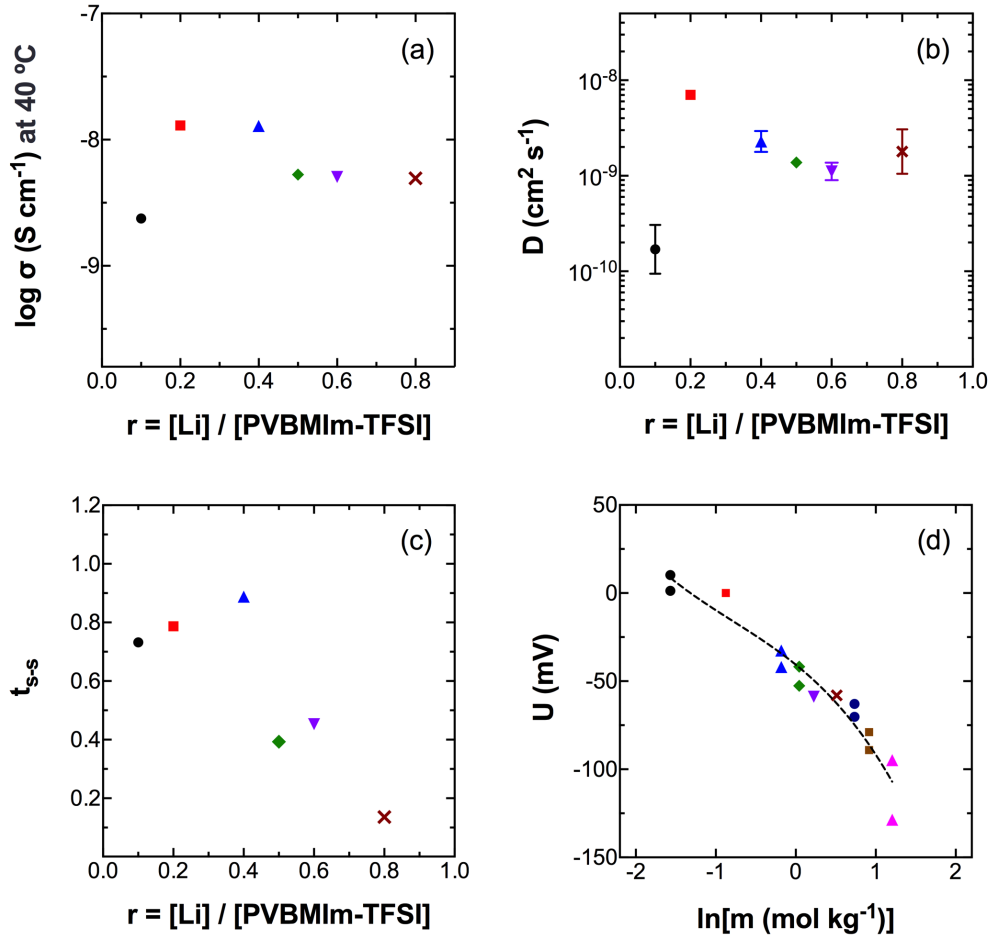
Figure 2.10 (a) Ionic conductivity σ at 40 °C; (b) restricted diffusion coefficient, D, (c) the steady-state current transference number, t_{s-s} as a function of salt concentration, r, and (d) concentration potential as a function of molarity, m, for MIm-TFSI+Li-TFSI-r SPEs.

Figure 2.11 shows the transference number, t^0_+ as a function of salt concentration (r), for MIm-TFSI+Li-TFSI-r SPEs. t^0_+ was calculated by Equation 2.11:

$$t^0_+ = 1 + (\frac{1}{t_{s-s}} - 1)\frac{(z_+\nu_+)FDc\phi_c}{\sigma}(\frac{dU}{dlnm})^{-1} \tag{2.11}$$

where z_+ is the charge on the cation, ν_+ is the number of cations in the dissociated salt, F is Faraday's constant (96485 C), ϕ_c is the volume fraction of the conducting phase

calculated by Equation 2.3 (Table 2.1), and c is the molar salt concentration in the conducting domain (mol cm^{-3}) calculated by Equation 2.12:

$$c = \frac{\rho_{IL} r}{MW_{IL} + r MW_{TFSI}} \tag{2.12}$$

where MW$_{TFSI}$ is the molar mass of Li-TFSI (287.08 g mol^{-1}). The parameters in Equation 2.11 using t_{s-s} from Figure 2.10c, D from Figure 2.10b, σ from Figure 2.10a, and $\frac{dU}{dlnm}$ by taking the derivative of Equation 2.9 for each salt concentration. At lower salt concentration ($r < 0.4$), t^0_+ is very close to the unity (*ca.* 0.95-0.98) while t^0_+ starts to decrease with the increase of r (*i.e.,* r = 0.5−0.8), and reaches a negative transference number at r = 0.8. From studies conducted by Balsara *et al.*,[37, 92, 99] the negative transference number implies the presence of negative-charged ion clusters (*i.e.,* Li$^+$ coordinates with TFSI$^-$), which is more mobile than free cations. Studies from both experimental and molecular simulation methods proved that Li$^+$ can coordinate with up to four oxygen atoms on TFSI$^-$ and form larger anion-rich ion clusters, [Li(TFSI)$_{m+1}$]$^{m-}$, with $m+1 \leq 4$.[119-123] Thus, when an electric field is applied to the electrolyte both Li$^+$ and TFSI$^-$ are driven to same direction as clusters. Those negatively-charged ion clusters (anions) would become the dominant mobile species and lead to the negative transference number and decrease of mobility of all ions, especially the Li$^+$.
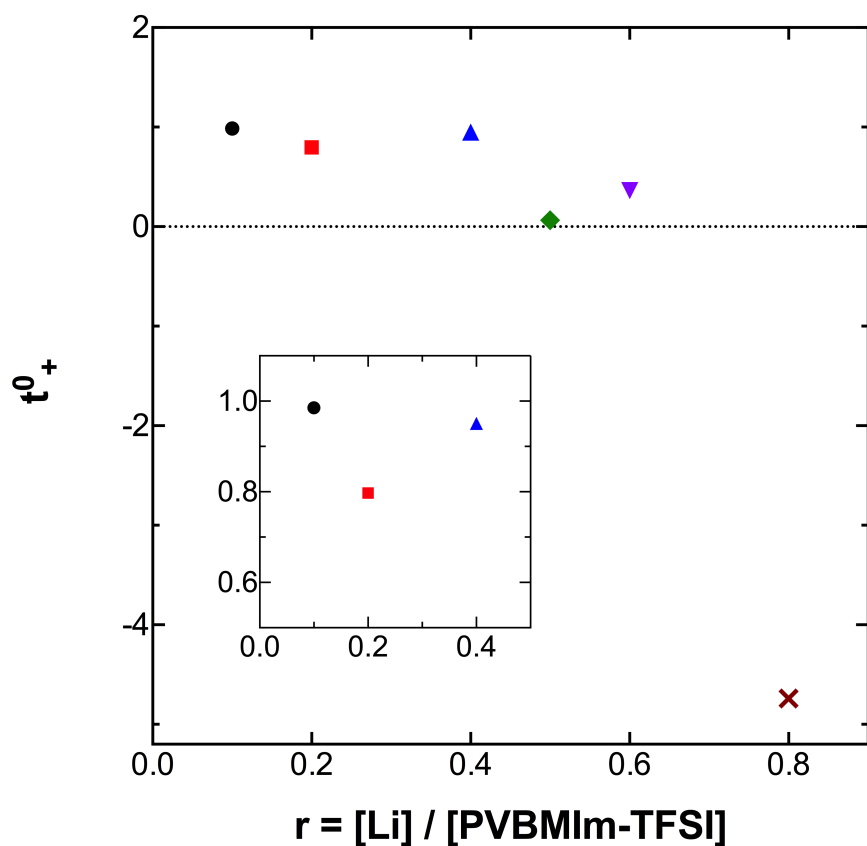
Figure 2.11 Transference number, t^0_+ as a function of salt concentration, r, for MIm-TFSI+Li-TFSI-r SPEs at room temperature.

Figure 2.12 shows selected Li-metal stripping and plating overvoltage profiles for SPEs with different salt concentration, MIm-TFSI+Li-TFSI-0.4 and MIm-TFSI+Li-TFSI-0.5 (Figure 2.12a); measurements are at a current density of 0.02 mA cm^{-2} at 70 °C. Both SPEs reveal a higher first cycle and then maintain a relatively constant overvoltage window (*ca.* 120 mV for MIm-TFSI+Li-TFSI-0.4 and *ca.* 110 mV for MIm-TFSI+Li-TFSI-0.5, respectively), as well as a smooth polarization profile over 200 cycles. These results indicate a smooth interface formation on the lithium metal and an ability to suppress

polarization degradation. The smooth overvoltage profiles also indicate that no lithium dendrites formation occurred and a good compatibility between SPE and lithium metal electrode.[124]

The impedance response from the stripping and plating cycles was regressed to an equivalent circuit model to determine all resistances across the entire cell.[104] The electrolyte bulk resistance (R_b) and interfacial resistance (R_i) were evaluated as a function of selected cycles in Figures 2.12b and 2.12c. The overall interfacial resistance (R_i) is composed of the passive layer resistance (R_p) from the solid electrolyte interface (SEI) and the charge transfer resistance (R_{ct}) between electrode and electrolyte; *i.e.*, $R_i = R_{ct} + R_p$. The R_b of both SPEs remain stable (*ca.* 70 Ω for MIm-TFSI+Li-TFSI-0.4 and *ca.* 85 Ω for MIm-TFSI+Li-TFSI-0.5, respectively) during the 200 cycles. The relatively higher R_b of MIm-TFSI+Li-TFSI-0.5 may due to its slightly lower ionic conductivity comparing with that of MIm-TFSI+Li-TFSI-0.4 (*i.e.*, 8×10^{-7} S cm^{-1} for MIm-TFSI+Li-TFSI-0.4 *versus.* 1.2×10^{-6} S cm^{-1} for MIm-TFSI+Li-TFSI-0.5, respectively at 70 °C). Interestingly, in Figure 2.12c, both SPEs show an identical trend of R_i that overlapped with each other. The trend of R_i begins at *ca.* 3500 Ω and then gradually decreases during cycling and reaches *ca.* 2350 Ω for both SPEs after 200 cycles. The decrease of R_i and unchanging overvoltage profiles indicate a stable and conductive SEI was formed. The low and stable polarization can be explained by an increase in the surface area of active lithium at the electrode during lithium stripping and plating, which has also been observed in IL based electrolytes.[125-127] In Figure 2.12, the cell overvoltage profiles can be correlated with R_b of the SPEs; typically, stable R_b correlates to stable polarization profiles and *vice versa*.

The salt concentration here only has minimal impact on lithium-metal stripping and plating results. Overall, both SPEs show stable R_i after 200 cycles, indicating good interfacial contact between the lithium electrode and the SPE, as well as enhanced SEI layer stability.
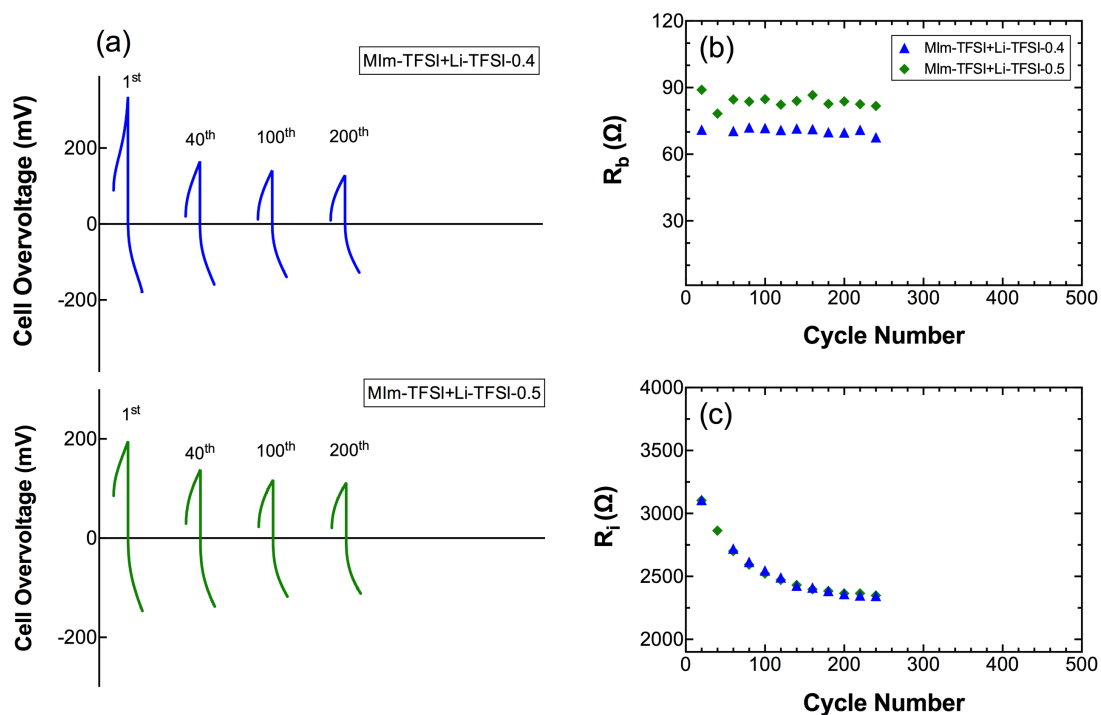
Figure 2.12 Selected Li-metal stripping-plating cycles with symmetric Li / SPE / Li cell under 0.02 mA cm^{-2} at 70 ºC of (a) MIm-TFSI+Li-TFSI-0.4 and MIm-TFSI+Li-TFSI-0.5. (b) Electrolyte bulk resistance (R_b) and (c) interfacial resistance (R_i) at selected cycles from equivalent circuit model regression of impedance spectra.

Figure 2.13 shows selected Li-metal stripping and plating overvoltage profiles for SPEs with different cation/anion chemistries at r = 0.5, MIm-TFSI+Li-TFSI-0.5, MIm-FSI+Li-FSI-0.5, and MPyr-FSI+Li-FSI-0.5 (Figure 2.13a); measurements are at a current density

of 0.02 mA cm^{-2} at 70 °C. All three SPEs reveal a smooth polarization profile; MIm-TFSI+Li-TFSI-0.5 and MPyr-FSI+Li-FSI-0.5 exhibit higher first cycle and then remain a constant overvoltage window (*ca.* 110 mV for MIm-TFSI+Li-TFSI-0.5 and *ca.* 50 mV for MPyr-FSI+Li-FSI-0.5, respectively), while MIm-FSI+Li-FSI-0.5 remain a relatively constant and smaller overvoltage window *ca.* 7-8 mV from the beginning over 200 cycles. Similar to the results in Figure 2.12, all SPEs show great capability to suppress polarization degradation, good compatibility with lithium metal, and no occurrence of lithium dendrites formation.

The impedance response from the stripping and plating cycles was regressed to an equivalent circuit model to determine all resistances across the entire cell. The R_b of all three SPEs remain stable (*ca.* 83 Ω for MIm-TFSI+Li-TFSI-0.5, *ca.* 94 Ω for MIm-TFSI+Li-TFSI-0.5, and *ca.* 377 Ω for MPyr-FSI+Li-FSI-0.5, respectively) during the 200 cycles. In Figure 2.13c, MIm-FSI+Li-FSI-0.5 and MPyr-FSI+Li-FSI-0.5 reveal nearly two and one orders of magnitude lower R_i than that of MIm-TFSI+Li-TFSI-0.5 (*i.e.*, *ca.* 46 Ω and 500 Ω *versus* 2600 Ω, respectively). Additionally, MIm-FSI+Li-FSI-0.5 and MPyr-FSI+Li-FSI-0.5 exhibit an increasing trend of R_i (from 18 Ω to 75 Ω for MIm-TFSI+Li-TFSI-0.5 and from 443 Ω to 608 Ω for MPyr-FSI+Li-FSI-0.5, respectively) which is different from that of MIm-TFSI+Li-TFSI-0.5 that R_i gradually decreases from 3500 Ω to 2350 Ω while cycling. The significant influence of cation/anion chemistry could be observed where SPEs with FSI$^-$ have lower cell overvoltage range, R_b, and R_i than that of SPE with TFSI$^-$. From Figure 2.13, one can conclude that the polarization and resistances of SPE can be easily controlled by manipulating the cation/anion chemistries. The

significant difference between FSI⁻ and TFSI⁻ containing SPEs could attribute to the weaker interaction of FSI⁻ with cations (Li^+, MIm^+, and $MPyr^+$), which can also be observed in other IL/salt systems.[128-129] The weaker interactions enable faster exchange of FSI⁻ binding with cations and therefore increase the mobility of ions.[128] The faster diffusion of Li^+ in the FSI⁻anion containing SPE can also be beneficial for preventing the formation of concentration gradient during the battery charge-discharge. The stable binary SPE, especially the MIm-FSI+Li-FSI-0.5 SPE may be a promising candidate for the lithium ion battery.
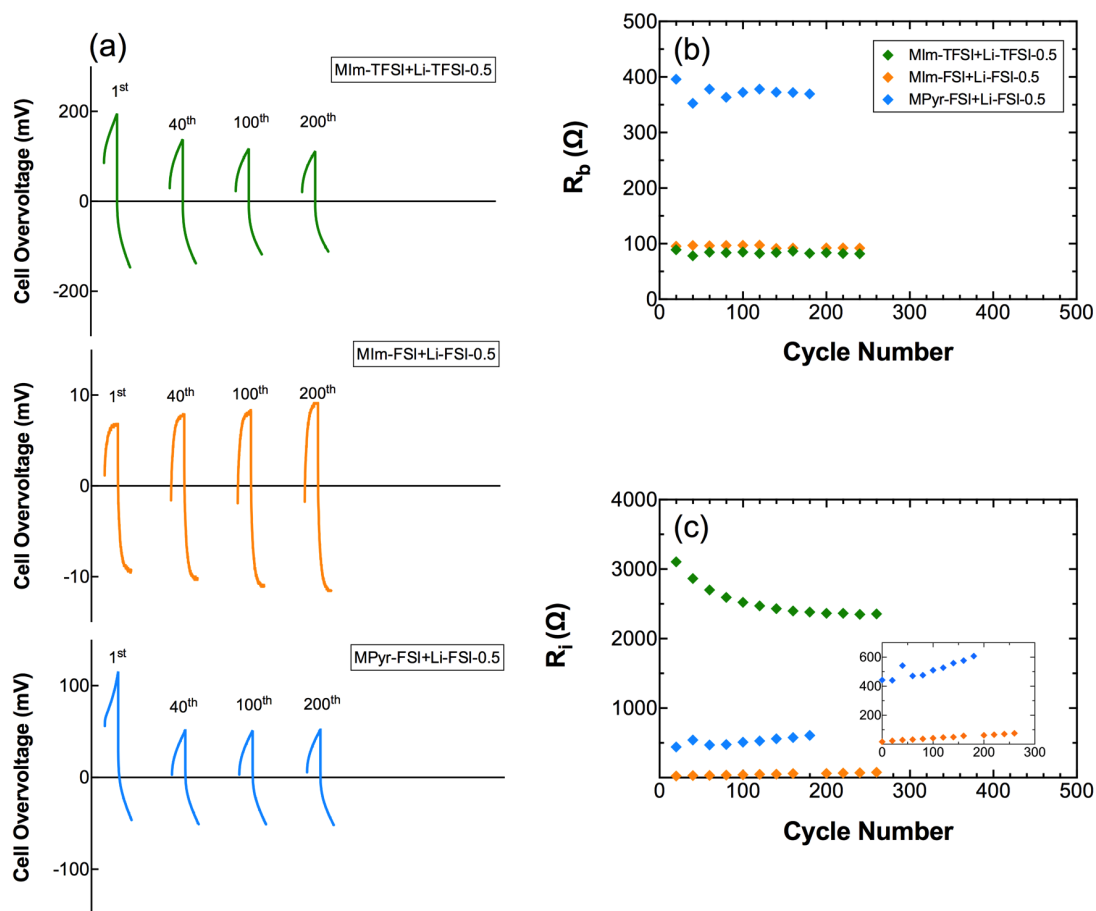
Figure 2.13 Selected Li-metal stripping-plating cycles with symmetric Li / SPE / Li cell under 0.02 mA cm^{-2} at 70 ºC of (a) MIm-TFSI+Li-TFSI-0.5, MIm-FSI+Li-FSI-0.5and MPyr-FSI+Li-FSI-0.5. (b) Electrolyte bulk resistance (R_b) and (c) interfacial resistance (R_i) at selected cycles from equivalent circuit model regression of impedance spectra.

2.4 Conclusions

This study investigates the relationship between salt concentration, cation/anion chemistries and ion transport properties in salt-doped PIL diblock copolymer SPEs. The variety of PIL diblock copolymers with one PS block and another PIL block with MIm$^+$/TFSI$^-$, MIm$^+$/FSI$^-$, MPyr$^+$/TFSI$^-$, and MPyr$^+$/FSI$^-$ ion pairs were systematically

56

investigated with respect to ion transport, morphology, and electrochemical stability. Results showed that SPE with MIm^+/FSI^- ion pair (MIm-FSI+Li-FSI-0.5) exhibits lower T_g and ~1 – 3 orders of magnitude higher conductivity than others. Note that a similar periodic microphase separated cylindrical morphology was observed for all SPEs with varying PIL chemistries, therefore, the conductivity is strongly influenced by ion pair interactions at similar morphologies. The ion-hopping mechanism in the MIm-FSI+Li-FSI-0.5 SPE shows a conductivity similar to its PIL homopolymer analog, while the segmental motion mechanism in the MIm-TFSI+Li-TFSI-0.5 SPE reveals a 3 orders of magnitude lower conductivity compared to its PIL homopolymer analog. The study of transport properties in MIm-TFSI+Li-TFSI-r SPE showed strong correlations between conductivity, salt diffusion coefficient and transference number over a wide range of salt concentrations. The negative transference number at r = 0.8 indicates the formation of larger anion-rich clusters and results in a decrease in ion transport.

This study with varying cation/anion chemistries, salt concentration and transport property relationships, provides avenues to design and control the transport mechanisms through the selection of ion pair chemistries in solid-state PIL block polymers SPEs where one can produce significant electrochemical property changes with subtle and simple chemical modification. This work also highlights that FSI^- anion in the present SPEs can accelerate ion transport and improve both conductivity and cycling stability.

CHAPTER III

LITHIUM ION CONDUCTING POLY(IONIC LIQUID) PENTABLOCK

TERPOLYMERS AS SOLID-STATE ELECTROLYTES[*]

3.1 Introduction

In Chapter II, PIL diblock copolymers show the conjoined properties of both PILs and block copolymers, where the latter not only improves the mechanical robustness of the SPE, but also self-assembles into a periodic microphase-separated nanostructure. Although diblock copolymers have been explored as SPEs and can potentially provide the orthogonal properties of high ion conduction and high mechanical strength simultaneously in a solid-state material,[130] there are limitations to diblock copolymer systems, such as a limited set of morphologies, and a lack of means to achieve simultaneous combination of multiple properties (*e.g.*, conductivity, strength, flexibility). Compared to AB diblock copolymers, multiblock polymers contain more than two chemistries and therefore enable the possibility to contain more than two desired functionalities, such as high ion conductivity, mechanical strength, flexibility, good film forming properties, processability, and high electrochemical stability all into a single material.[131]

In this work, a PIL multiblock polymer (specifically a PIL pentablock terpolymer (PILPTP)) was investigated as lithium ion conducting ternary SPEs for application to

lithium ion batteries. First, an ABCBA pentablock terpolymer, poly(tbS-*b*-EP-*b*-MS-*b*-EP-*b*-tbS), was brominated and quaternized to covalently attach two different cations to the C block (MIm$^+$ and MPyr$^+$) and subsequently ion exchanged to form two different TFSI-exchanged PILPTPs (MPyr-TFSI and MIm-TFSI). Then, lithium ion conducting SPEs were then fabricated by immersing transparent PILPTP thin films into a 1 M Li-TFSI/IL mixture to form ternary blend SPEs. The effect of two different cations (imidazolium and pyrrolidinium) on the conductive C block was also investigated to understand the influence of cation structure (specifically saturated *versus* unsaturated heterocyclic structure) on the electrochemical stability, ion conductivity, thermal stability, and mechanical properties of the SPE. The imidazolium cation has been extensively studied in ILs and PILs due to its higher ionic conductivity compared to other cations.[132-134] Recently, the saturated heterocyclic cations, such as pyrrolidinium, have gained more interest in ILs and PILs owing to its outstanding thermal and electrochemical stability. Although, in ILs, comparisons between unsaturated (*e.g.*, imidazolium) and saturated (*e.g.*, pyrrolidinium) cations have been explored,[62, 64, 135] there are few studies[136-137] that have explored the effects of cation structure (*e.g.*, saturated and unsaturated heterocyclic cations) on ternary SPEs based on PIL multiblock polymers.

3.2 Experimental Methods

3.2.1 Materials

Bis(trifluoromethane)sulfonimide lithium salt (Li-TFSI, 99.95%), and lithium ribbon (0.38 mm × 23 mm, 99.9%) were used as received from Sigma-Aldrich. 1-ethyl-3-

methylimidazolium bis(trifluoromethylsulfonyl)imide (EMIm-TFSI, 99%, IoLiTec) and

1-butyl-1-methylpyrrolidinium bis(trifluoromethylsulfonyl)imide (PYR$_{14}$-TFSI, 99%, IoLiTec) were dried under dynamic vacuum for 24 h and stored in argon-filled glove box

(mBraun) before use. Conductive carbon-coated aluminum foil (0.05 mg cm^{-2}), CR2032

coin cell cases (20 mm diameter $\times$ 3.2 mm thickness) with O-rings for battery research,

stainless steel spacers for CR2032 cells (15.5 mm diameter $\times$ 0.5 mm thickness, 15.5 mm

diameter $\times$ 0.2 mm thickness), and stainless steel wave springs for CR2032 cases were

used as received from MTI Corporation. Mylar PET release liner substrates (Grade 26965,

0.0762 mm) were used as received from LOPAREX. Deionized water with resistivity >

16 MΩ cm was used as appropriate.

3.2.2 Synthesis and Fabrication of Lithium Ion Conducting PILPTP Films

Initially, a precursor polymer was used to synthesize and fabricate lithium ion conducting

PILPTP SPE films. The precursor polymer is a ABCBA pentablock terpolymer, poly(tbS-

b-EP-*b*-MS-*b*-EP-*b*-tbS), that was synthesized and provided by Kraton Polymers, and

contains outer A blocks of tert-butyl-styrene (tbS), B blocks of a random copolymer of

ethylene-*r*-propylene (EP), and an inner C block of 4-methylstyrene (MS) (chemical

structure shown in Figure 3.1). This precursor ABCBA pentablock terpolymer has an M$_n$

~76 kg mol^{-1} with M$_n$ of respective blocks equal to 15-13-16-14-18 kg mol^{-1}. The

precursor polymer was subsequently brominated and quaternized to covalently attach two

different cations to the C block, methylimidazolium and methylpyrrolidinium, to form two

different bromide-conducting PILPTPs (MPyr-Br and MIm-Br (Table 3.1); Figure 3.1,

steps 1 and 2). Details of these two synthetic steps have been reported in detail elsewhere.[138]

Bromide-conducting PILPTP films were then fabricated by casting the polymer solution (from Figure 3.1, step 2) onto a silicon-coated Mylar PET film using an automatic film applicator (Elcometer 4340) with doctor blade at gauge height and speed of *ca*. 350-400 µm and 80 mm s^{-1}, respectively, under ambient conditions (see Figure 3.2a). Polymer solutions were partially covered with aluminum foil and allowed to evaporate under ambient conditions for 12 h and then further dried under vacuum for 24 h. The final film thicknesses were *ca*. 25-35µm and measured with a digital micrometer (Mitutoyo; accuracy = 0.001 mm).

A solid-state ion exchange metathesis of the bromide-conducting PILPTP films was performed to produce bis(trifluoromethylsulfonyl)imide (TFSI)-exchanged PILPTP films (Figure 3.1, step 3). The films were placed in a Li-TFSI aqueous solution (bromide-conducting PILPTP:Li-TFSI = 1:9 mol/mol, dissolved in 250 ml DI water) under continual mixing. The Li-TFSI solution was replaced with a freshly prepared solution every 24 h and this was repeated 4 times (total time = 96 h). The TFSI-exchanged films were then rinsed in fresh DI water for 30 min and this was repeated 3 times to remove excess TFSI anions. Residual water was removed by drying the films under vacuum at room temperature for 24 h. The dried TFSI-exchanged PILPTP films (referred to as MIm-TFSI and MPyr-TFSI; Table 3.1) were then immersed in a 1.0 M Li-TFSI/ionic liquid (IL) solution (IL = EMIm-TFSI or PYR$_{14}$-TFSI) for 36 h at room temperature. The resulting lithium ion conducting PILPTP SPE films (referred to as MIm-TFSI+Li-TFSI/EMIm-
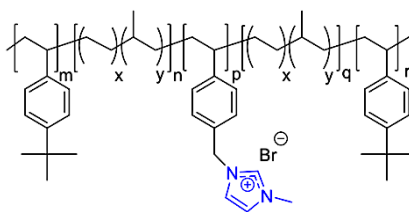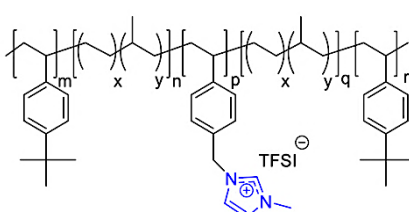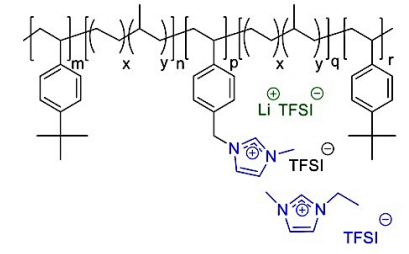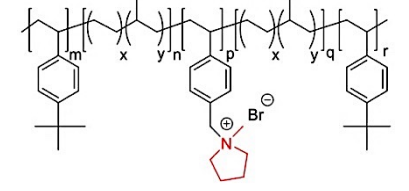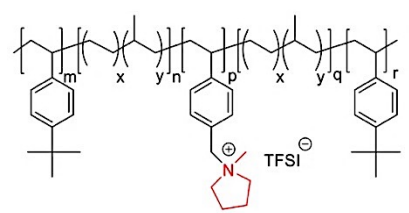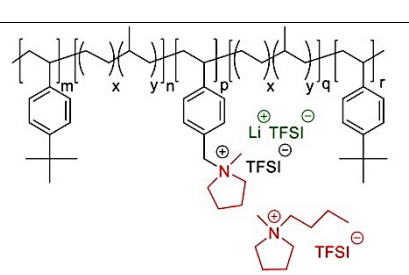
TFSI and MPyr-TFSI+LiTFSI/PYR$_{14}$-TFSI; Table 3.1) were removed from the Li-TFSI/IL solution and the excess Li-TFSI/IL was removed from the surface of the films with lint-free paper (Figure 3.2b). All the resulting SPE films contain *ca.* 8 mg 1.0 M Li-TFSI/ionic liquid solution measured by an analytical balance (Model: MS104TS/00, Mettler Toledo). Films were then dried under vacuum at room temperature for 24 h. The final films were stored inside an argon-filled glovebox (mBraun) with both water and oxygen concentrations < 5 ppm and environmental pressure between 1-8 mbar.
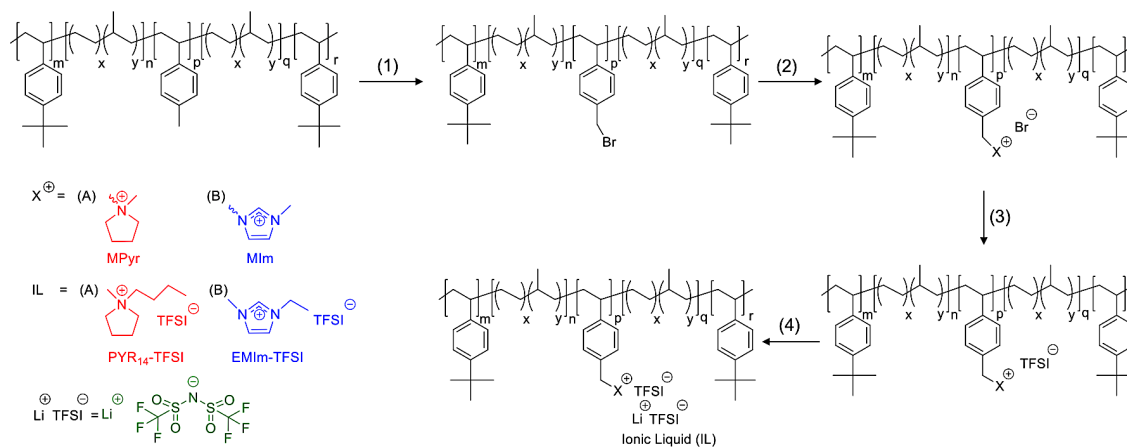
(1) AIBN, NBS, chlorobenzene, 70 °C, 10 h; (2) 1-methylpyrrolidine/1-methylimidazole, toluene, methanol, room temperature, 48 h; (3) Li-TFSI, H$_2$O, room temperature, 96 h; (4) Li-TFSI, ionic liquid, room temperature, 36 h

Figure 3.1 Synthesis of MIm-TFSI+Li-TFSI/EMIm-TFSI and MPyr-TFSI+Li-TFSI/PYR$_{14}$-TFSI. Reprinted with permission from ref[104].

Table 3.1 Sample name and chemical structure of PILPTPs. Reprinted with permission from ref[104].

Chemical structure	Sample name
	MIm-Br
	MIm-TFSI
	MIm-TFSI+ Li-TFSI/EMIm-TFSI
	MPyr-Br
	MPyr-TFSI
	MPyr-TFSI+ Li-TFSI/PYR$_{14}$-TFSI
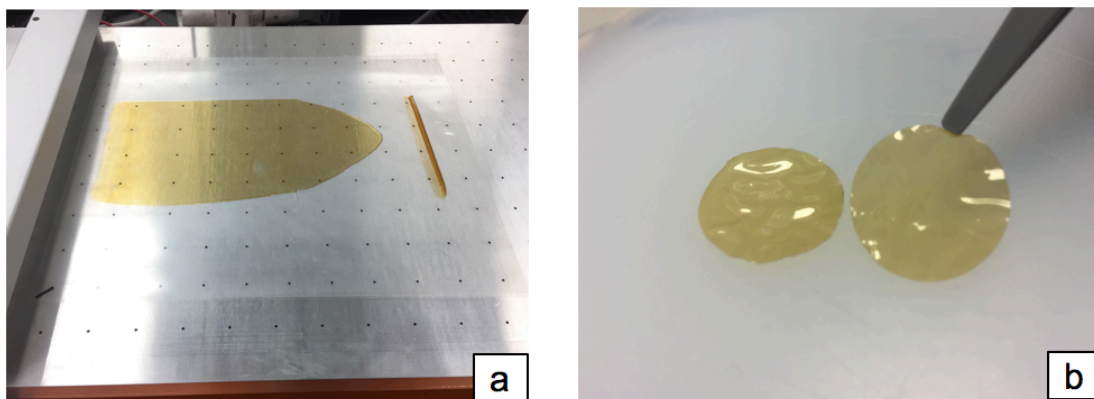
Figure 3.2 Images of (a) MPyr-Br and (b) MPyr-TFSI+Li-TFSI/PYR$_{14}$-TFSI solid-state films (thickness $\simeq$ 28 μm). Reprinted with permission from ref[104].

3.2.3 Characterization

Polymer films were analyzed with a Fourier transform infrared-attenuated total reflectance (FTIR-ATR) spectrometer (Nicolet 6700 Series, ThermoElectron) equipped with a single reflection diamond ATR accessory (Quest, Specac). All spectra were collected using a liquid nitrogen-cooled mercury-cadmium-telluride (MCT) detector at 32 scans per spectrum with a resolution of 4 and data spacing 1.928 cm^{-1}. The bare ATR crystal was collected as background spectrum and subtracted from each experiment spectrum. Differential scanning calorimetry (DSC) experiments were performed using a differential scanning calorimeter (Q200, TA Instruments) over the temperature range of -140 to 200 °C with the heating rate of 10 °C min^{-1} under nitrogen environment using a heat/cool/heat method. Glass transition temperatures (T$_g$s) were determined from the second thermogram heating cycle by the midpoint method. Thermal gravimetric analysis

(TGA; Q50, TA Instruments) was performed from ambient temperature to 900 °C at a 10 °C min^{-1} heating rate under nitrogen atmosphere (60 ml min^{-1}). Thermal degradation temperatures (T_ds) were determined at 5 wt% mass loss.

Small angle X-ray scattering (SAXS) data were collected using a Rigaku SMAX-3000 instrument at the U.S. Army Research Laboratory. A rotating Cu anode operated at 40 kV and 30 mA was used to generate characteristic Cu X-rays with wavelength (λ) of 1.542 Å. The incident X-ray beam was collimated using a focusing optic and three pinholes in a 1.5 m evacuated flight path. Samples were characterized at a sample-to-detector distance of 1.5 m using a Gabriel type 2D multi-wire xenon proportional counter. The data were corrected for background noise and averaged azimuthally to give intensity as a function of momentum transfer magnitude, I(q), where q = 4π (sin θ)/λ and 2θ is the scattering angle. The range of q spanned was from 0.007 Å^{-1} to 0.25 Å^{-1}. Data reduction and analysis were performed using Igor Pro v.7 (WaveMetrics, Inc) using procedures available from Argonne National Laboratory.[139-140] For elevated temperature measurements, samples were mounted in an environmental control cell (SAXLAB) with Kapton windows and characterized at intervals of 10 °C, ranging from 20 °C up to a maximum of 90 °C. The temperature of the cell was maintained using a temperature controlled liquid circulator (Julabo). During operation, the cell was left open to vacuum in the SAXS sample chamber. Samples were allowed to equilibrate at each temperature for 30 minutes prior to data collection. No evidence of sample degradation was noted.

Mechanical properties were analyzed with a dynamic mechanical analyzer (DMA; Q800, TA instruments) equipped with humidity chamber. Rectangular samples (20 × 5 ×

65

0.03 mm) were tested using a tension clamp. Tensile properties were measured with a strain rate of 0.2% min^{-1} at 25 °C in nitrogen at 5% RH.

3.2.4 Electrochemical Measurements

All the electrochemical test cells were prepared and assembled in an argon-purged glovebox (both water and oxygen concentrations < 5 ppm). Ionic conductivity and linear voltammetry were measured with an impedance analyzer (Solartron 1260) and potentiostat/galvanostat (Solartron 1287), respectively. A two-electrode cell was used for ionic conductivity measurements, where SPEs were sandwiched between two stainless steel solid blocking electrodes (surface area = 1.2161 ± 0.0015 cm^2) within a sealable Teflon custom-made cell [141]. Impedance scans (Nyquist plots) were measured at 10 mV amplitude over a frequency range of 1 MHz to 1 Hz at open circuit potential at a temperature range of 28 to 105 °C controlled by heating tape (BriskHeat; XtremeFLEXSDC) and a digital temperature controller with J type thermocouple (Model 650, OMEGA). SPEs were equilibrated for at least 1.5 h at each temperature. Ionic conductivity was calculated by using the following equation: $\sigma = L/AR$, where L and A is the thickness and cross-section area of the SPE, respectively; resistance, R, was determined from the semi-circle regression of high x-intercept from the Nyquist plot.

Electrochemical stability was determined *via* linear sweep voltammetry (LSV) with conductive carbon as working electrode and lithium metal as counter and reference electrodes. The test cell was assembled in an argon-filled glove box by sandwiching the SPE films between lithium ribbon (counter and reference electrode, 12 mm diameter) and

conductive carbon electrode (working electrode, 12 mm diameter) in a CR2032 coin cell. Additional drops of 1.0 M Li-TFSI/IL (80 mg) were added to each electrode during assembly to improve the contact between electrodes and SPE. Cells were then pressed twice using an electric coin cell crimper (MSK-160D, MTI). The cell was examined at a voltage rate of 1 mV s^{-1} from -1 to 6 V (*vs.* Li/Li$^+$) under ambient temperature.

The SPE cyclability and stability with lithium metal was evaluated using a battery tester (4200M, MACCOR) by stripping and plating. The test cell was assembled by sandwiching the lithium ion conducting SPE between two lithium ribbons (12 mm diameter) using similar assembly process as described above. Symmetrical lithium metal/SPE/lithium metal cells were examined under constant current (0.02 mA cm^{-2}, reversed polarization every 1h) at 70 °C controlled by a temperature chamber (MTC-020, MACCOR). Impedance scans were collected with an impedance analyzer every 10th polarization cycle at 10 mV amplitude at a frequency range of 100 kHz to 1 Hz.

3.3 Results and Discussion

Ion exchange metathesis of the SPEs from bromide ion form to TFSI ion form were confirmed by ATR-FTIR spectroscopy (shown in Figure 3.3). Four additional infrared bands representing the TFSI anion can be observed for both MIm-TFSI and MPyr-TFSI PILPTP films. The infrared band at 1348 cm^{-1} represents the SO$_2$ stretching vibration, while the band at 1053 cm^{-1} corresponds to a S-N-S antisymmetric stretching. The infrared bands at 1133 and 1180 cm^{-1} correspond to CF$_3$ stretching vibration.[142-143] In addition, the hydrophilic bromide-conducting PILPTP films exhibit a broad infrared band at 3380 cm^{-}

[1] corresponding to absorbed water. This band is not evident in the hydrophobic TFSI-exchanged PILPTP films. This further confirms successful anion exchange results, where water is negligible in TFSI-exchanged PILPTP films.
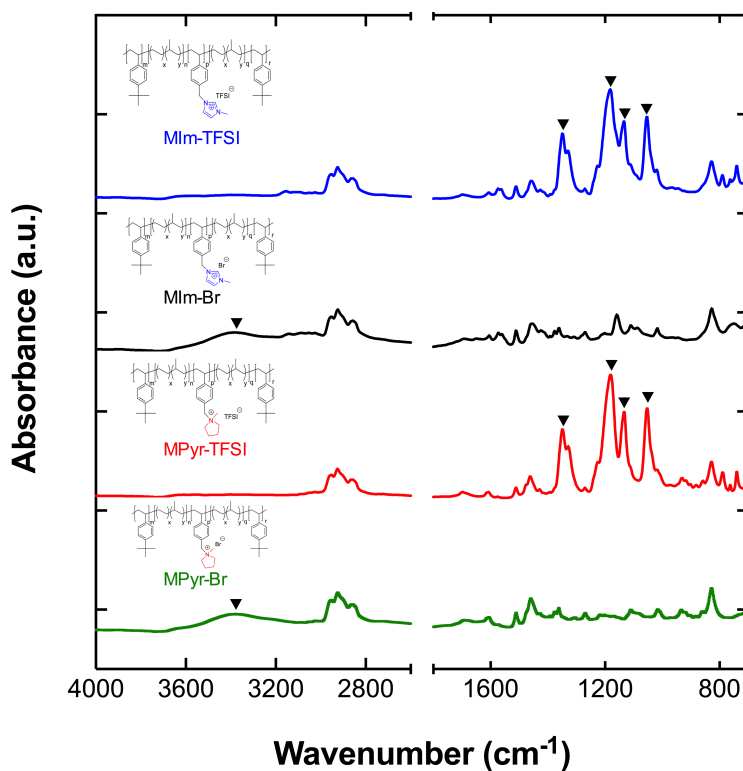
Figure 3.3 ATR-FTIR spectra of MIm-Br (black), MPyr-Br (green), MIm-TFSI (blue), and MPyr-TFSI (red). Reprinted with permission from ref[104].

Figure 3.4 shows selected stripping and plating cycles and cell overvoltage for 500 cycles for both SPEs (MIm-TFSI+Li-TFSI/EMIm-TFSI, Figure 3.4a; MPyr-TFSI+LiTFSI/PYR$_{14}$-TFSI, Figure 3.4b). Both SPEs exhibit smooth overvoltage profiles over 500 cycles. Over the 500 cycles, the MPyr-TFSI+Li-TFSI/PYR$_{14}$-TFSI remains in a relatively constant cell overvoltage window of *ca.* 10 mV, while MIm-TFSI+Li-

TFSI/EMIm-TFSI increases in its cell overvoltage window from *ca.* 5 to 20 mV. These results show a greater stability of SPE with pyrrolidinium cation and its outstanding ability to suppress polarization degradation. These smooth overvoltage profiles also indicate that no lithium dendrite formation occurs.[91]

Figure 3.4c, d show the impedance response (recorded after every 50 cycles) for both SPEs. The typical semi-circle impedance response was observed corresponding to the interfacial properties of the electrolyte (SPE) with the lithium electrode. The impedance response (Nyquist plot) was regressed to an equivalent circuit model (illustrated in Figure 3.5) to determine all of the resistances in the entire cell. The overall interfacial resistance (R_i) is composed of the passive layer resistance (R_p) from the solid electrolyte interface (SEI) and the charge transfer resistance (R_{ct}) between electrode and electrolyte; *i.e.*, $R_i = R_{ct} + R_p$.[62, 144] The electrolyte bulk resistance (R_b) and interfacial resistance (R_i) were evaluated as a function of selected cycles and are shown in the insets of Figure 3.4c, d. The R_is for both SPEs increase during an initial period. The R_i for the MPyr-TFSI+Li-TFSI/PYR$_{14}$-TFSI increases from 71 to 109 Ω after 50 cycles and then decreases and then stabilizes at 75 Ω after 150 cycles, whereas the R_i of MIm-TFSI+Li-TFSI/EMIm-TFSI stabilizes after 300 cycles. Additionally, the R_b of MPyr-TFSI+Li-TFSI/PYR$_{14}$-TFSI remains stable (*ca.* 10 mV) during the entire 500 cycles, while the R_b of MIm-TFSI+Li-TFSI/EMIm-TFSI increases during the same cycle span (*ca.* 10 to 45 mV). The increases in R_is correspond to the formation of a passivated layer on the Li metal.[145] The passivation of the Li metal anode is considered a promising method to enhance the SEI layer and reduce dendrite growth.[146] The R_i stability of the SPEs in this study indicates the good

interfacial contact between the lithium electrode and the SPE and enhanced SEI layer stability. Results from cell overvoltage and R_i suggest that both SPEs have the ability to prevent lithium dendrite growth. Moreover, the cell overvoltage profiles can be correlated with the R_b of the SPEs; typically, stable R_b correlates to stable polarization profiles and *vice versa* (*i.e.*, MPyr-TFSI + Li-TFSI/PYR$_{14}$-TFSI). The above behaviors are also in an agreement with the *post mortem* images of the lithium electrode and SPEs shown in Figure 3.6. After 500 cycles, post mortem analysis also revealed no observable IL leakage. This may be attributed to the non-volatility of the IL and the chemical compatibility and strong ionic interactions between the IL and PILPTP. Overall, the stripping and plating results demonstrate the promising cycling stability of the SPEs with lithium metal electrodes, specifically the MPyr-TFSI+Li-TFSI/PYR$_{14}$-TFSI SPE with outstanding stability with lithium metal over 500 stripping and plating cycles.[147]
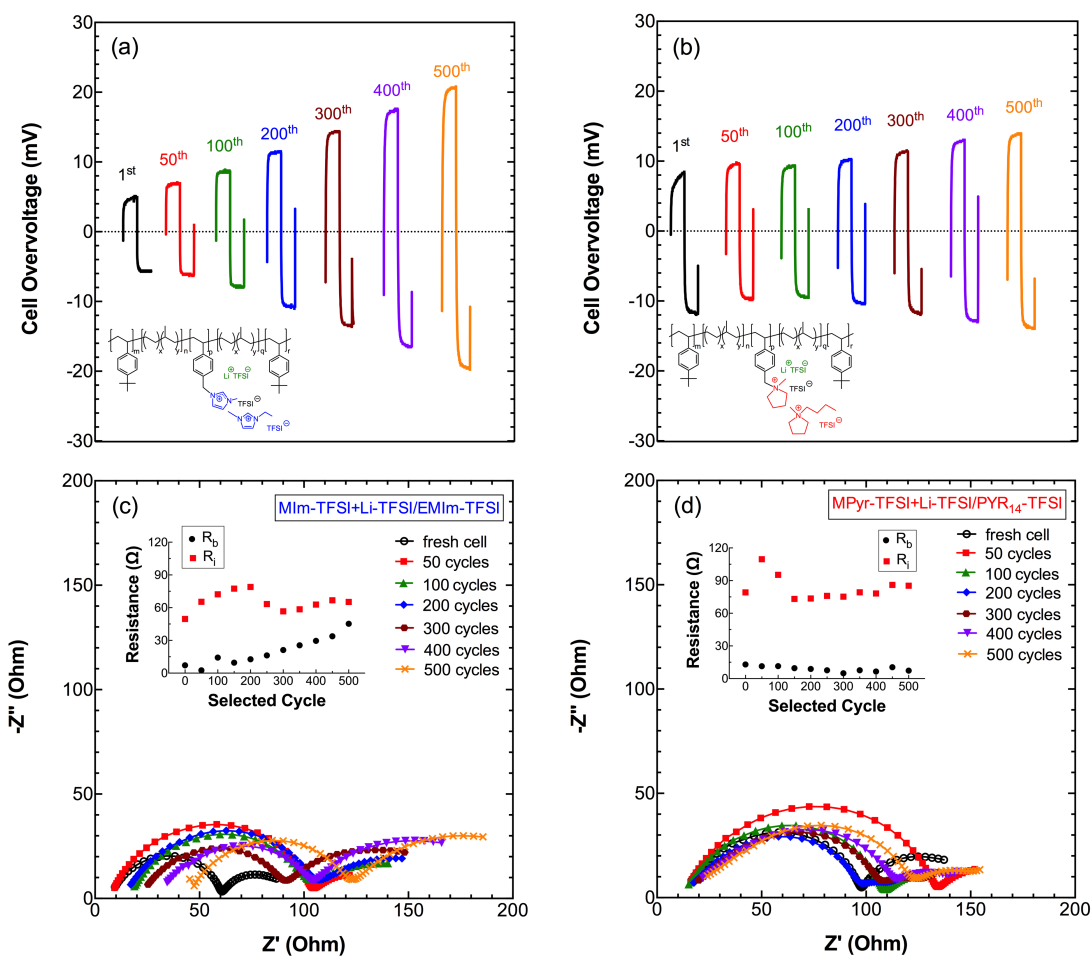
Figure 3.4 Selected stripping-plating cycles with symmetric Li / SPE / Li cell under 0.02 mA cm^{-2} and impedance spectra at the end of each selected cycles at 70 ºC of (a, c) MIm-TFSI+Li-TFSI/EMIm-TFSI and (b, d) MPyr-TFSI+Li-TFSI/PYR$_{14}$-TFSI. Insets correspond to interfacial resistance and electrolyte bulk resistance of selected cycles. Reprinted with permission from ref[104].

R_b = electrolyte bulk resistance R_{ct} = charge transfer resistance
Z_w = diffusive impedance C_{dl} = double layer capacitance
    R_p = passive layer resistance
    C_p = passive layer capacitance
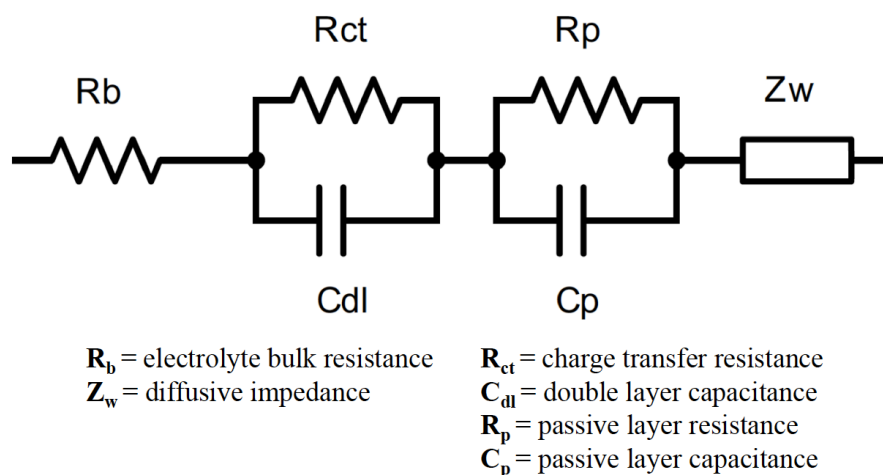
Figure 3.5 Equivalent circuit model adopted for fitting the impedance response of Figure 3.4. Reprinted with permission from ref[104].
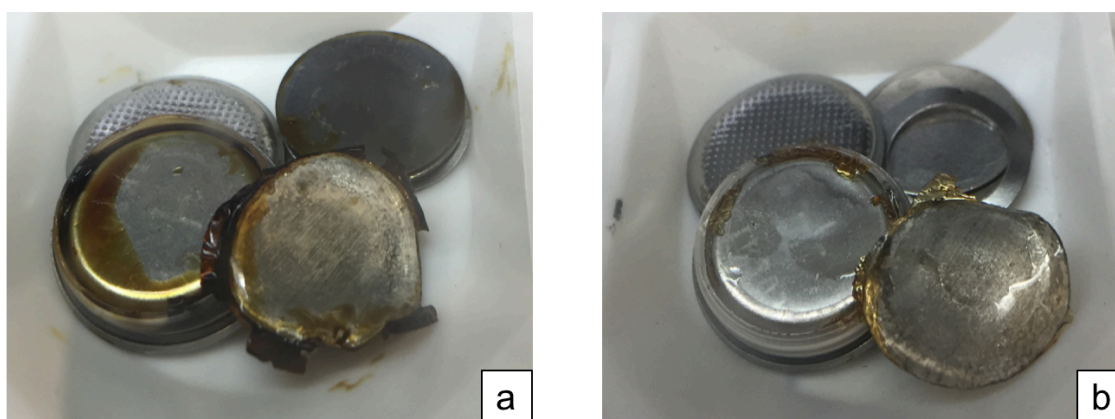
Figure 3.6 *Post mortem* images of disassembled coin cells for (a) MIm-TFSI+Li-TFSI/EMIm-TFSI and (b) MPyr-TFSI+Li-TFSI/PYR14-TFSI after 500 cycles of stripping and platting. Reprinted with permission from ref[104].

Figure 3.7 shows the electrochemical stability windows of both SPEs measured *via* linear sweep voltammetry within a -1 to 6 V (*versus* Li/Li⁺) voltage range. The results show that the MIm-TFSI+Li-TFSI/EMIm-TFSI and MPyr-TFSI+Li-TFSI/PYR$_{14}$-TFSI

have overall potential stability windows of *ca.* 2.2 and 4.8 V, respectively. A reduction

peak for each SPE was observed: -0.5 V *versus* Li/Li$^+$ for MPyr-TFSI+Li-TFSI/PYR$_{14}$-

TFSI and 1.8 V *versus* Li/Li$^+$ for MIm-TFSI+Li-TFSI/EMIm-TFSI. The electrochemical

stability of an electrolyte plays an important role in deciding the operating voltage window

for a battery and subsequently choosing the appropriate cathode material. Generally, the

anodic limit is the oxidation of the anion and the cathodic limit is the reduction of the

cation.[148] The reduction peak between -1 to 0 V *versus* Li/Li$^+$ for the MPyr-TFSI+Li-

TFSI/PYR$_{14}$-TFSI is associated with the lithium stripping/plating.[149] The reduction peak

or cathodic limit of 1.8 V *versus* Li/Li$^+$ for MIm-TFSI+Li-TFSI/EMIm-TFSI indicates the

reduction of imidazolium cation, which is significantly influenced by the presence of the

proton at the C2 position of the imidazole ring.[150-151] Compared to the pyrrolidinium cation,

which is a saturated heterocyclic cation,[152] the unsaturated heterocyclic imidazolium

cation is more easily reduced due to the presence of the vacant π^* orbital. The acidity

related to the presence of a proton at the C2 position on imidazolium ring also influences

the cation reduction.[153] The anodic limits of 4 and 4.8 V *versus* Li/Li$^+$ for the two SPEs,

respectively, correspond to the oxidation of TFSI anion in both SPEs. The MPyr-TFSI+Li-

TFSI/PYR$_{14}$-TFSI SPE exhibits an outstanding overall operating voltage window of 4.8

V under room temperature due to the notable electrochemical stability of pyrrolidinium

cation and TFSI anion, which is compatible with the commercial electrode materials

(typical operating range 3.0 to 4.2 V *versus* Li/Li$^+$ for lithium cobalt oxide and lithium

iron phosphate). The stability window under room temperature for the MPyr-TFSI+Li-

TFSI/PYR$_{14}$-TFSI SPE is also comparable to the other SPE results in the literature (*ca.* 4

to 5 V *versus* Li/Li$^+$) which are usually examined under higher temperatures (40 to 80 °C).[62, 85, 154]
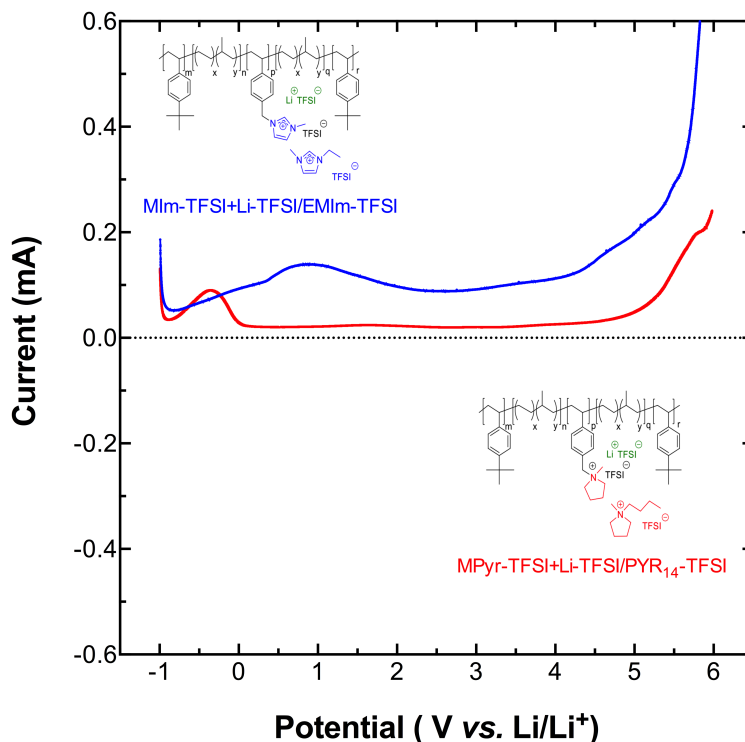
Figure 3.7 Linear voltammetry (electrochemical stability) of MIm-TFSI+Li-TFSI/EMIm-TFSI (blue) and MPyr-TFSI+Li-TFSI/PYR$_{14}$-TFSI (red) at a scan rate of 10 mV s^{-1} with carbon working electrode and Li counter and reference electrode under room temperature. Reprinted with permission from ref[104].

Figure 3.7 shows the temperature-dependent (28 to 105 °C) ionic conductivity under a dry condition (in an argon-filled glove box) for both SPEs. The conductivities of both SPEs increase with increasing temperature and follow the Vogel-Fulcher-Tammann (VFT) trend, where at a lower temperature (28 °C), MIm-TFSI+Li-TFSI/EMIm-TFSI (1.0 × 10^{-4} S cm^{-1}) is two orders of magnitude higher than MPyr-TFSI + Li-TFSI/PYR$_{14}$-TFSI (9.1

$\times$ 10^{-7} S cm^{-1}), while at a higher temperature (105 °C), MIm-TFSI+Li-TFSI/EMIm-TFSI

(1.31 $\times$ 10^{-3} S cm^{-1}) is one order of magnitude higher than MPyr-TFSI + Li-TFSI/PYR$_{14}$-

TFSI (1.21 $\times$ 10^{-4} S cm^{-1}). Comparing with other studies, ionic conductivity of MIm-

TFSI+Li-TFSI/EMIm-TFSI at 28 °C is one to two orders of magnitude higher than the

single-ion conducting SPEs (*ca.* 10^{-5} - 10^{-7} S cm^{-1} at 28 °C)[154-155] and also comparable with

other PIL SPEs (*ca.* 10^{-4} S cm^{-1} at 28 °C).[62, 85]

In Figure 3.8, the conductivity data was regressed to the VFT equation[116-117]:

$$\sigma(T) = \sigma_0 \exp\left(-\frac{b}{T-T_0}\right) \qquad\qquad (3.1)$$

where σ_0 (S cm^{-1}) is infinite temperature conductivity, which is proportional to the free

ion concentration,[156-157] b (K) is the constant related to the activation energy required for

ion motion, and T_0 (K) is the Vogel temperature that ion motion first occurs. The resulting

VFT fitting parameters are listed in Table 3.2. MIm-TFSI+Li-TFSI/EMIm-TFSI exhibits

higher σ_0 (23.9 mS cm^{-1} *versus* 10 mS cm^{-1}) and lower b (429.8 K *versus* 660.8 K) than

MPyr-TFSI+Li-TFSI/PYR$_{14}$-TFSI. Segalman *et al.*[158] suggested that the b parameter can

provide information in relation to decoupling ionic conductivity from structural relaxation

of the SPE, where SPEs with lower b parameters might indicate stronger decoupling of

ionic conductivity from segmental relaxation, which could be more promising on

achieving higher ionic conductivity at room temperature.[159-160] The VFT regression results

and the corresponding ionic conductivity trends are comparable with other PIL block

copolymers in the literature.[158] The ionic conductivity results show that the cation group

significantly affect ion mobility. This may be attributed to the delocalized positive charge

on the imidazolium cation, which can improve the degree of dissociation of ions compared

to the localized positive charge in the pyrrolidinium cation, which may deter the facile dissociation of ions.[108-109] The conductivity differences in this study between the imidazolium and pyrrolidinium cation corroborates with other studies on PILs and ILs with these cations.[161-162] Overall, the high ionic conductivity (1×10^{-3} S cm^{-1} at 84 °C) of the MIm-TFSI+Li-TFSI/EMIm-TFSI SPE is favorable for application to lithium ion batteries.[163]
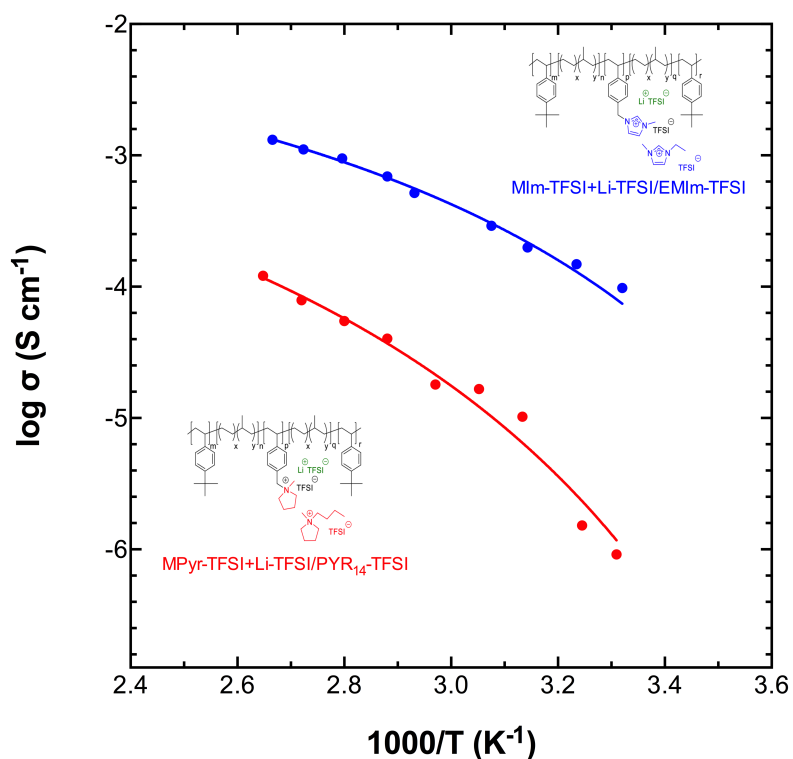
Figure 3.8 Temperature-dependent dry (H_2O < 5 ppm) ionic conductivity and Vogel-Fulcher-Tammann (VFT) regressions (solid lines) of MIm-TFSI+Li-TFSI/EMIm-TFSI (blue) and MPyr-TFSI+Li-TFSI/PYR$_{14}$-TFSI (red). Reprinted with permission from ref[104].

Table 3.2 Vogel-Fulcher-Tammann (VFT) equation regression results. Reprinted with permission from ref[104].

	σ_0 (mS cm^{-1})	b (K)	T_0 (K)
MIm-TFSI+Li-TFSI/EMIm-TFSI	23.9	429.8	226.8
MPyr-TFSI+Li-TFSI/PYR$_{14}$-TFSI	10.0	660.8	229.1

Figure 3.9 shows the SAXS data for both SPEs under vacuum at elevated temperatures (20 to 90 °C). From SAXS profiles at 20 °C, both samples show a single primary scattering maximum centered at *ca.* q = 0.015 Å^{-1}, corresponding to a correlation length of *ca.* 420 Å. A shoulder located at q $\approx$ 0.032 Å^{-1} is observed at 60 °C for the MIm-TFSI+Li-TFSI/EMIm-TFSI (Figure 3.9a) and 50 °C for the MPyr-TFSI+Li-TFSI/PYR$_{14}$-TFSI (Figure 3.9b). This shoulder disappears as the samples are heated above 50 °C and 60 °C, respectively. The average interdomain spacing (d* = 2π/q*) can be measured by recording the position of the primary scattering maximum, q* (listed in Table 3.3). The MPyr-TFSI+Li-TFSI/PYR$_{14}$-TFSI SPE has a slightly larger q* value (0.0159 Å^{-1} *versus* 0.0155 Å^{-1} at 20 °C), indicating that the average interdomain spacing for the SPE is slightly less than in the MIm-TFSI+Li-TFSI/EMIm-TFSI (*e.g.,* d* = 39.5 nm for MPyr-TFSI+Li-TFSI/PYR$_{14}$-TFSI and d* = 40.5 nm for MIm-TFSI+Li-TFSI/EMIm-TFSI at 20 °C). Overall, the SAXS profiles indicate that both SPEs are microphase-separated from room temperature up to 90 °C and that the average interdomain distance is relatively constant between the two materials, but with MIm-TFSI+Li-TFSI/EMIm-TFSI having a slightly larger spacing between domains. Both materials undergo a weak order-disorder transition between 50 °C and 70 °C.
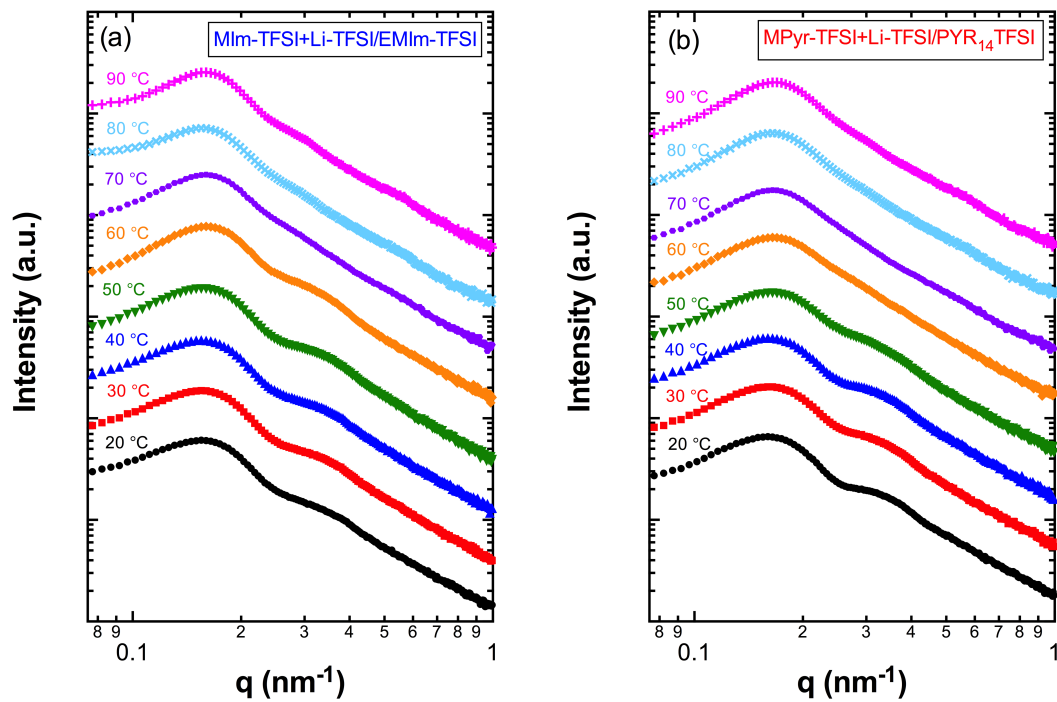
Figure 3.9 Temperature-dependent small-angle X-ray scattering (SAXS) profiles of (a) MIm-TFSI+Li-TFSI/EMIm-TFSI and (b) MPyr-TFSI+Li-TFSI/PYR$_{14}$-TFSI measured from 20 to 90 ºC under vacuum. Reprinted with permission from ref[104].

Table 3.3 Position of the primary scattering maximum. Reprinted with permission from ref[104].

Temperature (°C)	$q*$ (Å^{-1})	
	MIm-TFSI+Li-TFSI/EMIm-TFSI	MPyr-TFSI+Li-TFSI/PYR$_{14}$-TFSI
20	0.0155	0.0159
30	0.0155	0.0161
40	0.0154	0.0161
50	0.0156	0.0164
60	0.0160	0.0166
70	0.0160	0.0166
80	0.0155	0.0165
90	0.0158	0.0167

Figure 3.10 shows the DSC thermograms (glass transition temperatures) for both cation type polymers in the bromide-conducting form, TFSI-exchanged form, and lithium ion conducting PILPTP SPE form. The bromide-conducting block polymers exhibit two T_gs (indicative of phase separation), where the lower T_g is common to both at -51 °C and this corresponds to the B block (ethylene-*r*-propylene), while the higher T_g differs between both and this corresponds to the middle C block (PIL). The bromide-conducting block polymer with imidazolium cation (MIm-Br) containing C block exhibits a lower T_g compared to the one with pyrrolidinium cation (MPyr-Br): 127 °C *versus* 156 °C. This result corroborates with the previous studies on ILs and PILs with imidazolium and pyrrolidinium cations.[136, 161-162, 164] The TFSI-exchanged block polymers also exhibit two T_gs (also indicative of phase separation). Similar to the bromide-conducting block polymers, the lower T_g is common among both at -49 °C and this corresponds to the B block (ethylene-*r*-propylene). The higher T_gs correspond to the PIL C block and differ among the block polymers: 64 °C (MIm-TFSI) *versus* 70 °C (MPyr-TFSI). This T_g

depression from bromide ion form to TFSI ion form corroborates with other reports on PILs with these same anions, where the larger fluorine-containing anion acts as a pseudo-plasticizer in comparison to the smaller halide anion.[165] For the lithium ion conducting SPEs, only one distinct T_g was observed in each SPE at -61 °C (MIm-TFSI+Li-TFSI/EMIm-TFSI) and -63 °C (MPyr-TFSI+Li-TFSI/PYR$_{14}$-TFSI). This suggests that the addition of the salt/IL depresses the T_g of the ion containing C blocks considerably, where these low T_gs approach the T_gs of the reported corresponding pure ILs: EMIm-TFSI (-98 °C) and PYR$_{14}$-TFSI (-87 °C).[166] Despite the evidence of only one T_g for the lithium ion conducting SPEs, phase separation in these polymers are still evident in the SAXS results (Figure 3.9). Previous work suggests that both phase separation and a low T_g in the conducting block is conducive for the orthogonal properties of high mechanical strength and high ion mobility.[48]
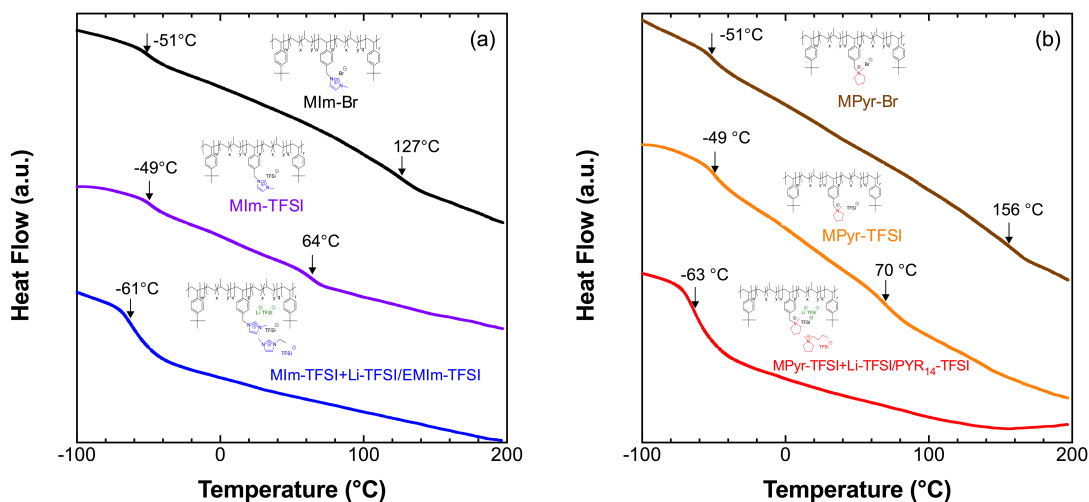
Figure 3.10 Differential scanning calorimetry profiles of (a) MIm-Br (black), MIm-TFSI (purple), and MIm-TFSI+Li-TFSI/EMIm-TFSI (blue); (b) MPyr-Br (brown), MPyr-TFSI (yellow), and MPyr-TFSI+Li-TFSI/PYR$_{14}$-TFSI (red). Reprinted with permission from ref[104].

Figure 3.11 shows the thermal stability of both lithium ion conducting SPEs examined by TGA under a nitrogen environment. The degradation temperatures (T_d) were measured at 5 wt% loss and both SPEs exhibit T_ds greater than > 300 ºC. Both samples exhibit a one-step thermal decomposition. Thermal stability is a key parameter for SPE regarding battery performance and safety, where the degradation temperatures reported here are much higher than standard maximum battery operating temperatures. Similar to previous studies, ILs containing the TFSI anion exhibit excellent thermal stability due to the low nucleophilicity of fluorine containing anion.[167-168] Therefore, the TFSI anion aids in the high decomposition temperature of the lithium conducting SPEs. The small differences in the decomposition temperatures among the two different SPEs could be related to the

higher thermal stability of saturated pyrrolidinium cations compared to unsaturated imidazolium cations.[169]
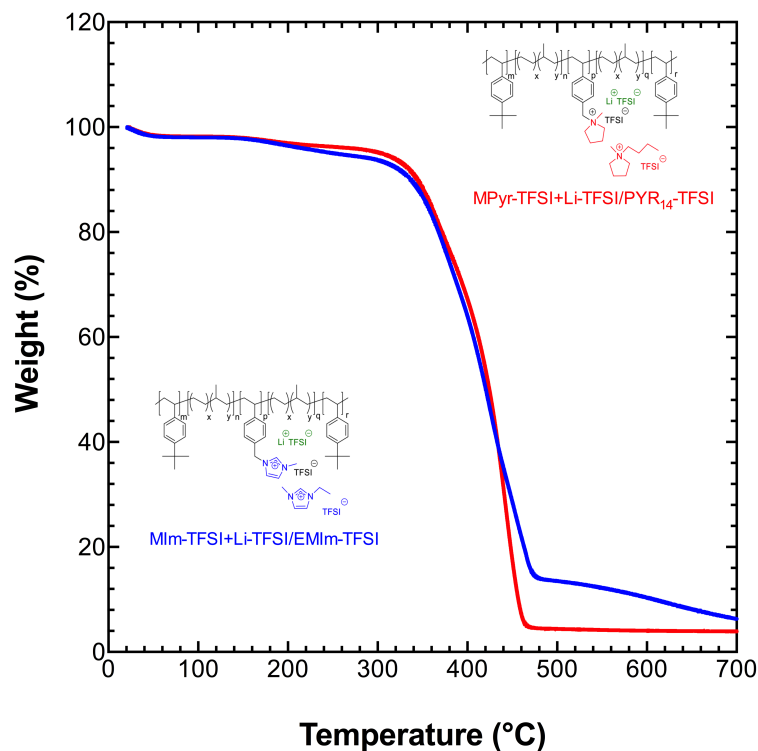
Figure 3.11 Thermogravimetric analysis profiles of MIm-TFSI+Li-TFSI/EMIm-TFSI (blue), and MPyr-TFSI+Li-TFSI/PYR$_{14}$-TFSI (red). Reprinted with permission from ref[104].

Mechanical strength of both SPEs were measured with DMA; strain-stress profiles are shown in Figure 3.12. Elastic modulus, ultimate tensile strength, and elongation break results from strain-stress profile are listed in Table 3.4. The MIm-TFSI+Li-TFSI/EMIm-TFSI sample reveals higher tensile properties than MPyr-TFSI+Li-TFSI/PYR$_{14}$-TFSI, *i.e.*, elastic modulus of 8.8 *versus* 0.25 MPa and ultimate tensile strength of 0.957 MPa *versus* 0.04 MPa. Both SPEs show elongation to breaks of 95.2 % and 90.8 %, respectively.

Mechanical robustness of SPE can play a critical role in suppressing Li-dendrite growth and prevent the short circuit between anode and cathode during charge-discharge, where the mechanical properties reported here are lower than other single ion conductor block copolymer SPEs.[156, 170-171] The SPEs in this study contain ILs, which results in high ion conductivities due to plasticizing effect of the ionic liquid (low T_gs of ion conductive phase), however, it also affects the mechanical properties as well [164]. With multiblock polymers, these properties can be optimized with the appropriate block polymer composition (molecular weight of each block) and block polymer/salt/IL composition (ratio of each component in ternary mixture).
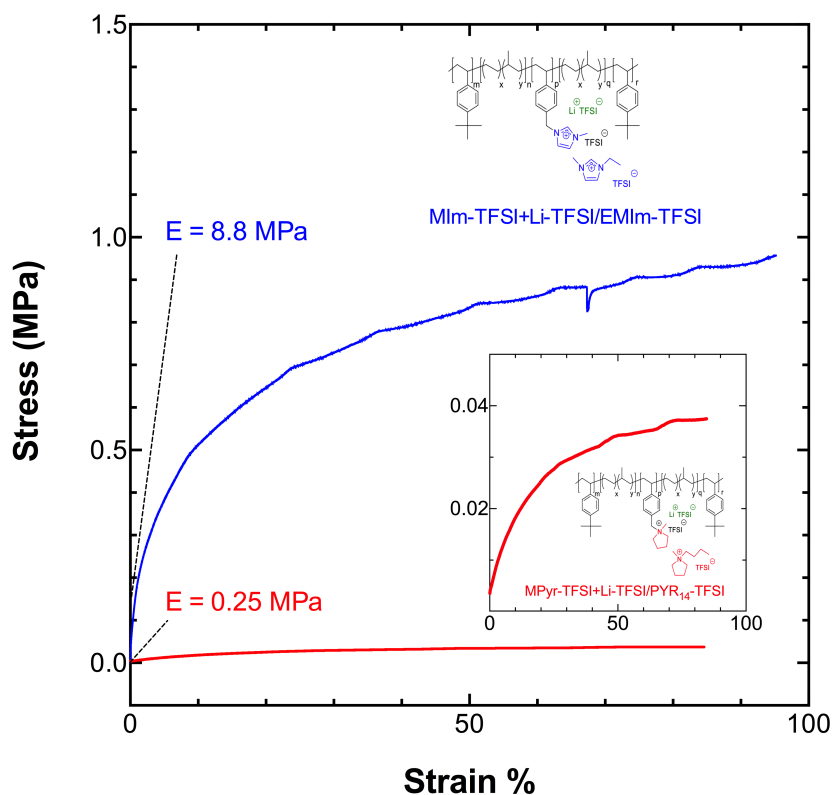
Figure 3.12 Strain-stress curves of MIm-TFSI+Li-TFSI/EMIm-TFSI (blue) and MPyr-TFSI+Li-TFSI/PYR$_{14}$-TFSI (red) at 25 ºC and 5% RH. Elastic modulus (E) was estimated from the initial slope (dashed lines). Inset corresponds to strain-stress curves of MPyr-TFSI+Li-TFSI/PYR$_{14}$-TFSI. Reprinted with permission from ref[104].

Table 3.4 Tensile properties of SPEs. Reprinted with permission from ref[104].

Sample name	Elastic modulus (MPa)	Ultimate tensile strength (MPa)	Elongation to break (%)
MIm-TFSI+LiTFSI/EMIm-TFSI	8.80	0.957	95.2
MPyr-TFSI+Li-TFSI/PYR14-TFSI	0.25	0.040	90.8

3.4 Conclusions

In this study, robust, free-standing SPEs based on a new ABCBA pentablock terpolymer (multiblock polymer), incorporating ionic liquid and lithium salt, was prepared and investigated. The impact of two different cations (imidazolium and pyrrolidinium) on the conductive block were also explored. Both SPEs exhibit degradation temperatures (T_ds) greater than 300 °C, which are much higher than standard maximum battery operating temperatures. The MIm-TFSI+Li-TFSI/EMIm-TFSI SPE exhibits a high ionic conductivity of 0.1 mS cm^{-1} at 28 °C, which is favorable for application to lithium ion batteries. The promising stability window of 4.2 V *versus* Li/Li$^+$ under room temperature for the MPyr-TFSI+Li-TFSI/PYR$_{14}$-TFSI SPE is also comparable to the other SPE results in the literature. The cycling stabilities of the SPEs with lithium metal electrodes were determined by stripping and plating under 70 °C. The MPyr-TFSI+Li-TFSI/PYR$_{14}$-TFSI SPE exhibits a stable electrolyte bulk resistance (R_b) and cell overvoltage profiles over 500 cycles, indicating its outstanding stability with lithium metal. Overall, the results from this study demonstrate that the lithium ion conducting ABCBA pentablock terpolymers have high potential as SPEs for lithium ion batteries with outstanding thermal and electrochemical stabilities and sufficient ionic conductivities.

CHAPTER IV

IMPACT OF IONIC LIQUID ON LITHIUM ION BATTERY WITH A SOLID

POLY(IONIC LIQUID) PENTABLOCK TERPOLYMER AS ELECTROLYTE

AND SEPARATOR

4.1 Introduction

In Chapter III, we prepared a robust, free-standing SPE based on a PIL multiblock copolymer (PILPTP) incorporating ionic liquid and lithium salt. The SPE demonstrates outstanding thermal and electrochemical stabilities, as well as sufficient ionic conductivities. However, solid-state ternary blend SPEs (*i.e.,* PIL (or PIL block copolymer) + lithium salt + IL) increase the complexity on optimizing the chemical, physical, and electrochemical properties due to their numerous tuning parameters (*e.g.,* polymer backbone chemistry, cation/anion chemistry and structure, IL/salt composition, *etc.*). As generally reported in the literature,[172-174] ILs mainly reside in one phase of the block copolymer and improve the polymer chain mobility, as well as lower the glass transition temperature (T_g) and enhance the salt dissociation or solvation. This suggests that by manipulating the additional IL in salt-doped PIL block copolymers, one can easily obtain SPEs with high ion conductivity and enhanced electrochemical stability. A number of recent studies on PIL(or PIL block polymer)/salt/IL blends have only focused on various IL chemistries, ionic conductivity, and battery performance,[62, 87, 89-90, 175-177] yet reported limited information regarding the modification of ion transport and stability by varying the IL concentration. Also, the plasticizing effect from the IL incorporation may improve

86

the ionic conductivity, but also influence mechanical modulus,[164, 178] where it is unclear how this will impact prolonged battery cycling.

Previously, publications that combine ILs and block copolymers have focused on neutral block copolymers.[107, 141, 179-180] Although critical insights with regard to property-conductivity relationships in IL/block copolymer have arisen, extra complexity should be considered for IL/PIL block copolymers. Compared to neutral block copolymers, PIL block copolymers have cations or anions covalently bound to the backbone with coordinated mobile counterions. Additionally, the coordination between the IL and PIL domain may affect transport-morphology relationships differently than IL/block copolymers, where ILs reside in neutral block domains solely due to high chemical affinity. For example, molecular dynamics simulations by Ganesan *et al.*[93-95] in IL/PILs suggests that anion-cation correlations and ion transport mechanisms are significantly different from those in neutral polymers. Therefore, a systematic experimental investigation on the impact of IL in IL/PIL block copolymers is warranted and could provide valuable insights into more complex solid-state electrolytes for lithium ion batteries.

In this work, the impact of imidazolium-based IL (*i.e.,* EMIm-TFSI) on a salt-doped PIL pentablock terpolymer (poly(S-b-EP-b-VBMIm-TFSI-b-EP-b-S), S = styrene; EP = ethylene-r-propylene; VBMIm-TFSI = vinylbenzylmethylimidazolium bis(trifluoromethylsulfonyl)imide) is explored in regards to ion transport, morphology, mechanical properties, electrochemical stability, and battery performance. Additionally, pulsed-field gradient nuclear magnetic resonance (PFG-NMR) was utilized to probe the self-diffusion coefficients of individual ionic species in the SPE. A systematic

experimental study on ion transport mechanisms that covers a broad range of IL compositions in a ternary solid polymer electrolyte system is still unexplored and this study provides valuable insights on optimizing complex SPEs for lithium ion batteries.

4.2 Experimental Methods

4.2.1 Materials

The non-ionic precursor ABCBA pentablock terpolymer, poly(S-*b*-EP-*b*-pmS-*b*-EP-*b*-S) (chemical structure shown in Figure 4.1), was manufactured by Kraton Polymers, LLC and received as solution in cyclohexane. The polymer contains styrene (S) as the A outer blocks, a random copolymer of ethylene-*r*-propylene (EP) as the B blocks, and para-substituted methyl styrene (pmS) as the inner C block with M_n ~88 kg mol^{-1} and M_n of respective blocks equal to 20-2-44-2-20 kg mol^{-1}.

Toluene (anhydrous, 99.8%), methanol (ACS reagent, $\geq$99.8%), *N*-methyl-2-pyrrolidone (NMP; anhydrous, 99.5%), *N*, *N*-dimethylacetamide (DMAc; anhydrous, 99.8%), lithium cobalt oxide (LiCoO$_2$; 99.8%), *N*-bromosuccinimide (NBS, 99%), 2,2´-azobis(2-methylpropionitrile) (AIBN; 98%), chlorobenzene (99.8%), 1-methylimidazole (MIm; 99%), dichloromethane-d2 (CD$_2$Cl$_2$, 99.9 atom % D, contains 0.1 % (v/v) TMS), and bis(trifluoromethylsulfonyl)imide lithium salt (Li-TFSI; 99.95%) were used as received from Sigma-Aldrich. Isopropyl alcohol (IPA, $\geq$ 99.5%) was used as received from VWR International. 1-ethyl-3-methylimidazolium bis(trifluoromethylsulfonyl)imide (EMIm-TFSI; 99%, IoLiTec) was dried under dynamic vacuum for 24 h and stored in argon-filled glove box (mBraun) before use. Lithium

titanate (Li$_4$Ti$_5$O$_{12}$; >98%), conductive graphite (≥99.98%), polyvinylidene fluoride (PVDF; ≥99.5%), conductive carbon-coated aluminum foil (0.05 mg cm^{-2}), CR2032 coin cell cases (20 mm diameter × 3.2 mm thickness) with O-rings for battery research, stainless steel spacers for CR2032 cells (15.5 mm diameter × 0.5 mm thickness, 15.5 mm diameter × 0.2 mm thickness), and stainless steel wave springs for CR2032 cases (1.2 mm height × 0.3mm thickness) were used as received from MTI Corporation. Mylar PET release liner substrates (Grade 26965, 0.0762 mm) were used as received from LOPAREX. Deionized (DI) water with resistivity *ca.* 16 MΩ cm was used as appropriate.
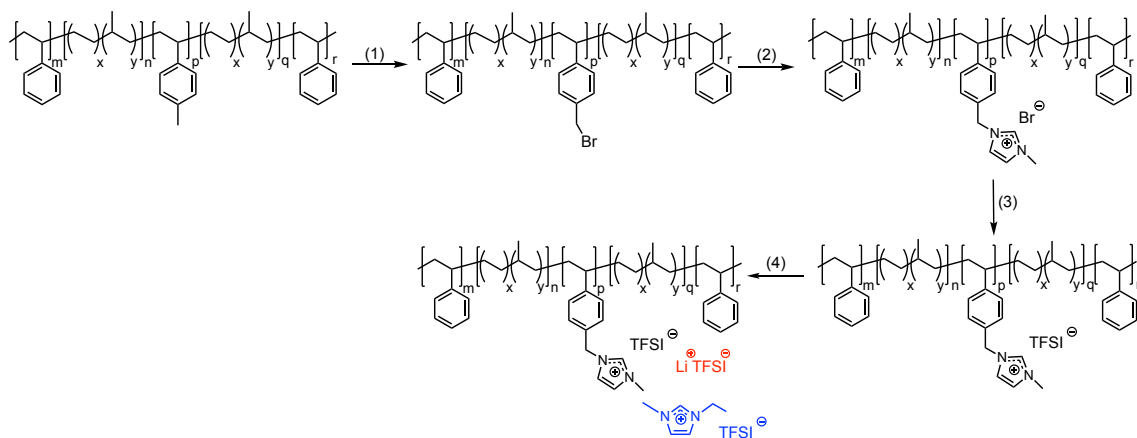
(1) AIBN, NBS, chlorobenzene, 70 ℃, 10 h; (2) 1-methylimidazole, toluene, methanol, room temperature, 48 h; (3) Li-TFSI, toluene, methanol, room temperature, 48 h; (4) Li-TFSI, 1-ethyl-3-methylimidazolium bis(trifluoromethylsulfonyl)imide, *N, N*-dimethylacetamide, room temperature

Figure 4.1 Synthesis of lithium ion conducting PILPTP.

4.2.2 Synthesis of poly(S-b-EP-b-VB-Br-b-EP-b-S) *via* Bromination

Bromine was covalently attached to the pmS midblock of the non-ionic precursor polymer, poly(S-*b*-EP-*b*-pmS-*b*-EP-*b*-S), *via* bromination (Figure 4.1, step 1). The non-

ionic precursor polymer was first precipitated and extensively washed with isopropyl alcohol (isopropyl alcohol/polymer, 6/1, w/w), followed by drying under vacuum at 50 °C for 12 h prior to the bromination reaction. A typical example of a bromination reaction is given as follows. 192.19 g of chlorobenzene was added into a three-neck round bottom flask equipped with a condenser followed by purging with nitrogen at room temperature continuously overnight under reflux. Subsequently, 10.0163 g poly(S-*b*-EP-*b*-pmS-*b*-EP-*b*-S) was transferred into the chlorobenzene and stirred until fully dissolved. The solution was heated to 70 °C and stirred in dark with continuous nitrogen purge. NBS (1.4469 g, 8.13 mmol) and AIBN (0.0670 g, 0.41 mmol) were added to the solution every 30 min for 10 additions. After the last addition, the reaction was stirred for 30 min and subsequently terminated by cooling the flask in liquid nitrogen. The resulting brominated polymer, poly(S-*b*-EP-*b*-VB-Br-*b*-EP-*b*-S) [VB-Br = vinylbenzyl bromide], was precipitated and extensively washed in methanol (methanol/polymer, 4/1 w/w) and then filtered and dried under vacuum at 50 °C for 24 h. Yield: 14.37 g of yellow solid particles. Degree of bromination (DB) was determined to be 94 % by ^{1}H NMR spectroscopy. NMR: 7.75-6.00 (m, C$_6$H$_5$, C$_6$H$_4$-CH$_2$-Br, C$_6$H$_4$-CH$_3$), 4.80-4.10 (s, C$_6$H$_4$-CH$_2$-Br), 2.55-2.17 (m, C$_6$H$_4$-CH$_3$), 2.16−0.75 (m, CH$_2$-CH, CH$_2$-CH, *(CH$_2$-CH$_2$)$_x$-(CH(CH$_3$)-CH$_2$)$_y$)*.

4.2.3 Synthesis of Bromide Ion Conducting PILPTP

The bromide ion conducting PILPTP (PTP-Br) was prepared by quaternization of poly(S-*b*-EP-*b*-VB-Br-*b*-EP-*b*-S) with 1-methylimidazole (Figure 4.1, step 2). The resulting ion-conducting polymer, poly(S-*b*-EP-*b*-VBMIm-Br-*b*-EP-*b*-S) [VBMIm-Br =

vinylbenzylmethylimidazolium bromide], is referred to as PTP-Br. A typical example of the quaternization of PTP-Br is given as follows. Poly(S-*b*-EP-*b*-VB-Br-*b*-EP-*b*-S) was first dissolved in toluene (toluene/poly(S-*b*-EP-*b*-VB-Br-*b*-EP-*b*-S), 4.4/1, w/w) in a 40 mL vial and mixed at room temperature for 3 h on a tube roller (SCILOGEX, MX-T6-S) to achieve a homogeneous solution. Subsequently, 1-methylimidazole and methanol (toluene/poly(S-*b*-EP-*b*-VB-Br-*b*-EP-*b*-S)/1-methylimidazole/methanol, 4.4/1/0.22/1.1, w/w/w/w) were added in the solution and mixed at room temperature for at least 48 h before use.

4.2.4 Preparation of Lithium Ion Conducting PILPTP Films

A TFSI-exchanged PILPTP (poly(S-*b*-EP-*b*-VBMIm-TFSI-*b*-EP-*b*-S) [VBMIm-TFSI = vinylbenzylmethylimidazolium bis(trifluoromethane)sulfonimide], referred to as PTP-TFSI) was then prepared *via* anion exchange metathesis of the PTP-Br (Figure 4.1, step 3). A bis(trifluoromethane)sulfonimide lithium salt (Li-TFSI) solution was prepared by dissolving Li-TFSI (Li-TFSI:PTP-Br = 9:1 mol/mol) in 50 mL toluene/methanol (4/1 w/w) solvent. The Li-TFSI solution was added dropwise into the PTP-Br solution under continual mixing at room temperature. The solution was stirred at room temperature for 48 h. The resulting PTP-TFSI was then precipitated with excess methanol (500 mL) overnight, followed by multiple washes with methanol to remove excess TFSI anions and toluene. Residual solvent was removed by filtering and drying the polymer under vacuum in an oven at room temperature for 24 h. The dried PTP-TFSI was then dissolved in DMAc at a concentration of 0.33 g mL^{-1} and mixed with the desired proportions of ionic liquid

(1-ethyl-3-methylimidazolium bis(trifluoromethylsulfonyl)imide, EMIm-TFSI) and Li-TFSI to obtain [Li]/[PVBMIm-TFSI] = 0.1 (mol/mol) ([PVBMIm-TFSI] = poly(vinylbenzylmethylimidazolium bis(trifluoromethylsulfonyl)imide); conductive block in pentablock terpolymer) and various r = [EMIm-TFSI]/[PVBMIm-TFSI] (mol/mol) ratios (Table 4.1; Figure 4.1, step 4). The ternary mixture (PTP-Li-r, Table 4.2) was mixed for 3 h at room temperature. The PTP-Li-r SPEs were then fabricated by casting the ternary mixture solution onto a silicon-coated Mylar PET film using an automatic film applicator (Elcometer 4340) with doctor blade at gauge height and speed of *ca*. 400 μm and 60 mm s^{-1}, respectively, under ambient conditions. The conducting phase volume fraction (*i.e.*, volume fraction of PIL block + IL + salt) was calculated by the method described in Appendix B (B1). Polymer solutions were partially covered with aluminum foil and allowed to evaporate under ambient conditions for 12 h and then further dried under vacuum for 24 h at 50 °C. The final film thicknesses were *ca*. 35-50 μm and measured with a digital micrometer (Mitutoyo; ± 0.001 mm accuracy). The films were stored inside an argon-filled glovebox (mBraun) with both water and oxygen concentrations < 5 ppm and environmental pressure between 1-8 mbar.

Table 4.1 Sample name, chemical structure and ionic liquid composition ([a] r) of PILPTPs.

Chemical structure	Sample name	r
	PTP-Br	-
	PTP-TFSI	-
	PTP-Li-0	0
	PTP-Li-0.1 PTP-Li-0.2 PTP-Li-0.3 PTP-Li-0.5 PTP-Li-0.7	0.1 0.2 0.3 0.5 0.7

[a] r = [EMIm-TFSI] / [PVBMIm-TFSI] (mol/mol)

Table 4.2 Corresponding IL composition in PTP-TFSI and [a] PTP-Li-r SPEs.

SPE	IL weight (%)	IL volume fraction	[b] Conducting phase (PIL+Li-TFSI+IL) volume fraction
PTP-TFSI	0	0	0.742
PTP-Li-0	0	0	0.754
PTP-Li-0.1	7.62	0.068	0.770
PTP-Li-0.2	12.22	0.109	0.781
PTP-Li-0.3	16.73	0.150	0.791
PTP-Li-0.5	24.75	0.224	0.810
PTP-Li-0.7	30.67	0.280	0.823

[a] r = [EMIm-TFSI] / [PVBMIm-TFSI] (mol/mol)
[b] For all PTP-Li-r SPEs, [Li]/[PVBMIm-TFSI] (mol/mol) = 0.1. The conducting phase volume fraction was calculated by the method described in Appendix B1.

4.2.5 Characterization

The chemical structure and the degree of bromination (DB) of the brominated pentablock terpolymer, poly(S-*b*-EP-*b*-VB-Br-*b*-EP-*b*-S) (PTP-Br), was determined by proton nuclear magnetic resonance spectroscopy (^{1}H NMR; Varian 500 MHz spectrometer, 23 °C) with CD_2Cl_2 as the solvent. ^{1}H NMR spectra of the precursor polymer poly(S-*b*-EP-*b*-pmS-*b*-EP-*b*-S) and PTP-Br were collected and referenced to CD_2Cl_2 at 5.32 ppm.

Differential scanning calorimetry (DSC) experiments were performed using a differential scanning calorimeter (Q200, TA Instruments) over the temperature range of -140 to 200 °C with the heating rate of 10 °C min^{-1} under nitrogen environment using a heat/cool/heat method. DSC samples were prepared in an argon-purged glovebox (both

water and oxygen concentrations < 5 ppm). Glass transition temperatures (T_gs) were determined from the second thermogram heating cycle by the midpoint method.

Small-angle X-ray scattering (SAXS) data were collected using a Rigaku SMAX-3000 instrument. A rotating Cu anode operated at 40 kV and 30 mA was used to generate characteristic Cu X-rays with wavelength (λ) of 1.542 Å. The incident X-ray beam was collimated using a focusing optic and three pinholes in a 1.5 m evacuated flight path. Samples were characterized at a sample-to-detector distance of 1.5 m using a Gabriel-type 2D multi-wire xenon proportional counter. The data were corrected for background noise and transmission before azimuthal averaging to give intensity as a function of momentum transfer vector magnitude, I(q), where $q = 4\pi (\sin \theta)/\lambda$ and 2θ is the scattering angle. The range of q spanned was 0.007 Å^{-1} to 0.25 Å^{-1}. Data reduction and analysis were performed using Igor Pro v.7 (WaveMetrics, Inc) using procedures available from Argonne National Laboratory.[139-140] For elevated temperature measurements, samples were mounted in an environmental control cell (SAXLAB) with Kapton windows and characterized at intervals of 10 °C, ranging from 20 °C up to a maximum of 90 °C. The temperature of the cell was maintained using a temperature controlled liquid circulator (Julabo). During operation, the cell was left open to vacuum in the SAXS sample chamber. Samples were allowed to equilibrate at each temperature for 30 min prior to data collection. No evidence of sample degradation was noted.

Mechanical properties were analyzed with a dynamic mechanical analyzer (DMA; Q800, TA instruments) equipped with nitrogen-controlled humidity chamber. Rectangular

samples (20 × 5 × 0.03 mm) were tested using a tension clamp. Tensile properties were measured with a strain rate of 0.2% min^{-1} at 25 °C in nitrogen at *ca.* 0 − 3% RH.

Ionic conductivity was measured with an impedance analyzer (Solartron 1260) and potentiostat/galvanostat (Solartron 1287) in an argon-purged glovebox (both water and oxygen concentrations < 5 ppm) *via* electrochemical impedance spectroscopy. A two-electrode cell was used for ionic conductivity measurements, where SPEs were sandwiched between two stainless steel solid blocking electrodes (surface area = 1.2161 ± 0.0015 cm^2) within a sealable Teflon custom-made cell.[141] Impedance scans (Nyquist plots) were measured at 10 mV amplitude over a frequency range of 1 MHz to 1 Hz at open circuit potential at a temperature range of 30 to 93 °C controlled by heating tape (BriskHeat; XtremeFLEXSDC) and a digital temperature controller with J type thermocouple (OMEGA, Model 650). SPEs were equilibrated for at least 1.5 h at each temperature. Ionic conductivity was calculated by using the following equation: $\sigma = L/AR$, where L and A are the thickness and cross-section area of the SPE, respectively; resistance, R, was determined from the equivalent circuit regression of real-axis intercept from the Nyquist plot.[105]

The cyclability and stability with lithium metal were evaluated using a battery tester (MACCOR, 4200M) *via* lithium stripping and plating. The test cell was assembled by sandwiching the lithium ion conducting PILPTP film between two lithium ribbons (12 mm dia.) using similar assembly process as described in CR2032 coin cell (Section 2.6). Symmetrical lithium metal/SPE/lithium metal cells were examined under constant current (0.02 mA cm^{-2}, reversed polarization every 1h) at room temperature. The interfacial

resistance evolution was collected *via* electrochemical impedance spectroscopy with an impedance analyzer every 10th polarization cycle at 10 mV amplitude at a frequency range of 100 kHz to 1 Hz. The obtained spectra were then fitted using an equivalent circuit model described in our previous publication.[104]

The diffusion-time dependent diffusion coefficients ($D_{app}(\Delta)$) of 1-ethyl-3-methylimidazolium cation (D_{EMIm+}) and lithium cation (D_{Li+}) were determined by using ^{1}H and ^{7}Li pulsed-field-gradient nuclear magnetic resonance (PFG-NMR). The PFG-echo profiles were obtained using the 13-interval bipolar gradient stimulated echo (Dbppste, vender supplied sequence, VNMRJ, Agilent, USA) as a function of gradient strength (g) and fitted with the Stejskal-Tanner equation[181]:

$$S(g) = S(0)\exp\left[-D(g\gamma\delta^2)\left(\Delta - \frac{\delta}{3}\right)\right]$$ (4.1)

where S(g) and S(0) are the echo intensity at the gradient strength of *g* and 0, respectively; *D* is the diffusion coefficient; γ is the gyromagnetic ratio of ^{1}H or ^{7}Li; Δ is the diffusion delay; δ is the length of gradient pulse. The gradient strength was varied with 32 equal steps and the maximum gradient strengths were chosen accordingly for the full decay of echo signal. The Δ and δ are $20 - 160$ ms and $3 - 4$ ms, respectively. The TFSI anion diffusion coefficient, D_{TFSI-} was not able to be determined using ^{19}F PFG-NMR because the fast relaxation of ^{19}F nuclei made invisible the signal after applying PFG sequence. Then, the rotational correlation time, τ_c, was used to determine D_{TFSI-} with the Einstein-Smoluchowski equation[182]:

$$D = \frac{a^2}{6\tau_c}$$ (4.2)

where a is the molecular radius of TFSI⁻ anion (3.53 Å).[183] The rotational correlation times

(τ_c) for TFSI⁻ anion were estimated using the nuclear relaxation ratio[184]:

$$\frac{T_2}{T_1} = \left[\frac{2}{1+\omega_0^2\tau_c^2} + \frac{8}{1+4\omega_0^2\tau_c^2}\right] / \left[3 + \frac{5}{1+\omega_0^2\tau_c^2} + \frac{2}{1+4\omega_0^2\tau_c^2}\right] \tag{4.3}$$

All NMR experiments were performed on a 600 MHz NMR spectrometer equipped with

a 5 mm z-gradient liquid NMR probe (Doty Scientific, USA). ^{19}F spin-spin (T_2) and spin-

lattice (T_1) relaxation times were measured using a spin-echo (90°-τ-180°-τ-acquisition)

and the inversion-recovery (180°-τ-90°-acquisition) sequences, respectively, at 25 °C.

Larmor frequency (ω_0) for ^{19}F relaxation measurements was $2\pi \times 564.01$ rad MHz.

4.2.6 Preparation of Lithium Ion Batteries with Lithium Ion Conducting PILPTP Films as Solid-State Electrolyte and Separator

The negative electrode (anode) was prepared by spreading a mixture of (8.0/1.0/1.5 wt.

ratio) Li$_4$Ti$_5$O$_{12}$/conductive graphite/PVDF dissolved in *N*-methyl-2-pyrrolidone (NMP,

22 wt. %) onto a copper current collector using an adjustable film applicator (MTI

Corporation). The positive electrode (cathode) was prepared using a similar process as the

anode by spreading a mixture of (7.0/2.0/1.0 wt. ratio) LiCoO$_2$/conductive graphite/PVDF

dissolved in NMP (27 wt. %) onto conductive carbon-coated aluminum foil. The film

thicknesses ranged from 0.03 to 0.04 mm and were measured with a digital micrometer

(Mitutoyo; ± 0.001 mm accuracy). The electrodes were first dried overnight at room

temperature, followed by additional drying at 120 °C under vacuum for 4 h. The active

material loadings were approximately 2.17 mg cm^{-2} and 1.41 mg cm^{-2} for Li$_4$Ti$_5$O$_{12}$ and

LiCoO$_2$ electrodes, respectively. Disks 1.2 cm in diameter were punched from the Li$_4$Ti$_5$O$_{12}$ and LiCoO$_2$ electrodes without any additional preparation or pressing before use. Li$_4$Ti$_5$O$_{12}$/LiCoO$_2$ polymer batteries were fabricated in an argon-purged glove box (water and oxygen concentrations < 5 ppm) by laminating the LiCoO$_2$ positive electrode with lithium ion conducting PILPTP film (PTP-Li-0.5) and then adding the Li$_4$Ti$_5$O$_{12}$ negative electrode as shown in Figure 4.2. Additional drops of 1.0 M Li-TFSI/EMIm-TFSI (*ca.* 80 mg) were added to each electrode during assembly to improve the contact between electrodes and PTP-Li-0.5.[86] Coin cell batteries were pressed twice using an electric coin cell crimping machine (MTI Corporation, MSK-160D) under argon environment at room temperature to ensure a proper seal.

After assembling, the batteries were transferred to a battery tester (MACCOR, 4200M) and held at open circuit voltage (OCV) for 24 h prior to testing. Battery cycling tests on Li$_4$Ti$_5$O$_{12}$/ LiCoO$_2$ coin cell polymer batteries were performed at room temperature at a rate of C/n, where C is the theoretical capacity of cathode material (mAh g^{-1}) and n is the number of hours used to charge and discharge the battery. Batteries were charged at C/10 rate (calculated from the mass of LiCoO$_2$ electrode) using a constant current until the potential reached 2.7 V and followed by a constant voltage step at 2.7 V for 3 h. Later a discharge step at C/10 using constant current was applied until the potential reached 1.5 V. After a 40 min rest period, the same charge-discharge procedure was repeated as described above.
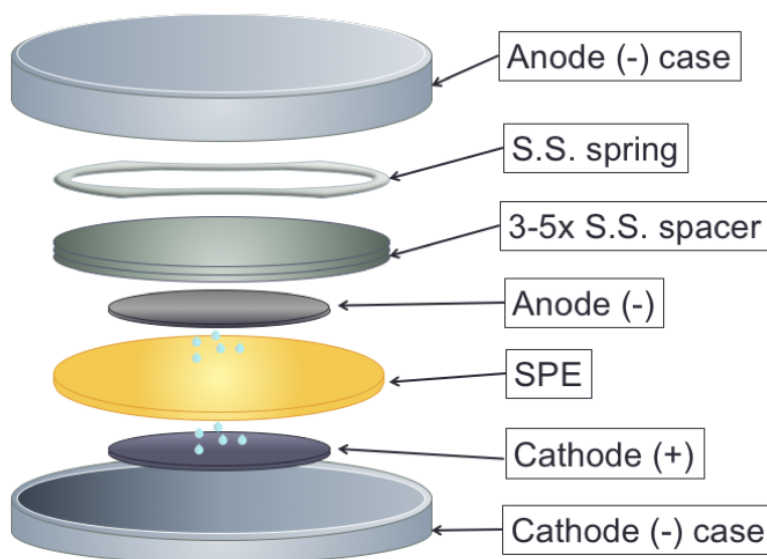
Figure 4.2 Schematic showing configuration of lithium-ion coin cell battery with lithium ion conducting PILPTP as solid-state electrolyte and separator.

4.3 Results and Discussion

Figure 4.3 shows the DSC thermograms (glass transition temperatures) for PTP-TFSI and the PTP-Li-r SPEs. PTP-TFSI exhibits two T_gs (indicative of phase separation), where the higher T_g is at 122 °C and this corresponds to the A block (styrene), while the lower T_g at 69°C corresponds to the middle C block (PIL). The T_gs of B block (ethylene-*r*-propylene), which are located *ca.* -50 °C in our previous study,[104] are absent in the thermogram due to its relatively smaller M_n compared to the A and C blocks (2 kg mol^{-1} *versus* 20 kg mol^{-1} and 44 kg mol^{-1}, respectively). As IL content increases in the PTP-Li-r SPEs, the depression of the middle C block T_gs from 46 °C to -44 °C can be observed, while the polystyrene T_gs are unaffected (*ca.* 120 °C), suggesting that the IL/salt mainly resides in the conductive C block domains (PIL). This could be due to the high chemical

affinity of ILs towards the PIL block compared to the other blocks producing SPEs with phase-separated conductive and non-conductive microdomains.[107, 185-188] The phase selectivities of IL and T_g depression from PTP-TFSI polymer to PTP-Li-r SPEs corroborate with other reports on block copolymers with addition of IL/salt,[35, 107, 187] where the IL and salt are selective for one block and act as plasticizers, increasing polymer chain dynamics. These properties suggest an increase in segmental mobility of the PIL (conductive) block, therefore allowing for an enhancement of the lithium ion mobility (conductivity). The evidence of two distinct T_gs for the PTP-Li-r SPEs suggests an ordered microphase separation in the PILPTP SPEs and can be confirmed with SAXS (Figure 4.4a).
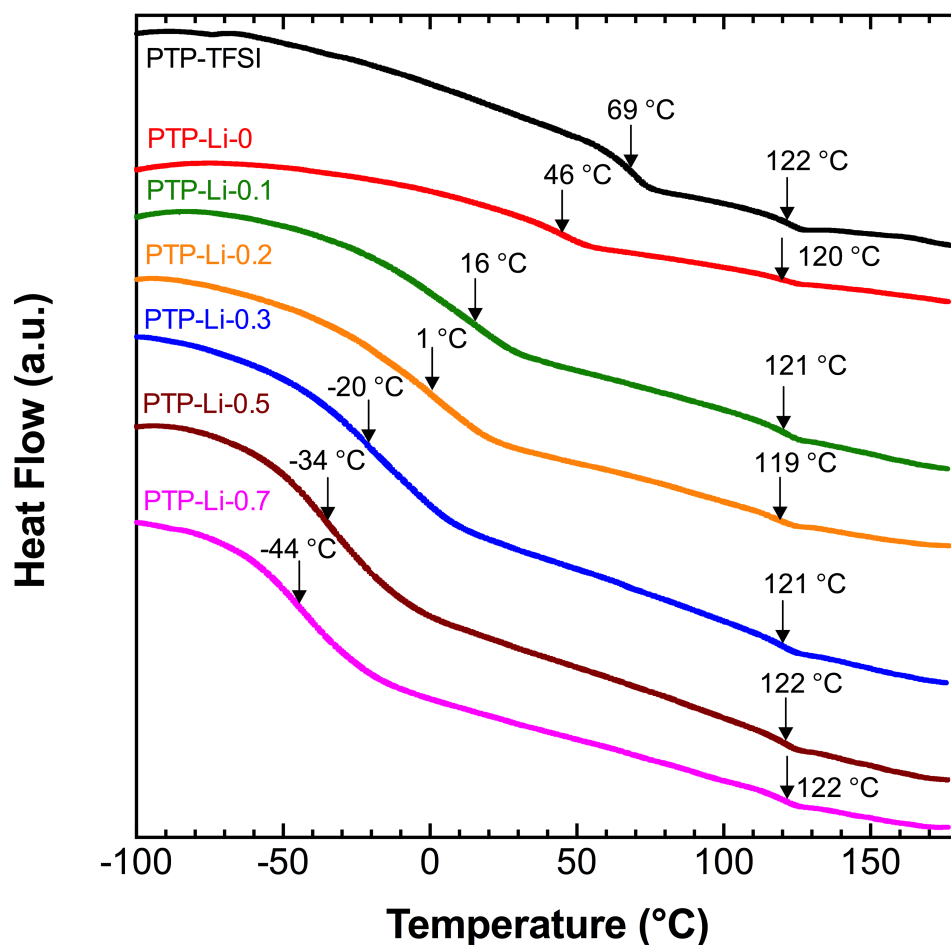
Figure 4.3 Differential scanning calorimetry profiles for all PILPTP SPEs: PTP-Li-r ([Li]/[PVBMIm-TFSI] = 0.1) at different r = [EMIm-TFSI]/[PVBMIm-TFSI] ratios.

Figure 4.4a shows the SAXS data for PTP-TFSI and the PTP-Li-r SPEs. The SAXS profile for PTP-TFSI shows a strong peak and two additional, distinct scattering features at higher angles, indicating microphase separation and possible ordering. The SAXS profiles of PTP-Li-r at r = 0 to 0.7 are nearly identical to that of PTP-TFSI, indicating that the morphology of PTP-TFSI is retained despite the addition of the IL/salt. The average interdomain spacing, d^*, can be directly calculated from the position of the primary

102

scattering maximum, q^*, where $d^* = 2\pi/q^*$ [189] (listed in Table 4.3). A careful analysis of the SAXS data strongly suggests a morphology of polystyrene (PS)-poly(ethylene-*r*-propylene) (PEP) core-shell spheres on a poorly ordered body-centered cubic (BCC) lattice with PIL block as the continuous domain.[190] The detailed descriptions of morphology analysis and modeling process are included in Appendix B2.

The SAXS profiles of PTP-Li-0.5 SPE under vacuum at elevated temperatures (20 to 90 °C) are shown in Figure 4.4b. The SAXS profiles of PTP-Li-0.5 remain virtually unchanged at elevated temperatures, with almost no change in the values of d^* (Table 4.3), indicating the persistence of the morphology observed at room temperature. The same behavior was observed for PTP-TFSI and PTP-Li-r at other IL compositions (Table 4.3). The SAXS data also shows that the SPEs do not exhibit an order-disorder transition (ODT) between 20 to 90 °C, which is the operating temperature window of lithium ion batteries.

In diblock copolymers, the effects of swelling with either a homopolymer or a selective solvent are complex and well-known to alter morphological behavior.[191-194] For ABA triblock copolymers, directly analogous to the ABCBA pentablock copolymers in this study, swelling the midblock with a selective solvent has been found to have a similar effect on morphology, resulting in either swelling or a morphological transformation.[195] In the present study, as IL content increases, the overall morphology is unchanged but rather than increasing with IL content, d^* is found to decrease from 37.8 to 29.6 nm. However, as d^* decreases, analysis of the SAXS data show that the mean radius of the PS-PEP core-shell domains decreases from 16.5 nm to 10.0 nm (Appendix B in Table B1). The decrease of radius allows the BCC lattice to contract while still maintaining the

103

required ratio of conducting phase and non-conducting phase, leading to the observed decrease in d^* and BCC lattice constant ($a = d^*\sqrt{2}$) (Appendix B in Table B1). This change in the equilibrium morphology may be attributed to the thermodynamic balance between chain stretching and unfavorable enthalpic interactions between constituents. If the sphere radius remained constant, the addition of ILs would require the polymer chain of PIL block to elongate and stretch, which is energetically unfavorable.[196-197] Here, the material accommodates this change by reorganizing to form smaller PS-PEP sphere domains, while maintaining the BCC structure. This further implies that the enthalpic penalty for increasing the interfacial area between the core-shell spheres and continuous conducting matrix is lower than the entropic cost of increased chain stretching. Further analysis of the thermodynamic behavior is required to confirm this behavior.
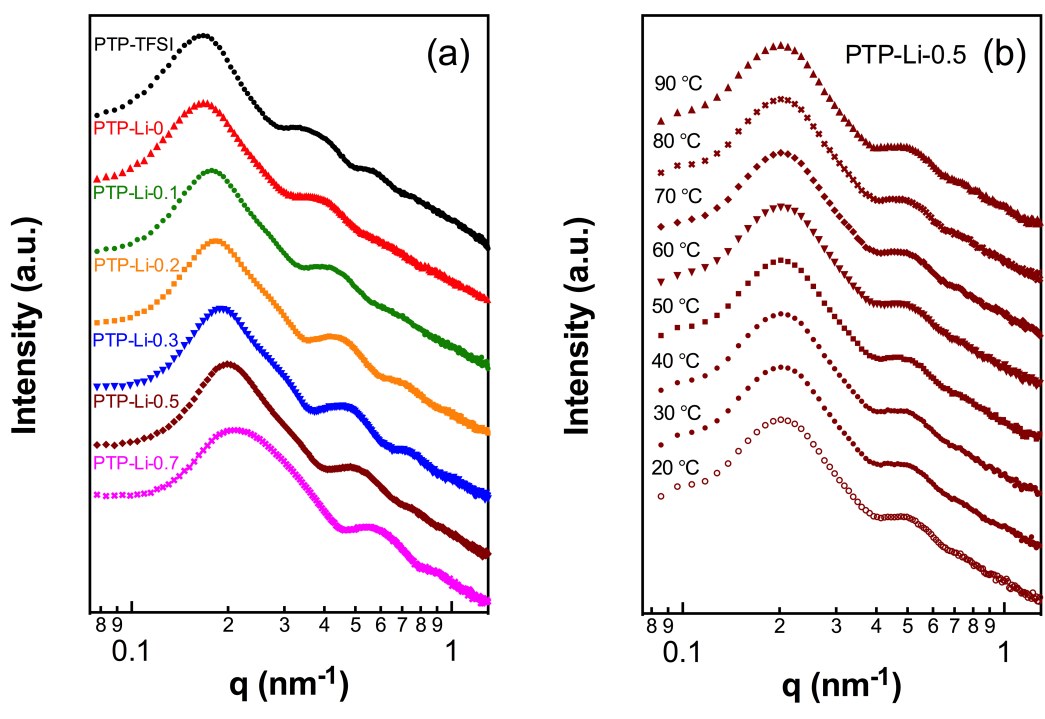
Figure 4.4 Small-angle X-ray scattering (SAXS) profiles of PTP-TFSI and PTP-Li-r SPEs at (a) room temperature and (b) elevated temperatures from 20 to 90 ℃ under vacuum for PTP-Li-0.5.

Table 4.3 SAXS domain spacing, d*, of PTP-TFSI and PTP-Li-r SPEs.

Temperature (°C)	d* (nm)			
	PTP-TFSI	PTP-Li-0	PTP-Li-0.1	PTP-Li-0.2
Room	37.75	37.31	35.13	34.06
20	37.51	37.07	34.28	33.61
30	37.59	37.11	34.34	33.66
40	37.63	37.17	34.38	33.70
50	37.63	37.15	34.29	33.69
60	37.64	37.15	34.03	33.56
70	37.61	37.03	33.74	33.35
80	37.45	36.87	33.34	32.70
90	36.91	36.41	32.90	32.58

Temperature (°C)	d* (nm)		
	PTP-Li-0.3	PTP-Li-0.5	PTP-Li-0.7
Room	32.79	31.22	29.60
20	32.70	31.22	28.87
30	32.76	30.70	28.92
40	32.72	30.71	28.96
50	32.66	30.72	29.02
60	32.58	30.74	29.04
70	32.46	30.71	29.22
80	32.40	30.74	29.54
90	32.36	30.83	30.25

Figure 4.5 shows the temperature-dependent (30 to 93 °C) ionic conductivity under a dry condition (in an argon-filled glove box) for PTP-Li-r SPEs. The conductivities were regressed to Vogel-Fulcher-Tammann (VFT) equation (Figure 4.5a) and Arrhenius equation (Figure 4.5b). In Figure 4.5, the conductivities increase with increasing r from values on the order of 10^{-8} S cm^{-1} (PTP-Li-0.1) to values higher than 10^{-5} S cm^{-1} (PTP-Li-0.7) at 30 °C. This result can be attributed to the reduction of PIL block T_g (or increase in the segmental motion of the polymer chains) and the increasing number of mobile ions with increase in IL. The PTP-Li-0.7, with the highest IL composition, has the highest

conductivity of 0.72 mS cm^{-1} at 93 ºC. This result is also comparable to our previous study (SPE with σ = 1.1 mS cm^{-1} at 94 ºC) [104], which has tert-butyl-styrene as the A block and higher molecular weight ethylene-*r*-propylene B block (13-14 kg mol^{-1}) compared with to this present study, which has styrene as the A block and a lower molecular weight ethylene-*r*-propylene B block (2 kg mol^{-1}).

In Figure 4.5a, the conductivity data was regressed to the VFT equation[116-117]:

$$\sigma(T) = \sigma_0 \exp\left(-\frac{b}{T-T_0}\right) \qquad (4.4)$$

where σ_0 (S cm^{-1}) is infinite temperature conductivity, which is proportional to the free ion concentration[156-157], b (K) is a constant related to the pseudo-activation energy required for segmental motion of the polymer chain[198], and T_0 (K) is the Vogel temperature, which corresponds to a temperature at which ion motion first occurs and is typically ~ 50 K below the measured T_g of the polymer.[199] In Figure 4.5b, the conductivity data was regressed to the Arrhenius equation:

$$\sigma(T) = \sigma_0 \exp\left(-\frac{E_a}{RT}\right) \qquad (4.5)$$

where E_a is the activation energy related to the potential barrier of the displacement of the charge carrier.[200] The resulting VFT and Arrhenius fitting parameters are listed in Table 4.4. For PTP-Li-0.1, PTP-Li-0.2, and PTP-Li-0.3 the VFT model reveals a more successful regression (R-squared value = 0.99) than the Arrhenius model (R-squared value = 0.97), indicating that at lower ionic liquid content (r $\leq$ 0.3), ionic mobility is more strongly coupled to the segmental motion of the polymer chains.[201] For PTP-Li-0.5 and PTP-Li-0.7, the conductivity data appears to fit both VFT and Arrhenius equations reasonably (R-squared value = 0.99) over the temperature range. These results indicate

that at higher IL content, the SPEs start to exhibit Arrhenius behavior, where ion motion is dictated by ion hopping and less dependent on polymer segmental dynamics.[202-203] The reduction of temperature dependence of conductivity between PTP-Li-0.1 and PTP-Li-0.7 can be observed; the PTP-Li-0.1 SPE increases three orders of magnitude, while the PTP-Li-0.7 SPE increases only one order of magnitude as a function of temperature. Table 4.4 lists the Arrhenius activation energies (E_a) and Vogel temperatures (T_0) determined from the Arrhenius and VFT regressions, respectively. The Arrhenius activation energy decreases from 45.22 kJ mol^{-1} to 18.42 kJ mol^{-1} for SPEs PTP-Li-0.1 to PTP-Li-0.7, respectively. This trend indicates the beneficial incorporation of IL into the PIL block, enhancing the free volume of the system and facilitating the motion of ionic charge carriers.[200] The VFT regression results in T_g-T_0 values close to the expected 50 K for PTP-Li-0.1, PTP-Li-0.2, and PTP-Li-0.3, whereas the T_g-T_0 values of PTP-Li-0.5 and PTP-Li-0.7 are larger (*ca.* 90 K).[66]
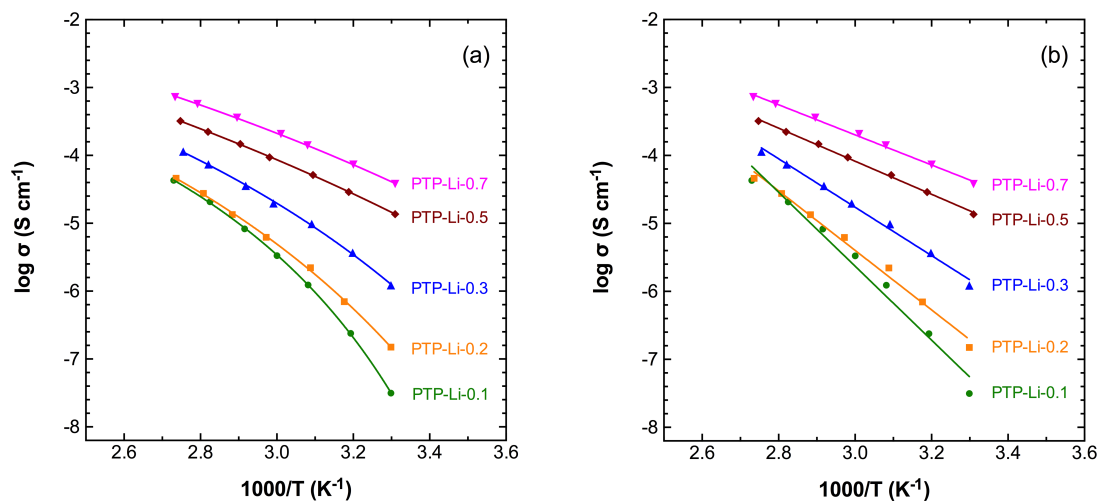
Figure 4.5 Temperature-dependent dry (H_2O < 5 ppm) ionic conductivity of the PTP-Li-r SPEs at different r = [EMIm-TFSI]/[PVBMIm-TFSI] ratios. Data regressed to (a) Vogel-Fulcher-Tammann (VFT) (solid lines) and (b) Arrhenius (solid lines) equations.

Table 4.4 Regression results for PTP-Li-r SPEs.

SPE	[a] E_a (kJ mol^{-1})	[b] T_0 (K)	[c] T_g (K)	$T_g - T_0$ (K)
PTP-Li-0.1	45.22	240.9	289.15	54.1
PTP-Li-0.2	36.41	210.6	274.15	63.4
PTP-Li-0.3	29.61	195.9	253.15	57.1
PTP-Li-0.5	20.22	140.3	239.15	98.7
PTP-Li-0.7	18.42	147.1	229.15	81.9

[a] Activation energies from Arrhenius equation.
[b] Vogel temperatures from VFT equation.
[c] PIL middle block T_g measured from DSC.

Figure 4.6 shows the conductivity *versus* reduced temperature, T_g/T (based on T_g of PIL). Plotting conductivity *versus* reduced temperature is a method to view the conductivity without the contribution of polymer chain segmental motion,[204-205] *i.e.*, T_g-

109

independent conductivity. Therefore, the attribution of charge carrier concentration on ion conductivity can be more clearly revealed. The T_g-independent conductivities display a similar trend, which is common with materials with similar chemistries.[58] If the reduced temperature approach removes the contributions of polymer chain segmental dynamics on conductivity, then the differences in conductivity can be primarily attributed to the differences in ionic carrier concentration. In other words, if there were no differences in ion carrier concentration, then the conductivity for all SPEs in Figure 4.6 would collapse perfectly onto one master curve. The differences observed in Figure 4.6 therefore support the results in Figure 4.5 suggesting that at various ionic liquid compositions, there are contributions from both polymer chain segmental dynamics and ion carrier concentration.
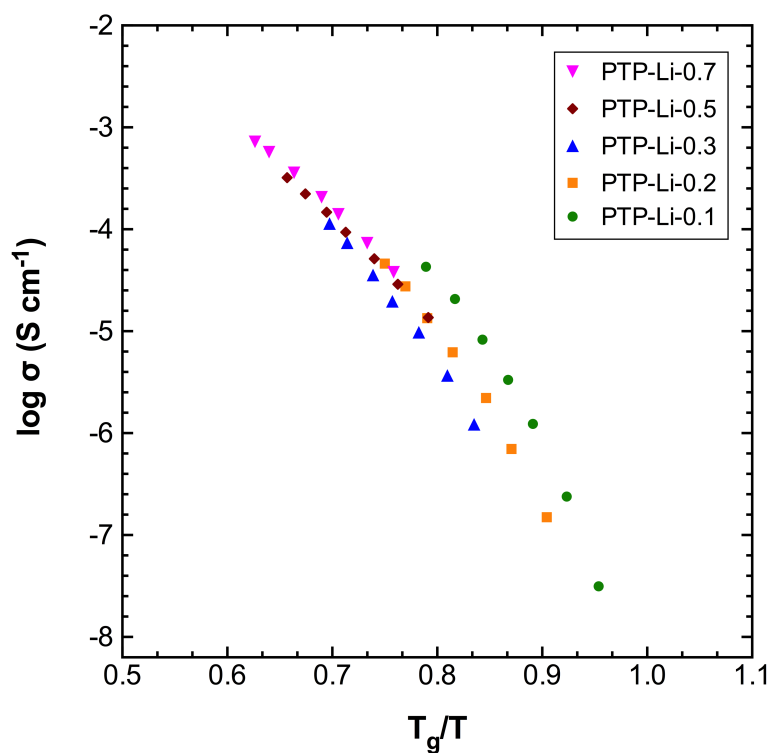
Figure 4.6 Ionic conductivity *versus* T_g/T of PTP-Li-r SPEs.

Mechanical strength of PTP-Li-r SPEs were measured with DMA; strain-stress profiles are shown in Figure 4.7a. Elastic modulus, ultimate tensile strength, and elongation break results from the strain-stress profiles are listed in Table 5. The PTP-Li-0.1 SPE reveals the highest elastic modulus (59.89 MPa) and ultimate tensile strength (1.94 MPa) compared to other samples. The depression of mechanical properties can be observed with the addition IL; elastic modulus and ultimate tensile strength decrease from 59.89 MPa and 1.94 MPa to 0.41 MPa and 0.20 MPa, respectively, with increasing r from 0.1 to 0.7. In Figure 4.7b, an intense drop in the elastic modulus at r = 0.3 can be observed (from 52.17 to 0.55 MPa, at r = 0.2 to 0.3), indicating the mechanical percolation behavior between IL

composition and elastic modulus. This mechanical percolation transition was also observed in other binary polymer blends.[206-209] At low IL composition (r < 0.3), the glassy polystyrene domain appears to have a significant effect on the modulus. Between r = 0.2 and 0.3, the SPE goes through a percolation transition and the PIL/IL/salt phase begins to impact the modulus. Specifically, the addition of IL results in a plasticizing effect on the SPE and leads to the depression of mechanical properties. Results in Figure 4.7 also suggest that in ternary blend SPEs, the mechanical properties can be optimized with the appropriate component composition (*i.e.* block copolymer/salt/IL composition ratio).
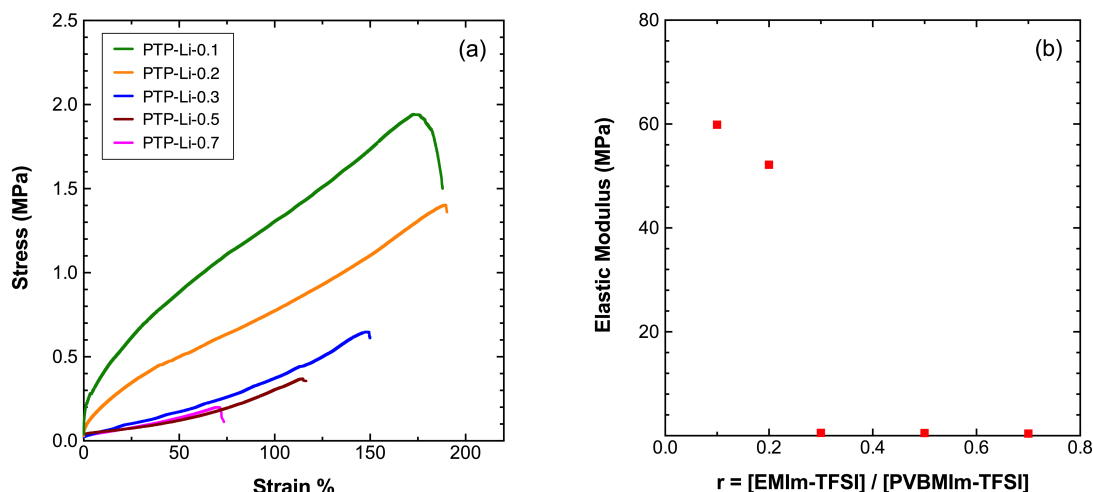
Figure 4.7 (a) Strain-stress profiles of PTP-Li-r SPEs at different r = [EMIm-TFSI]/[PVBMIm-TFSI] ratios at 25 ºC and 5% RH; (b) elastic modulus as a function of r.

Table 4.5 Mechanical properties of PTP-Li-r SPEs.

SPE	Elastic modulus (MPa)	Ultimate tensile strength (MPa)	Elongation to break (%)
PTP-Li-0.1	59.89	1.94	182.4
PTP-Li-0.2	52.17	1.40	190.1
PTP-Li-0.3	0.55	0.65	150.0
PTP-Li-0.5	0.51	0.37	116.5
PTP-Li-0.7	0.41	0.20	73.4

Figure 4.8 shows selected Li-metal stripping and plating overvoltage profiles for PTP-Li-0.2 (Figure 4.8a) and PTP-Li-0.5 (Figure 4.8b); measurements are at a current density of 0.02 mA cm^{-2} at room temperature using a battery tester (MACCOR, 4200M). Both SPEs exhibit smooth polarization profiles over 500 cycles, indicating a smooth interphase formation on the lithium metal.[210] Over the 500 cycles, the PTP-Li-0.2 remains in a relatively constant cell overvoltage window of *ca.* 50 mV, while PTP-Li-0.5 shows more pronounced voltage oscillations from *ca.* 90 to 150 mV after 300 cycles. These results indicate a greater stability of PTP-Li-0.2 and its outstanding ability to suppress polarization degradation. The higher polarization (or concentration polarization) usually results from the accumulation of anions at the electrode surface and causes concentration gradients.[211-212] These smooth overvoltage profiles also indicate that no lithium dendrite formation occurs and good compatibility between SPEs and lithium metal electrodes.[124]

The impedance response from the stripping and plating cycles was regressed to an equivalent circuit model to determine all resistances across the entire cell.[104] The

electrolyte bulk resistance (R_b) and interfacial resistance (R_i) were evaluated as a function of selected cycles in Figures 4.8c and 4.8d. The overall interfacial resistance (R_i) is composed of the passive layer resistance (R_p) from the solid electrolyte interface (SEI) and the charge transfer resistance (R_{ct}) between electrode and electrolyte; *e.g.*, $R_i = R_{ct} + R_p$. The R_b of PTP-Li-0.2 remains stable (*ca.* 22 Ω) during the entire 500 cycles, while the R_b of PTP-Li-0.5 increases 3-fold during the same cycle span (*ca.* 100 to 300 Ω). Additionally, in Figure 4.8d, PTP-Li-0.2 shows a relatively higher R_i then that of in PTP-Li-0.5 (*i.e.*, 700 vs 400 Ω) in the initial cycles; however, it gradually decreases during cycling and results in a similar R_i (*ca.* 500 Ω) for both SPEs after 500 cycles. The R_i for the PTP-Li-0.5 only exhibits minimal change from 480 to 500 Ω. The decrease of R_i in PTP-Li-0.2 and its unchanging overvoltage profile indicate a stable and conductive SEI was formed. The low and stable polarization can be explained by an increase in the surface area of active lithium at the electrode during lithium stripping and plating, which has also been observed in IL based electrolytes.[125-127] Comparing Figure 4.8a and 4.8b with 4.8c, the cell overvoltage profiles can be correlated with R_b of the SPEs; typically, stable R_b correlates to stable polarization profiles and *vice versa*. Overall, both SPEs show stable R_i after 500 cycles, indicating good interfacial contact between the lithium electrode and the SPE, as well as enhanced SEI layer stability. The incorporation of IL in this study could facilitate the uniform formation of SEI and result in the stable polarization. However, the higher IL content in the SPE might cause the trade-off between electrolyte stability and its higher bulk electrolyte resistance (300 Ω for PTP-Li-0.5) and may merit further investigation.

114
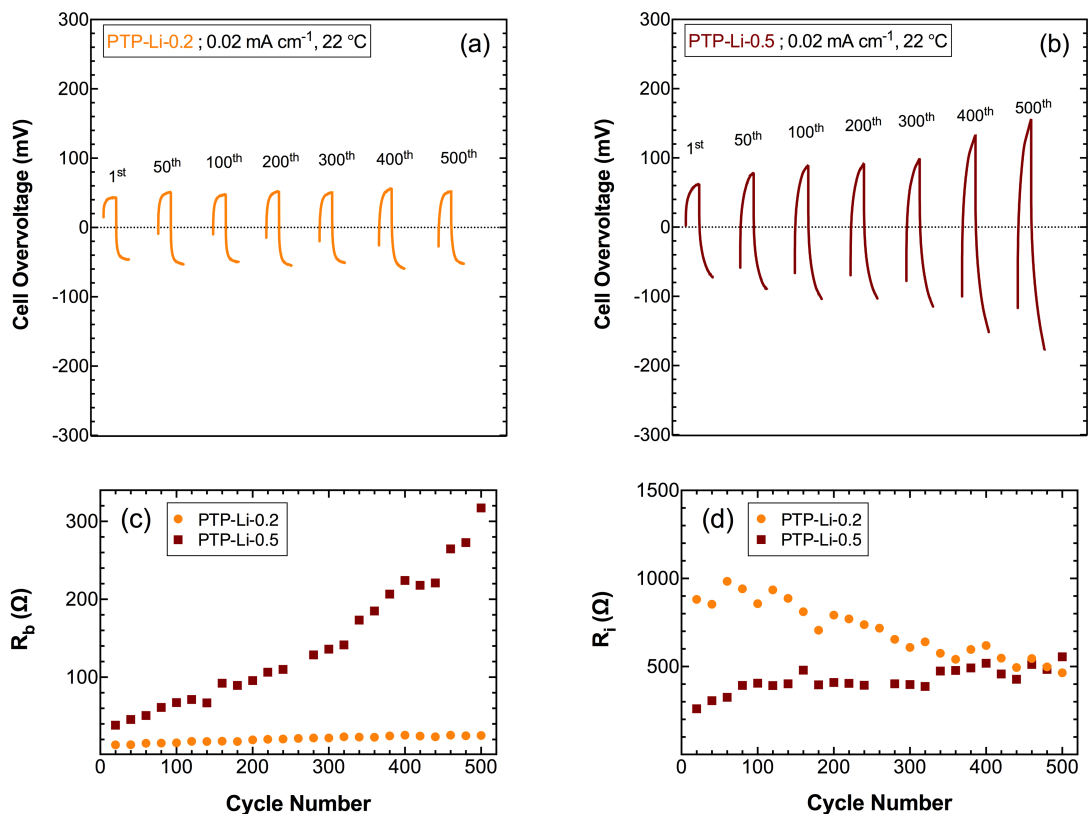
Figure 4.8 Selected Li-metal stripping-plating cycles with symmetric Li / SPE / Li cell under 0.02 mA cm^{-2} at room temperature of (a) PTP-Li-0.2 and (b) PTP-Li-0.5. (c) Electrolyte bulk resistance and (d) interfacial resistance at selected cycles from equivalent circuit model regression of impedance spectra.

Figure 4.9 shows the comparison of self-diffusion of mobile cations and anions (D_{Li+}, D_{EMIm+}, and D_{TFSI-} at diffusion delay $\Delta = 0$ for PTP-Li-0.2, PTP-Li-0.5 and PTP-Li-0.7 SPEs). The detailed description of diffusion coefficient calculation is detailed in the Supporting Information (SI.3.). The diffusion trends for all ions are similar in both PTP-Li-0.5 and PTP-Li-0.7. PTP-Li-0.2 shows the faster Li$^+$ diffusion (*i.e.*, 9.3×10^{-12} m^2 s^{-1} for PTP-Li-0.2 *versus* 3.8×10^{-12} m^2 s^{-1} and 4.2×10^{-12} m^2 s^{-1} for PTP-Li-0.5 and PTP-Li-0.7, respectively) and EMIm$^+$ diffusion (*i.e.*, 3.0×10^{-12} m^2 s^{-1} for PTP-Li-0.2 *versus* 1.5

115

$\times$ 10^{-12} m^2 s^{-1} *and* 1.6 $\times$ 10^{-12} m^2 s^{-1} for PTP-Li-0.5 and PTP-Li-0.7, respectively) and slightly slower TFSI$^-$ diffusion (*i.e.*, 1.0 $\times$ 10^{-12} m^2 s^{-1} for PTP-Li-0.2 *versus* 2.3 $\times$ 10^{-12} m^2 s^{-1} *and* 1.7 $\times$ 10^{-12} m^2 s^{-1} for PTP-Li-0.5 and PTP-Li-0.7, respectively) compared with the previous two SPEs. In PTP-Li-0.2, the difference between D_{Li+} and D_{TFSI-} is about an order of magnitude (*i.e.*, 9.3 $\times$ 10^{-12} m^2 s^{-1} *versus* 1.0 $\times$ 10^{-12} m^2 s^{-1}). This enhancement and suppression of Li$^+$ and TFSI$^-$ mobilities, respectively, in PTP-Li-0.2 compared to the other two PTP-Li-r SPEs may be a result of the segmental motion of the PIL polymer chain, where Li$^+$ and EMIm$^+$ are more mobile due to their smaller sizes comparing with TFSI$^-$ (*i.e.*, V_{Li+} ~ 25 Å^3 and V_{EMIm+} ~154 Å^3 *versus* V_{TFSI-} ~ 248 Å^3 from ref[103, 115]) while TFSI$^-$ ions were hold on the vicinity of PIL domains. However, when IL concentration increases, this effect is dampened due to the increase in EMIm$^+$ and TFSI$^-$ ions in the PIL domain and the diffusion of constituent ions will be vary according to the interactions between ions and its environment (*i.e.* ternary blend SPE[213]). All the SPEs in this work show D_{Li+} > D_{TFSI-}, suggesting a higher degree of Li−TFSI dissociation occurs in this polymer system, which is different from the bulk ionic liquids/Li-TFSI system, where D_{Li+} < D_{TFSI-} due to the formation of ion clusters (*i.e.*, [Li(TFSI)$_{m+1}$]$^{m-}$, with m+1 $\leq$ 4, from ref [119-122]).

The diffusion coefficient results in Figure 4.9 can also be correlated with the cell overvoltage profiles in Figures 4.8a and 4.8b, where higher D_{Li+} in PTP-Li-0.2 can effectively prevent the formation of a concentration gradient, as well as the accumulation of overvoltage (*i.e.*, maintains stable overvoltage at *ca.* 50 mV), while the PTP-Li-0.5

reveals an increasing of overvoltage from 90 mV to 150 mV due to its lower D_{Li+}, indicating the formation of a concentration gradient.
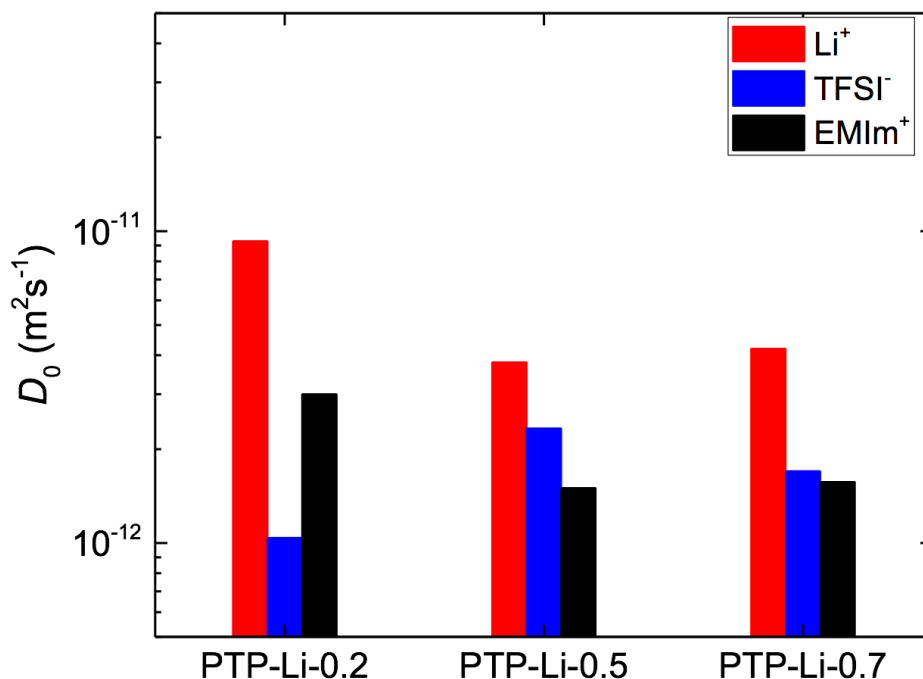
Figure 4.9 PFG-NMR self-diffusion coefficients for Li$^+$, TFSI$^-$, and EMIm$^+$ in PTP-Li-0.2 , PTP-Li-0.5, and PTP-Li-0.7.

Figure 4.10 shows the charge-discharge (C/D) performance of Li$_4$Ti$_5$O$_{12}$/ PTP-Li-0.5/LiCoO$_2$ 2032 coin cell at room temperature. Lithium titanate (Li$_4$Ti$_5$O$_{12}$, theoretical capacity = 161 mAh g^{-1}) was used as the negative electrode (anode) due to its enhanced cycling stability with minimal volume change and minimum SEI formation during cycling compared with graphite.[214-215] Lithium cobalt oxide (LiCoO$_2$, theoretical capacity = 145 mAh g^{-1}) was used as the positive electrode (cathode) owing to their common usage in

small portable electronics and good stability.[8] In Figure 4.10, the C/D cycles are at a current rate of 0.1 C and voltage window from $1.5 - 2.7$ V versus open circuit at 22 ℃. The discharge capacity of the battery is 57 mAh g^{-1} in the first cycle; during the first twenty cycles, the discharge capacity gradually fades to *ca.* 40 mAh g^{-1}, which is *ca.* 30% of the theoretical capacity of LiCoO$_2$ (145 mAh g^{-1}) at 0.1 C. The cell shows stable cycling performance and final capacity retention of 63 % over 100 cycles. These results are comparable to other reported LTO/LCO battery performances with SPE separators,[86, 216-217] where others require testing at elevated temperatures and only report less than 50 stable cycles.

The PTP-Li-0.5 SPE reveals promising room temperature cycling durability in the lithium ion battery over 100 cycles with discharge capacity *ca.* 40 mAh g^{-1}. The relatively low discharge capacity may due to the moderate ionic conductivity (*ca.* 10^{-5} S cm^{-1} at room temperature), which could be improve by altering the PIL, IL and salt compositions. By understanding the underlying chemistries and components involved in the battery cycling degradation, guidelines for designing long-lasting lithium-ion battery may be formulated.
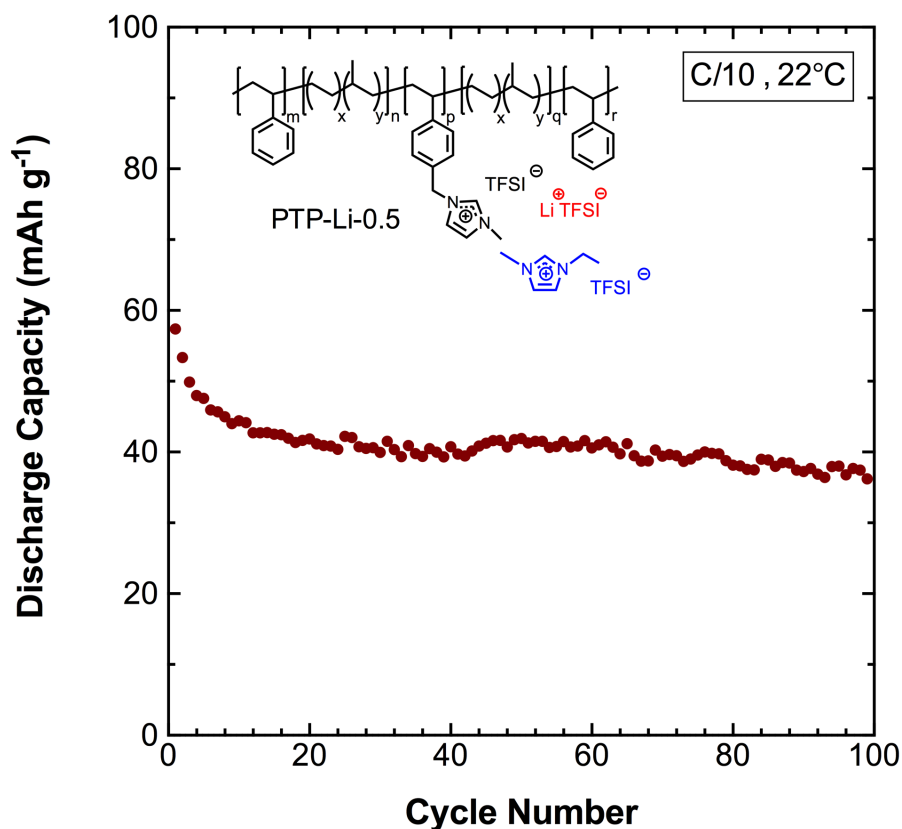
Figure 4.10 Discharge capacity as function of cycle number with PTP-Li-0.5 as solid-state electrolyte and separator in the $Li_4Ti_5O_{12}/$ $LiCoO_2$ cell at 22 °C. Charge-discharge rate = 0.1 C from 1.5 to 2.7 V.

4.4 Conclusions

Ternary blend PIL multiblock polymer SPEs (*i.e.,* PIL multiblock polymer + ionic liquid + lithium salt) provide a promising pathway to achieve high ionic conductivity with numerous property-tuning parameters. In this study, a ternary blend SPE with varying IL compositions was systematically investigated with respect to ion transport, morphology, and mechanical properties along with electrochemical stability. Results show that at high IL concentrations, the IL resides in the PIL conductive domain and depresses the PIL

block T_g, as well as increases the continuous conductive domain for ion transport. Increasing the IL concentrations also contributes to plasticization and mechanical percolation. Interestingly, SPE with high IL concentrations results in a reduction of Li^+ cation self-diffusion coefficient and increased overpotential. This suggests that ion solvation phenomena and transport mechanisms in the SPE are fundamentally important to electrolyte performance. This work provides valuable insights in regard to IL incorporation in solid-state PIL block polymers enabling the design of new SPEs with both high ionic conductivity and improved stability.

CHAPTER V

CONCLUSIONS AND FUTURE OUTLOOK

5.1 Summary

The development of SPEs for the solid-state lithium ion batteries requires a comprehensive understanding of the structure-property relationships in polymers. In this work, SPE based on novel PIL block copolymers were investigated in regards to transport properties, self-assembled morphology, electrochemical stability, and battery performance. Key chemistry-property findings elucidated the ability to optimize the properties of SPE with attainable high ionic conductivity and improved stability for the future solid-state lithium ion batteries.

A series of styrene-based PIL diblock copolymers and their analogous PIL homopolymers were synthesized with various covalently attached cations (MIm^+ and $MPyr^+$) and counter-anions ($TFSI^-$ and FSI^-). This study allowed for the investigation of the impacts of lithium salt concentration and cation/anion chemistry in a binary salt-doped PIL diblock copolymer SPE in relation to physical, transport, morphological, and electrochemical properties. PIL diblock copolymer SPEs with FSI^- exhibit ion-hopping dominated transport mechanism, while remain nearly no difference in conductivity compared to their analogous PIL homopolymer SPEs, indicating that FSI^- can accelerate ion transport and improve both conductivity and stability. The result suggests that the cation/anion chemistry can cause a significant impact on transport properties, where one

can generate a significant electrochemical property change with a subtle and simple chemical modification (*i.e.*, cation/anion type).

To advance the development of SPE, a PIL pentablock terpolymer (PILPTP) was prepared as a lithium ion conducting ternary SPE by immersing PILPTP thin films into a 1 M Li-TFSI/IL mixture to form ternary blend SPEs. Two different cations in the PIL block (MIm$^+$ and MPyr$^+$) were investigated to understand the influence of cation structure (specifically saturated *versus* unsaturated heterocyclic structure) on the electrochemical stability, ion conductivity, thermal stability, and mechanical properties. The key result from this study is the high ionic conductivity of 0.1 mS cm^{-1} at 28 °C for the MIm$^+$ containing SPE and the promising stability window of 4.2 V *versus* Li/Li$^+$ under room temperature for the MPyr$^+$ containing SPE. The results demonstrate that the PILPTPs have high potential as SPEs for lithium ion batteries with outstanding thermal and electrochemical stabilities and sufficient ionic conductivities.

In a continuing study, similar lithium ion conducting ternary PILPTP SPEs were investigated with the goal of understanding the influence of IL concentration on ion transport mechanisms and electrochemical stability. The impact of imidazolium-based IL (*i.e.*, EMIm-TFSI) was explored in regards to ion transport, morphology, mechanical properties, electrochemical stability, and battery performance. PFG-NMR was utilized to probe the self-diffusion coefficients of individual ionic species in the SPE. Results showed that at high IL concentrations, the IL resides in the PIL conductive domain, depresses the PIL block T$_g$, increases the continuous conductive domain for ion transport, as well as contributes to mechanical percolation. Interestingly, SPE with high IL concentrations also

leads to a reduction of Li^+ cation self-diffusion coefficient and increased overpotential. Lithium ion battery with this ternary SPE shows stable cycling performance over 100 cycles under room temperature. The results demonstrate the ion solvation and transport phenomena in ternary SPEs as well as enable the design of new SPEs for room temperature solid-state lithium ion batteries.

5.2 Future Directions

The work presented in this dissertation can be expanded into multiple opportunities and directions for further development of reliable SPEs. A comprehensive investigation of the structure-to-transport interplay is proposed to unveil and quantify the ion pair interaction for the PIL diblock copolymer SPEs from Chapter II. Further exploration of the mechanical properties and cycling stability relationship for the PIL multiblock copolymer SPEs from Chapter IV can be conducted through both chemical and fabricating methods. Finally, to improve the cycling stability of future SPEs for lithium ion battery, a better understanding of the electrolyte-electrode interfaces and the underlying degradation mechanism would be of interest.

5.2.1 Structure-to-Transport Interplay in PIL Diblock Copolymer SPEs

In Chapter II, the importance of ion pair interaction on the transport properties of PIL diblock copolymer SPE *via* electrochemical measurements was emphasized. One further opportunity that can be explored is to combine multiple experimental techniques to quantify the specific interaction energy between cation/anion pair and corroborate with

the transport properties (*e.g.*, ion self-diffusion coefficient and transference number). Specifically, the direction of the further study is to combine the ion transport characterization method in Chapter II with the self-diffusion coefficient measurement measured *via* PFG-NMR in Chapter IV, as well as the interaction energy study (*e.g.*, wide-angle X-ray scattering (WAXS)[58, 218-220]) to quantify the ion coordination under both macro- and micro-scales. Therefore, one can compare ion pairs under various chemistries (*e.g.*, chain length, ion size, and dielectric constant) with quantifying parameters *(i.e.*, ion-ion correlation length, self-diffusion coefficient, and cation transference number) to develop a comprehensive framework on the ion coordination in solid-state SPEs.

5.2.2 Mechanical Properties on Cycling Performance in PIL Multiblock Copolymer SPEs

Another opportunity for further development would be to expand the mechanical studies of PIL multiblock copolymer SPEs. The main focuses in Chapter III and IV were to investigate the structure-electrochemical property relationships with little discussion on mechanical property investigation. From the literature,[34, 221] theoretical models showed that the mechanical robustness of SPE is important for cycling stability, especially in the lithium metal batteries. However, in the present dissertation, our SPEs exhibit relatively lower mechanical performance (*i.e.*, elastic modulus = 50 MPa) compared with others in the literature[156, 170-171] (*e.g.*, E = 0.3 GPa). The reinforced mechanical properties (*e.g.*, higher tensile strength and elongation of break) in SPEs can be achieved through approaches include: (1) optimizing polymer backbone composition *(e.g.*, polystyrene,

poly(ethylene-r-propylene), and PIL repeat unit ratios), and (2) incorporating the dispersing nano/micro-sized fillers. In the multiblock copolymer, the robustness and flexibility of the SPE thin films can be modified *via* the optimization of the repeat unit ratio from the polymer backbone. Additionally, studies have shown that addition of nano/micro-ceramic fillers (*e.g.*, Al_2O_3, SiO_2, and TiO_2) in SPE hosts also improves the morphological, electrochemical and mechanical properties of the SPEs.[5, 222-224] Additionally, the relationship between mechanical properties and battery cycling lifetime is still unexplored in the literature, which can also provide valuable insights on designing reliable SPEs.

5.2.3 Electrolyte-Electrode Interface and Underlying Chemistry in Solid-State Lithium Ion Battery

The ultimate goal of solid-state lithium battery development is to achieve stable and longer cycling performance. Therefore, designing new battery materials for improved performance requires the understanding of underlying chemistries between the electrolyte-electrode interface and the involved components during the battery charge-discharge cycles. Structural and chemical investigations of the anode solid electrolyte interface (SEI) and cathode surface during the electrochemical cycling can seek a better understanding of the factors that limiting the capacity, as well as the failure mechanism.

The investigation of these thin, disordered, and reactive interfaces requires the incorporation of *ex situ* and *in situ* techniques. Several techniques have been reported in the literature to investigate the interface and electrode, electrolyte surface. *Ex situ*

techniques, such as X-ray photoelectron spectroscopy (XPS)[225] and scanning electron microscopy (SEM) with energy dispersive X-ray spectroscopy (EDS),[226] can be used to study the surface composition and oxidation states, as well as the element distribution on the electrode or the electrolyte surface. Recently, novel *in situ* techniques such as solid-state NMR[227-228] and atomic force microscopy (AFM)[229] allow for chemical and structural property characterization under battery working conditions, which can be used to address the composition of the electrode-electrolyte interface. Results from those studies will elucidate the capacity degradation mechanism and formation of SEI during battery cycling, which will provide guidelines for future modifications of SPEs in lithium batteries with improved stability.

REFERENCES

1. Agency, U. S. E. P. *Inventory of U.S. Greenhouse Gas Emissions and Sinks: 1990-2017*; 2019.

2. Nagaura, T., Lithium ion rechargeable battery. *Progress in Batteries & Solar Cells* **1990,** *9*, 209.

3. Xu, K., Nonaqueous liquid electrolytes for lithium-based rechargeable batteries. *Chemical reviews* **2004,** *104* (10), 4303-4418.

4. Fan, L.; Wei, S.; Li, S.; Li, Q.; Lu, Y., Recent progress of the solid-state electrolytes for high-energy metal-based batteries. *Advanced Energy Materials* **2018,** *8* (11), 1702657.

5. Agrawal, R. C.; Pandey, G. P., Solid polymer electrolytes: materials designing and all-solid-state battery applications: an overview. *Journal of Physics D: Applied Physics* **2008,** *41* (22).

6. Zhang, H.; Li, C.; Piszcz, M.; Coya, E.; Rojo, T.; Rodriguez-Martinez, L. M.; Armand, M.; Zhou, Z., Single lithium-ion conducting solid polymer electrolytes: advances and perspectives. *Chem Soc Rev* **2017,** *46* (3), 797-815.

7. Mindemark, J.; Lacey, M. J.; Bowden, T.; Brandell, D., Beyond PEO—alternative host materials for Li + -conducting solid polymer electrolytes. *Progress in Polymer Science* **2018,** *81*, 114-143.

8. Blomgren, G. E., The development and future of lithium ion batteries. *Journal of The Electrochemical Society* **2017,** *164* (1), A5019-A5025.

9. Zubi, G.; Dufo-López, R.; Carvalho, M.; Pasaoglu, G., The lithium-ion battery: State of the art and future perspectives. *Renewable and Sustainable Energy Reviews* **2018,** *89*, 292-308.

10. Hallinan, D. T.; Balsara, N. P., Polymer electrolytes. *Annual Review of Materials Research* **2013,** *43* (1), 503-525.

11. Marcinek, M.; Syzdek, J.; Marczewski, M.; Piszcz, M.; Niedzicki, L.; Kalita, M.; Plewa-Marczewska, A.; Bitner, A.; Wieczorek, P.; Trzeciak, T.; Kasprzyk, M.; P.Łężak; Zukowska, Z.; Zalewska, A.; Wieczorek, W., Electrolytes for Li-ion transport – review. *Solid State Ionics* **2015,** *276*, 107-126.

12. Fenton, D., Complexes of alkali metal ions with poly (ethylene oxide). *polymer* **1973,** *14*, 589.

13. Ibrahim, S.; Yassin, M. M.; Ahmad, R.; Johan, M. R., Effects of various LiPF6 salt concentrations on PEO-based solid polymer electrolytes. *Ionics* **2011,** *17* (5), 399-405.

14. Munshi, M. Z. A.; Owens, B. B., Ionic Transport in Poly(ethylene oxide) (PEO)-LiX Polymeric Solid Electrolyte. *Polymer Journal* **1988,** *20*, 577–586.

15. Fauteux, C. D. R. a. D., Phase diagrams and conductivity characterization of some PEO - LiX electrolytes. *Journal of The Electrochemical Society* **1986,** *133*, 315-325.

16. Fullerton-Shirey, S. K.; Maranas, J. K., Effect of LiClO4 on the structure and mobility of PEO-based solid polymer electrolytes. *Macromolecules* **2009,** *42* (6), 2142-2156.

17. Henderson, W. A., Crystallization kinetics of glyme-LiX and PEO-LiX polymer electrolytes. *Macromolecules* **2007,** *40*, 4963-4971.

18. Borodin, O.; Smith, G. D., Mechanism of ion transport in amorphous poly(ethylene oxide)/ LiTFSI from molecular dynamics simulations. *Macromolecules* **2006,** *39*, 1620-1629.

19. Bernhard, R.; Latini, A.; Panero, S.; Scrosati, B.; Hassoun, J., Poly(ethylenglycol)dimethylether–lithium bis(trifluoromethanesulfonyl)imide, PEG500DME–LiTFSI, as high viscosity electrolyte for lithium ion batteries. *Journal of Power Sources* **2013,** *226*, 329-333.

20. Abraham, K. M.; Jiang, Z., PEO-Like polymer electrolytes with high room temperature conductivity. *Journal of The Electrochemical Society* **1997,** *144* (6), L136-L138.

21. Cheng, S.; Smith, D. M.; Li, C. Y., How does nanoscale crystalline structure affect ion transport in solid polymer electrolytes? *Macromolecules* **2014,** *47* (12), 3978-3986.

22. Xu, K., Electrolytes and interphases in Li-ion batteries and beyond. *Chem Rev* **2014,** *114* (23), 11503-11618.

23. Gadjourova, Z.; Andreev, Y. G.; Tunstall, D. P.; Bruce, P. G., Ionic conductivity in crystalline polymer electrolytes. *Nature* **2001,** *412*, 520-523.

24. Johansson, P., First principles modelling of amorphous polymer electrolytes: Li+–PEO, Li+–PEI, and Li+–PES complexes. *Polymer* **2001,** *42* (9), 4367-4373.

25. Kim, Y.-T.; Smotkin, E. S., The effect of plasticizers on transport and electrochemicalproperties of PEO-based electrolytes for lithiumrechargeable batteries. *Solid State Ionics* **2002,** *149*, 29–37.

26. Kumar, Y.; Hashmi, S. A.; Pandey, G. P., Lithium ion transport and ion–polymer interaction in PEO based polymer electrolyte plasticized with ionic liquid. *Solid State Ionics* **2011,** *201* (1), 73-80.

27. Wetjen, M.; Navarra, M. A.; Panero, S.; Passerini, S.; Scrosati, B.; Hassoun, J., Composite poly(ethylene oxide) electrolytes plasticized by N-alkyl-N-butylpyrrolidinium bis(trifluoromethanesulfonyl)imide for lithium batteries. *ChemSusChem* **2013,** *6* (6), 1037-43.

28. Vignarooban, K.; Dissanayake, M. A. K. L.; Albinsson, I.; Mellander, B. E., Effect of TiO2 nano-filler and EC plasticizer on electrical and thermal properties of poly(ethylene oxide) (PEO) based solid polymer electrolytes. *Solid State Ionics* **2014,** *266*, 25-28.

29. Srivastava, S.; Schaefer, J. L.; Yang, Z.; Tu, Z.; Archer, L. A., 25th anniversary article: polymer-particle composites: phase stability and applications in electrochemical energy storage. *Adv Mater* **2014,** *26* (2), 201-34.

30. Krawiec, W.; L.G. Scanlon, J.; Fellner, J. P.; Vaia, R. A.; Vasudevan, S.; Giannelis, E. P., Polymer nanocomposites: a new strategy for synthesizing solid electrolytes for rechargeable lithium batteries. *Journal of Power Sources* **1995,** *54*, 310-315.

31. Meyer, W. H., Polymer electrolytes for lithium-ion batteries. *Advanced materials* **1998,** *10.6*, 439-448.

32. Ben youcef, H.; Garcia-Calvo, O.; Lago, N.; Devaraj, S.; Armand, M., Cross-linked solid polymer electrolyte for all-solid-state rechargeable lithium batteries. *Electrochimica Acta* **2016,** *220*, 587-594.

33. Harris, D. J.; Bonagamba, T. J.; Schmidt-Rohr, K.; Soo, P. P.; Sadoway, D. R.; Mayes, A. M., Solid-state NMR investigation of block copolymer electrolyte dynamics. *Macromolecules* **2002,** *35*, 3772-3774.

34. Young, W.-S.; Kuan, W.-F.; Epps, T. H., Block copolymer electrolytes for rechargeable lithium batteries. *Journal of Polymer Science Part B: Polymer Physics* **2014,** *52* (1), 1-16.

35. Thelen, J. L.; Wang, A. A.; Chen, X. C.; Jiang, X.; Schaible, E.; Balsara, N. P., Correlations between salt-induced crystallization, morphology, segmental dynamics, and conductivity in amorphous block copolymer electrolytes. *Macromolecules* **2018,** *51* (5), 1733-1740.

36. Thelen, J. L.; Teran, A. A.; Wang, X.; Garetz, B. A.; Nakamura, I.; Wang, Z.-G.; Balsara, N. P., Phase behavior of a block copolymer/salt mixture through the order-to-disorder transition. *Macromolecules* **2014,** *47* (8), 2666-2673.

37.   Loo, W. S.; Galluzzo, M. D.; Li, X.; Maslyn, J. A.; Oh, H. J.; Mongcopa, K. I.; Zhu, C.; Wang, A. A.; Wang, X.; Garetz, B. A.; Balsara, N. P., Phase behavior of mixtures of block copolymers and a lithium salt. *J Phys Chem B* **2018,** *122* (33), 8065-8074.

38.   Huang, J.; Tong, Z.-Z.; Zhou, B.; Xu, J.-T.; Fan, Z.-Q., Salt-induced microphase separation in poly (ε-caprolactone)-b-poly (ethylene oxide) block copolymer. *Polymer* **2013,** *54* (12), 3098-3106.

39.   Chintapalli, M.; Le, T. N. P.; Venkatesan, N. R.; Mackay, N. G.; Rojas, A. A.; Thelen, J. L.; Chen, X. C.; Devaux, D.; Balsara, N. P., Structure and ionic conductivity of polystyrene-block-poly(ethylene oxide) electrolytes in the high salt concentration limit. *Macromolecules* **2016,** *49* (5), 1770-1780.

40.   Irwin, M. T.; Hickey, R. J.; Xie, S.; Bates, F. S.; Lodge, T. P., Lithium salt-induced microstructure and ordering in diblock copolymer/homopolymer blends. *Macromolecules* **2016,** *49* (13), 4839-4849.

41.   Sarapas, J. M.; Saijo, K.; Zhao, Y.; Takenaka, M.; Tew, G. N., Phase behavior and Li+ Ion conductivity of styrene-ethylene oxide multiblock copolymer electrolytes. *Polymers for Advanced Technologies* **2016,** *27* (7), 946-954.

42.   Metwalli, E.; Rasool, M.; Brunner, S.; Muller-Buschbaum, P., Lithium-salt-containing high-molecular-weight polystyrene-block-polyethylene oxide block copolymer films. *Chemphyschem* **2015,** *16* (13), 2882-2889.

43.   Teran, A. A.; Balsara, N. P., Thermodynamics of block copolymers with and without salt. *J Phys Chem B* **2014,** *118* (1), 4-17.

44.   Nakamura, I.; Wang, Z.-G., Salt-doped block copolymers: ion distribution, domain spacing and effective χ parameter. *Soft Matter* **2012,** *8* (36).

45.   Zardalidis, G.; Gatsouli, K.; Pispas, S.; Mezger, M.; Floudas, G., Ionic conductivity, self-assembly, and viscoelasticity in poly(styrene-b-ethylene oxide) electrolytes doped with LiTf. *Macromolecules* **2015,** *48* (19), 7164-7171.

46.   Young, W.-S.; Epps, T. H., Ionic conductivities of block copolymer electrolytes with various conducting pathways: sample preparation and processing considerations. *Macromolecules* **2012,** *45* (11), 4689-4697.

47.   Young, W.-S.; Thomas H. Epps, I., Salt doping in PEO-containing block copolymers: counterion and concentration effects. *Macromolecules* **2009,** *42*, 2672-2678.

48.   Meek, K. M.; Elabd, Y. A., Polymerized ionic liquid block copolymers for electrochemical energy. *Journal of Materials Chemistry A* **2015,** *3* (48), 24187-24194.

49. Yuan, J.; Mecerreyes, D.; Antonietti, M., Poly(ionic liquid)s: an update. *Progress in Polymer Science* **2013,** *38* (7), 1009-1036.

50. Mecerreyes, D., Polymeric ionic liquids: broadening the properties and applications of polyelectrolytes. *Progress in Polymer Science* **2011,** *36* (12), 1629-1648.

51. Yuan, J.; Antonietti, M., Poly(ionic liquid)s: Polymers expanding classical property profiles. *Polymer* **2011,** *52* (7), 1469-1482.

52. Marcilla, R.; Blazquez, J. A.; Fernandez, R.; Grande, H.; Pomposo, J. A.; Mecerreyes, D., Synthesis of novel polycations using the chemistry of ionic liquids. *Macromolecular Chemistry and Physics* **2005,** *206* (2), 299-304.

53. Shaplov, A. S.; Ponkratov, D. O.; Vygodskii, Y. S., Poly(ionic liquid)s: synthesis, properties, and application. *Polymer Science Series B* **2016,** *58* (2), 73-142.

54. Keith, J. R.; Mogurampelly, S.; Wheatle, B. K.; Ganesan, V., Influence of side chain linker length on ion-transport properties of polymeric ionic liquids. *Journal of Polymer Science Part B: Polymer Physics* **2017,** *55* (23), 1718-1723.

55. Shaplov, A. S.; Marcilla, R.; Mecerreyes, D., Recent advances in innovative polymer electrolytes based on poly(ionic liquid)s. *Electrochimica Acta* **2015,** *175*, 18-34.

56. la Cruz, D. S.-d.; Green, M. D.; Ye, Y.; Elabd, Y. A.; Long, T. E.; Winey, K. I., Correlating backbone-to-backbone distance to ionic conductivity in amorphous polymerized ionic liquids. *Journal of Polymer Science Part B: Polymer Physics* **2012,** *50* (5), 338-346.

57. Choi, U. H.; Ye, Y.; Salas de la Cruz, D.; Liu, W.; Winey, K. I.; Elabd, Y. A.; Runt, J.; Colby, R. H., Dielectric and viscoelastic responses of imidazolium-based ionomers with different counterions and side chain lengths. *Macromolecules* **2014,** *47* (2), 777-790.

58. Iacob, C.; Matsumoto, A.; Brennan, M.; Liu, H.; Paddison, S. J.; Urakawa, O.; Inoue, T.; Sangoro, J.; Runt, J., Polymerized ionic liquids: correlation of ionic conductivity with nanoscale morphology and counterion volume. *ACS Macro Letters* **2017,** *6* (9), 941-946.

59. Shaplov, A. S.; Lozinskaya, E. I.; Ponkratov, D. O.; Malyshkina, I. A.; Vidal, F.; Aubert, P.-H.; Okatova, O. g. V.; Pavlov, G. M.; Komarova, L. I.; Wandrey, C.; Vygodskii, Y. S., Bis(trifluoromethylsulfonyl)amide based "polymeric ionic liquids": Synthesis, purification and peculiarities of structure–properties relationships. *Electrochimica Acta* **2011,** *57*, 74-90.

60. Zhang, H.; Li, L.; Feng, W.; Zhou, Z.; Nie, J., Polymeric ionic liquids based on ether functionalized ammoniums and perfluorinated sulfonimides. *Polymer* **2014,** *55* (16), 3339-3348.

61. Shaplov, A. S.; Ponkratov, D. O.; Vlasov, P. S.; Lozinskaya, E. I.; Komarova, L. I.; Malyshkina, I. A.; Vidal, F.; Nguyen, G. T. M.; Armand, M.; Wandrey, C.; Vygodskii, Y. S., Synthesis and properties of polymeric analogs of ionic liquids. *Polymer Science Series B* **2013,** *55* (3-4), 122-138.

62. Appetecchi, G. B.; Kim, G. T.; Montanino, M.; Carewska, M.; Marcilla, R.; Mecerreyes, D.; De Meatza, I., Ternary polymer electrolytes containing pyrrolidinium-based polymeric ionic liquids for lithium batteries. *Journal of Power Sources* **2010,** *195* (11), 3668-3675.

63. Zhou, Z. B.; Matsumoto, H.; Tatsumi, K., Cyclic quaternary ammonium ionic liquids with perfluoroalkyltrifluoroborates: synthesis, characterization, and properties. *Chemistry* **2006,** *12* (8), 2196-212.

64. Pont, A.-L.; Marcilla, R.; De Meatza, I.; Grande, H.; Mecerreyes, D., Pyrrolidinium-based polymeric ionic liquids as mechanically and electrochemically stable polymer electrolytes. *Journal of Power Sources* **2009,** *188* (2), 558-563.

65. Marcilla, R.; Blazquez, J. A.; Rodriguez, J.; Pomposo, J. A.; Mecerreyes, D., Tuning the solubility of polymerized ionic liquids by simple anion-exchange reactions. *Journal of Polymer Science: Part A: Polymer Chemistry* **2004,** *42*, 208–212

66. Ye, Y.; Elabd, Y. A., Anion exchanged polymerized ionic liquids: High free volume single ion conductors. *Polymer* **2011,** *52* (5), 1309-1317.

67. Vygodskii, Y. S.; Shaplov, A. S.; Lozinskaya, E. I.; Lyssenko, K. A.; Golovanov, D. G.; Malyshkina, I. A.; Gavrilova, N. D.; Buchmeiser, M. R., Conductive polymer electrolytes derived from poly(norbornene)s with pendant ionic imidazolium moieties. *Macromolecular Chemistry and Physics* **2008,** *209* (1), 40-51.

68. Marcilla, R.; Alcaide, F.; Sardon, H.; Pomposo, J. A.; Pozo-Gonzalo, C.; Mecerreyes, D., Tailor-made polymer electrolytes based upon ionic liquids and their application in all-plastic electrochromic devices. *Electrochemistry Communications* **2006,** *8* (3), 482-488.

69. Zhang, H.; Liu, C.; Zheng, L.; Feng, W.; Zhou, Z.; Nie, J., Solid polymer electrolyte comprised of lithium salt/ether functionalized ammonium-based polymeric ionic liquid with bis(fluorosulfonyl)imide. *Electrochimica Acta* **2015,** *159*, 93-101.

70. Yunis, R.; Girard, G. M. A.; Wang, X.; Zhu, H.; Bhattacharyya, A. J.; Howlett, P.; MacFarlane, D. R.; Forsyth, M., The anion effect in ternary electrolyte systems using poly(diallyldimethylammonium) and phosphonium-based ionic liquid with high lithium salt concentration. *Solid State Ionics* **2018,** *327*, 83-92.

71. Ganesan, V., Ion transport in polymeric ionic liquids: recent developments and open questions. *Molecular Systems Design & Engineering* **2019,** *4* (2), 280-293.

72. Griffin, P. J.; Freyer, J. L.; Han, N.; Geller, N.; Yin, X.; Gheewala, C. D.; Lambert, T. H.; Campos, L. M.; Winey, K. I., Ion transport in cyclopropenium-based polymerized ionic liquids. *Macromolecules* **2018,** *51* (5), 1681-1687.

73. Lim, J. Y.; Kim, J. K.; Lee, J. M.; Ryu, D. Y.; Kim, J. H., An amphiphilic block–graft copolymer electrolyte: synthesis, nanostructure, and use in solid-state flexible supercapacitors. *Journal of Materials Chemistry A* **2016,** *4* (20), 7848-7858.

74. Gilbert, J. B.; Luo, M.; Shelton, C. K.; Rubner, M. F.; Cohen, R. E.; Thomas H. Epps, I., Determination of lithium-ion distributions in nanostructured block polymer electrolyte thin films by X-ray photoelectron spectroscopy depth profiling. *ACS Nano* **2015,** *9* (1), 512-520.

75. Wang, J.-Y.; Chen, W.; Russell, T. P., Ion-complexation-induced changes in the interaction parameter and the chain conformation of PS-b-PMMA copolymers. *Macromolecules* **2008,** *41* (13), 4904-4907.

76. Wang, J.-Y.; Chen, W.; Roy, C.; Sievert, J. D.; Russell, T. P., Influence of ionic complexes on phase behavior of polystyrene-b-poly (methyl methacrylate) copolymers. *Macromolecules* **2008,** *41* (3), 963-969.

77. Stancik, C. M.; Lavoie, A. R.; Schütz, J.; Achurra, P. A.; Lindner, P.; Gast, A. P.; Waymouth, R. M., Micelles of imidazolium-functionalized polystyrene diblock copolymers investigated with neutron and light scattering. *Langmuir* **2004,** *20* (3), 596-605.

78. Weber, R. L.; Ye, Y.; Schmitt, A. L.; Banik, S. M.; Elabd, Y. A.; Mahanthappa, M. K., Effect of nanoscale morphology on the conductivity of polymerized ionic liquid block copolymers. *Macromolecules* **2011,** *44* (14), 5727-5735.

79. Choi, J.-H.; Ye, Y.; Elabd, Y. A.; Winey, K. I., Network structure and strong microphase separation for high ion conductivity in polymerized ionic liquid block copolymers. *Macromolecules* **2013,** *46* (13), 5290-5300.

80. Ye, Y.; Choi, J.-H.; Winey, K. I.; Elabd, Y. A., Polymerized ionic liquid block and random copolymers: effect of weak microphase separation on ion transport. *Macromolecules* **2012,** *45* (17), 7027-7035.

81. Li, M.; Yang, L.; Fang, S.; Dong, S., Novel polymeric ionic liquid membranes as solid polymer electrolytes with high ionic conductivity at moderate temperature. *Journal of Membrane Science* **2011,** *366* (1-2), 245-250.

82. Zhang, H.; Feng, W.; Zhou, Z.; Nie, J., Composite electrolytes of lithium salt/polymeric ionic liquid with bis(fluorosulfonyl)imide. *Solid State Ionics* **2014,** *256*, 61-67.

133

83. He, X.; Wang, Z.; Zhou, W.; Jiang, X.; Han, Z.; Chen, D., Imidazolium-functionalized norbornene ionic liquid block copolymer and silica composite electrolyte membranes for lithium-ion batteries. *Journal of Applied Polymer Science* **2017,** *134* (22).

84. Wang, A.; Liu, X.; Wang, S.; Chen, J.; Xu, H.; Xing, Q.; Zhang, L., Polymeric ionic liquid enhanced all-solid-state electrolyte membrane for high-performance lithium-ion batteries. *Electrochimica Acta* **2018,** *276*, 184-193.

85. Li, M.; Wang, L.; Yang, B.; Du, T.; Zhang, Y., Facile preparation of polymer electrolytes based on the polymerized ionic liquid poly((4-vinylbenzyl)trimethylammonium bis(trifluoromethanesulfonylimide)) for lithium secondary batteries. *Electrochimica Acta* **2014,** *123*, 296-302.

86. Nykaza, J. R.; Savage, A. M.; Pan, Q.; Wang, S.; Beyer, F. L.; Tang, M. H.; Li, C. Y.; Elabd, Y. A., Polymerized ionic liquid diblock copolymer as solid-state electrolyte and separator in lithium-ion battery. *Polymer* **2016,** *101*, 311-318.

87. Goujon, N.; Huynh, T. V.; Barlow, K. j.; Kerr, R.; Vezzù, K.; Di Noto, V.; O'Dell, L. A.; Chiefari, J.; Howlett, P. C.; Forsyth, M., Enabling high lithium conductivity in polymerized ionic liquid block copolymer electrolytes. *Batteries & Supercaps* **2018,** *2*, 132-138.

88. Li, M.; Wang, L.; Du, T., Preparation of polymer electrolytes based on the polymerized imidazolium ionic liquid and their applications in lithium batteries. *Journal of Applied Polymer Science* **2014,** *131* (20), n/a-n/a.

89. Safa, M.; Chamaani, A.; Chawla, N.; El-Zahab, B., Polymeric ionic liquid gel electrolyte for room temperature lithium battery applications. *Electrochimica Acta* **2016,** *213*, 587-593.

90. Li, X.; Zhang, Z.; Li, S.; Yang, K.; Yang, L., Polymeric ionic liquid–ionic plastic crystal all-solid-state electrolytes for wide operating temperature range lithium metal batteries. *Journal of Materials Chemistry A* **2017,** *5* (40), 21362-21369.

91. Joost, M.; Kunze, M.; Jeong, S.; Schönhoff, M.; Winter, M.; Passerini, S., Ionic mobility in ternary polymer electrolytes for lithium-ion batteries. *Electrochimica Acta* **2012,** *86*, 330-338.

92. Galluzzo, M. D.; Loo, W. S.; Wang, A. A.; Walton, A.; Maslyn, J. A.; Balsara, N. P., Measurement of three transport coefficients and the thermodynamic factor in block copolymer electrolytes with different morphologies. *J Phys Chem B* **2020,** *124* (5), 921-935.

93. Zhang, Z.; Krajniak, J.; Keith, J. R.; Ganesan, V., Mechanisms of ion transport in block copolymeric polymerized ionic liquids. *ACS Macro Letters* **2019,** *8* (9), 1096-1101.

94.   Mogurampelly, S.; Ganesan, V., Ion transport in polymerized ionic liquid–ionic liquid blends. *Macromolecules* **2018,** *51* (23), 9471-9483.

95.   Mogurampelly, S.; Keith, J. R.; Ganesan, V., Mechanisms underlying ion transport in polymerized ionic liquids. *J Am Chem Soc* **2017,** *139* (28), 9511-9514.

96.   Zugmann, S.; Fleischmann, M.; Amereller, M.; Gschwind, R. M.; Wiemhöfer, H. D.; Gores, H. J., Measurement of transference numbers for lithium ion electrolytes via four different methods, a comparative study. *Electrochimica Acta* **2011,** *56* (11), 3926-3933.

97.   Evans, J.; A.Vincent, C.; G.Bruce, P., Electrochemical measurement of transference numbers in polymer electrolytes. *Polymer* **1987,** *28* (13), 2324-2328.

98.   Hafezi, H.; Newman, J., Verification and analysis of transference number measurements by the galvanostatic polarization method. *Journal of The Electrochemical Society* **2000,** *146* (8), 3036-3042.

99.   Pesko, D. M.; Timachova, K.; Bhattacharya, R.; Smith, M. C.; Villaluenga, I.; Newman, J.; Balsara, N. P., Negative transference numbers in poly(ethylene oxide)-based electrolytes. *Journal of The Electrochemical Society* **2017,** *164* (11), E3569-E3575.

100.   Ma, Y.; Doyle, M.; Fuller, T. F.; Doeff, M. M.; Jonghe, L. C. D.; Newman, J., The measurement of a complete set of transport properties for a concentrated solid polymer electrolyte solution. *Journal of The Electrochemical Society* **1995,** *142* (6), 1859-1868.

101.   Villaluenga, I.; Pesko, D. M.; Timachova, K.; Feng, Z.; Newman, J.; Srinivasan, V.; Balsara, N. P., Negative Stefan-Maxwell diffusion coefficients and complete electrochemical transport characterization of homopolymer and block copolymer electrolytes. *Journal of The Electrochemical Society* **2018,** *165* (11), A2766-A2773.

102.   Sun, R.; Elabd, Y. A., Synthesis and high alkaline chemical stability of polyionic liquids with methylpyrrolidinium, methylpiperidinium, methylazepanium, methylazocanium, and methylazonanium cations. *ACS Macro Letters* **2019**, 540-545.

103.   Ye, C.; Shreeve, J. M., Rapid and accurate estimation of densities of room-temperature ionic liquids and salts. *The Journal of Physical Chemistry A* **2007,** *111* (8), 1456-1461.

104.   Tzu-Ling Chen; Rui Sun; Carl Willis; Brian Morgan; Fredrick L. Beyer; Elabd, Y. A., Lithium ion conducting polymerized ionic liquid pentablock terpolymers as solid-state electrolytes. *Polymer* **2019,** *161*, 128-138.

105.   Moreno, M.; Simonetti, E.; Appetecchi, G.; Carewska, M.; Montanino, M.; Kim, G.-T.; Loeffler, N.; Passerini, S., Ionic liquid electrolytes for safer lithium batteries I. investigation around optimal formulation. *Journal of The Electrochemical Society* **2017,** *164* (1), A6026-A6031.

106.   Baskaran, R.; Selvasekarapandian, S.; Kuwata, N.; Kawamura, J.; Hattori, T., Conductivity and thermal studies of blend polymer electrolytes based on PVAc–PMMA. *Solid State Ionics* **2006,** *177* (26-32), 2679-2682.

107.   Metwalli, E.; Kaeppel, M. V.; Schaper, S. J.; Kriele, A.; Gilles, R.; Raftopoulos, K. N.; Müller-Buschbaum, P., Conductivity and morphology correlations of ionic-liquid/lithium-salt/block copolymer nanostructured hybrid electrolytes. *ACS Applied Energy Materials* **2018,** *1* (2), 666-675.

108.   Zhu, Q.; Song, Y.; Zhu, X.; Wang, X., Ionic liquid-based electrolytes for capacitor applications. *Journal of Electroanalytical Chemistry* **2007,** *601* (1-2), 229-236.

109.   MacFarlane, D. R., Meakin, P., Sun, J., Amini, N., and Forsyth, M., Pyrrolidinium imides: A new family of molten aalts and conductive plastic crystal phases. *The Journal of Physical Chemistry B* **1999,** *103* (20), 4164-4170.

110.   Kerner, M.; Plylahan, N.; Scheers, J.; Johansson, P., Ionic liquid based lithium battery electrolytes: fundamental benefits of utilising both TFSI and FSI anions? *Phys Chem Chem Phys* **2015,** *17* (29), 19569-81.

111.   Tsuzuki, S.; Hayamizu, K.; Seki, S., Origin of the low-viscosity of [emim][(FSO2)2N] ionic liquid and its lithium salt mixture: experimental and theoretical study of self-diffusion coefficients, conductivities, and intermolecular interactions. *Journal of Physical Chemistry B* **2010,** *114*, 16329–16336.

112.   May, A. W.; Shi, Z.; Wijayasekara, D. B.; Gin, D. L.; Bailey, T. S., Self-assembly of highly asymmetric, poly(ionic liquid)-rich diblock copolymers and the effects of simple structural modification on phase behaviour. *Polymer Chemistry* **2019,** *10* (6), 751-765.

113.   Ye, Y.; Sharick, S.; Davis, E. M.; Winey, K. I.; Elabd, Y. A., High hydroxide conductivity in polymerized ionic liquid block copolymers. *ACS Macro Letters* **2013,** *2* (7), 575-580.

114.   Meek, K. M.; Sharick, S.; Ye, Y.; Winey, K. I.; Elabd, Y. A., Bromide and hydroxide conductivity–morphology relationships in polymerized ionic liquid block copolymers. *Macromolecules* **2015,** *48* (14), 4850-4862.

115.   Makino, T.; Kanakubo, M.; Umecky, T.; Suzuki, A.; Nishida, T.; Takano, J., Electrical conductivities, viscosities, and densities of N-methoxymethyl- and N-butyl-N-methylpyrrolidinium ionic liquids with the bis(fluorosulfonyl)amide anion. *Journal of Chemical & Engineering Data* **2012,** *57* (3), 751-755.

116.   Hiemenz, P. C.; Lodge, T. P., *Polymer Chemistry*. CRC Press: 2007.

117.   Fulcher, G. S., Analysis of recent measurements of the viscosity of glasses. *Journal of the American Ceramic Society* **1925,** *8* (6), 339-355.

118. Umebayashi, Y.; Hamano, H.; Seki, S.; Minofar, B.; Fujii, K.; Hayamizu, K.; Tsuzuki, S.; Kameda, Y.; Kohara, S.; Watanabe, M., Liquid structure of and Li+ ion solvation in bis(trifluoromethanesulfonyl)amide based ionic liquids composed of 1-ethyl-3-methylimidazolium and N-methyl-N-propylpyrrolidinium cations. *J Phys Chem B* **2011,** *115* (42), 12179-91.

119. Liu, H.; Maginn, E., Effect of ion structure on conductivity in lithium-doped ionic liquid electrolytes: a molecular dynamics study. *J Chem Phys* **2013,** *139* (11), 114508.

120. Borodin, O.; Giffin, G. A.; Moretti, A.; Haskins, J. B.; Lawson, J. W.; Henderson, W. A.; Passerini, S., Insights into the structure and transport of the lithium, sodium, magnesium, and zinc bis(trifluoromethansulfonyl)imide aalts in ionic liquids. *The Journal of Physical Chemistry C* **2018,** *122* (35), 20108-20121.

121. Li, Z.; Smith, G. D.; Bedrov, D., Li+ solvation and transport properties in ionic liquid/lithium salt mixtures: a molecular dynamics simulation study. *J Phys Chem B* **2012,** *116* (42), 12801-9.

122. Lassegues, J. C.; Grondin, J.; Talaga, D., Lithium solvation in bis(trifluoromethanesulfonyl)imide-based ionic liquids. *Phys Chem Chem Phys* **2006,** *8* (48), 5629-5632.

123. Fujii, K.; Hamano, H.; Doi, H.; Song, X.; Tsuzuki, S.; Hayamizu, K.; Seki, S.; Kameda, Y.; Dokko, K.; Watanabe, M.; Umebayashi, Y., Unusual Li+ ion solvation structure in bis(fluorosulfonyl)amide based ionic liquid. *The Journal of Physical Chemistry C* **2013,** *117* (38), 19314-19324.

124. Grande, L.; von Zamory, J.; Koch, S. L.; Kalhoff, J.; Paillard, E.; Passerini, S., Homogeneous lithium electrodeposition with pyrrolidinium-based ionic liquid electrolytes. *ACS Appl Mater Interfaces* **2015,** *7* (10), 5950-5958.

125. Girard, G. M. A.; Wang, X.; Yunis, R.; MacFarlane, D. R.; Bhattacharyya, A. J.; Forsyth, M.; Howlett, P. C., Sustainable, dendrite free lithium-metal electrode cycling achieved with polymer composite electrolytes based on a poly(Ionic liquid) host. *Batteries & Supercaps* **2019,** *2* (3), 229-239.

126. Girard, G. M. A.; Hilder, M.; Nucciarone, D.; Whitbread, K.; Zavorine, S.; Moser, M.; Forsyth, M.; MacFarlane, D. R.; Howlett, P. C., Role of Li concentration and the SEI layer in enabling high performance Li metal electrodes using a phosphonium bis(fluorosulfonyl)imide ionic liquid. *The Journal of Physical Chemistry C* **2017,** *121* (39), 21087-21095.

127. Bhatt, A. I.; Kao, P.; Best, A. S.; Hollenkamp, A. F., Understanding the morphological changes of lithium surfaces during cycling in electrolyte solutions of lithium salts in an ionic liquid. *Journal of The Electrochemical Society* **2013,** *160* (8), A1171-A1180.

128.	Tsuzuki, S.; Hayamizu, K.; Seki, S., Origin of the low-viscosity of [emim][(FSO2) 2N] ionic liquid and its lithium salt mixture: experimental and theoretical study of self-diffusion coefficients, conductivities, and intermolecular interactions. *The Journal of Physical Chemistry B* **2010,** *114* (49), 16329-16336.

129.	Hayamizu, K.; Tsuzuki, S.; Seki, S.; Fujii, K.; Suenaga, M.; Umebayashi, Y., Studies on the translational and rotational motions of ionic liquids composed of N-methyl-N-propyl-pyrrolidinium (P13) cation and bis(trifluoromethanesulfonyl)amide and bis(fluorosulfonyl)amide anions and their binary systems including lithium salts. *J Chem Phys* **2010,** *133* (19), 194505.

130.	Inceoglu, S.; Rojas, A. A.; Devaux, D.; Chen, X. C.; Stone, G. M.; Balsara, N. P., Morphology–conductivity relationship of single-ion-conducting block copolymer electrolytes for lithium batteries. *ACS Macro Letters* **2014,** *3* (6), 510-514.

131.	Meek, K. M.; Sun, R.; Willis, C.; Elabd, Y. A., Hydroxide conducting polymerized ionic liquid pentablock terpolymer anion exchange membranes with methylpyrrolidinium cations. *Polymer* **2018,** *134,* 221-226.

132.	Wang, J.; He, X.; Zhu, H.; Chen, D., Preparation of a ROMP-type imidazolium-functionalized norbornene ionic liquid block copolymer and the electrochemical property for lithium-ion batteries polyelectrolyte membranes. *RSC Advances* **2015,** *5* (54), 43581-43588.

133.	Yin, K.; Zhang, Z.; Yang, L.; Hirano, S.-I., An imidazolium-based polymerized ionic liquid via novel synthetic strategy as polymer electrolytes for lithium ion batteries. *Journal of Power Sources* **2014,** *258,* 150-154.

134.	Borgel, V.; Markevich, E.; Aurbach, D.; Semrau, G.; Schmidt, M., On the application of ionic liquids for rechargeable Li batteries: high voltage systems. *Journal of Power Sources* **2009,** *189* (1), 331-336.

135.	Li, L.; Wang, J.; Yang, P.; Guo, S.; Wang, H.; Yang, X.; Ma, X.; Yang, S.; Wu, B., Preparation and characterization of gel polymer electrolytes containing N-butyl-N-methylpyrrolidinium bis (trifluoromethanesulfonyl) imide ionic liquid for lithium ion batteries. *Electrochimica Acta* **2013,** *88,* 147-156.

136.	Vogl, T.; Goodrich, P.; Jacquemin, J.; Passerini, S.; Balducci, A., The influence of cation structure on the chemical–physical properties of protic ionic liquids. *The Journal of Physical Chemistry C* **2016,** *120* (16), 8525-8533.

137.	Ueno, K.; Tokuda, H.; Watanabe, M., Ionicity in ionic liquids: correlation with ionic structure and physicochemical properties. *Physical Chemistry Chemical Physics* **2010,** *12* (8), 1649-1658.

138. Rui Sun; Monica Hwang; Carl Willis; Brian Morgan; Fredrick L. Beyer; Elabd, Y. A., Hydroxide conducting polymerized ionic liquid pentablock terpolymer anion exchange membranes with various cations. **2018**.

139. Ilavsky, J., Nika: software for two-dimensional data reduction. *Journal of Applied Crystallography* **2012,** *45* (2), 324-328.

140. Ilavsky, J.; Jemian, P. R., Irena: tool suite for modeling and analysis of small-angle scattering. *Journal of Applied Crystallography* **2009,** *42* (2), 347-353.

141. Gwee, L.; Choi, J.-H.; Winey, K. I.; Elabd, Y. A., Block copolymer/ionic liquid films: The effect of ionic liquid composition on morphology and ion conduction. *Polymer* **2010,** *51* (23), 5516-5524.

142. Du, Q.; Fu, X.; Liu, S.; Niu, L.; Wang, G.; Zou, X., Polymer Electrolytes based on polymeric ionic Liquid poly (methyl 2-(3-vinylimidazolidin-1-yl) acetate bis (trifluoromethane sulfonyl)imide). *Journal of Inorganic and Organometallic Polymers and Materials* **2012,** *22* (2), 316-323.

143. Milligan, D. E.; Jacox, M. E., Matrix-isolation study of the reaction of atomic and molecular fluorine with carbon atoms. The infrared spectra of normal and 13C-substituted CF2 and CF3. *The Journal of Chemical Physics* **1968,** *48* (5), 2265-2271.

144. G. B. Appetecchi, S. S., and S. Passerini, Investigation on the Stability of the Lithium-Polymer Electrolyte Interface. *Journal of The Electrochemical Society* **2000,** *147* (12), 4448-4452.

145. F. Capuano, F. C., and B. Scrosati, Composite Polymer Electrolytes. *Journal of the Electrochemical Society* **1991,** *138.7* 1918-1922.

146. Li, N. W.; Yin, Y. X.; Li, J. Y.; Zhang, C. H.; Guo, Y. G., Passivation of lithium metal anode via hybrid ionic liquid electrolyte toward stable Li plating/stripping. *Adv Sci (Weinh)* **2017,** *4* (2), 1600400.

147. Nádherná, M.; Reiter, J.; Moškon, J.; Dominko, R., Lithium bis (fluorosulfonyl) imide–PYR14TFSI ionic liquid electrolyte compatible with graphite. *Journal of power sources* **2011,** *196* (18), 7700-7706.

148. Izutsu, K., *Electrochemistry in nonaqueous solutions*. John Wiley & Sons: 2009.

149. Brinkkötter, M.; Lozinskaya, E. I.; Ponkratov, D. O.; Vlasov, P. S.; Rosenwinkel, M. P.; Malyshkina, I. A.; Vygodskii, Y.; Shaplov, A. S.; Schönhoff, M., Influence of anion structure on ion dynamics in polymer gel electrolytes composed of poly(ionic liquid), ionic liquid and Li salt. *Electrochimica Acta* **2017,** *237*, 237-247.

150. Garcia, B.; Lavallée, S.; Perron, G.; Michot, C.; Armand, M., Room temperature molten salts as lithium battery electrolyte. *Electrochimica Acta* **2004,** *49* (26), 4583-4588.

151. De Vos, N.; Maton, C.; Stevens, C. V., Electrochemical stability of ionic liquids: general influences and degradation mechanisms. *ChemElectroChem* **2014,** *1* (8), 1258-1270.

152. Lagrost, P. H. a. C., Electrochemical reactivity in room-temperature ionic liquids. *Chemical Reviews* **2008,** *108* (7), 2238-2264.

153. Belhocine, T.; Forsyth, S. A.; Gunaratne, H. Q. N.; Nieuwenhuyzen, M.; Puga, A. V.; Seddon, K. R.; Srinivasan, G.; Whiston, K., New ionic liquids from azepane and 3-methylpiperidine exhibiting wide electrochemical windows. *Green Chem.* **2011,** *13* (1), 59-63.

154. Bouchet, R.; Maria, S.; Meziane, R.; Aboulaich, A.; Lienafa, L.; Bonnet, J.-P.; Phan, T. N.; Bertin, D.; Gigmes, D.; Devaux, D., Single-ion BAB triblock copolymers as highly efficient electrolytes for lithium-metal batteries. *Nature materials* **2013,** *12* (5), 452.

155. Porcarelli, L.; Aboudzadeh, M. A.; Rubatat, L.; Nair, J. R.; Shaplov, A. S.; Gerbaldi, C.; Mecerreyes, D., Single-ion triblock copolymer electrolytes based on poly(ethylene oxide) and methacrylic sulfonamide blocks for lithium metal batteries. *Journal of Power Sources* **2017,** *364*, 191-199.

156. Chopade, S. A.; Au, J. G.; Li, Z.; Schmidt, P. W.; Hillmyer, M. A.; Lodge, T. P., Robust polymer electrolyte membranes with high ambient-temperature lithium-ion conductivity via polymerization-induced microphase separation. *ACS Applied Materials & Interfaces* **2017,** *9* (17), 14561-14565.

157. Green, M. D.; Wang, D.; Hemp, S. T.; Choi, J.-H.; Winey, K. I.; Heflin, J. R.; Long, T. E., Synthesis of imidazolium ABA triblock copolymers for electromechanical transducers. *Polymer* **2012,** *53* (17), 3677-3686.

158. Evans, C. M.; Sanoja, G. E.; Popere, B. C.; Segalman, R. A., Anhydrous proton transport in polymerized ionic liquid block copolymers: roles of block length, ionic content, and confinement. *Macromolecules* **2015,** *49* (1), 395-404.

159. Fan, F.; Wang, Y.; Hong, T.; Heres, M. F.; Saito, T.; Sokolov, A. P., Ion conduction in polymerized ionic liquids with different pendant groups. *Macromolecules* **2015,** *48* (13), 4461-4470.

160. Wang, Y.; Fan, F.; Agapov, A. L.; Saito, T.; Yang, J.; Yu, X.; Hong, K.; Mays, J.; Sokolov, A. P., Examination of the fundamental relation between ionic transport and segmental relaxation in polymer electrolytes. *Polymer* **2014,** *55* (16), 4067-4076.

161. Dagousset, L.; Nguyen, G. T. M.; Vidal, F.; Galindo, C.; Aubert, P.-H., Ionic liquids and γ-butyrolactone mixtures as electrolytes for supercapacitors operating over extended temperature ranges. *RSC Advances* **2015,** *5* (17), 13095-13101.

162. Ogihara, W.; Washiro, S.; Nakajima, H.; Ohno, H., Effect of cation structure on the electrochemical and thermal properties of ion conductive polymers obtained from polymerizable ionic liquids. *Electrochimica Acta* **2006,** *51* (13), 2614-2619.

163. Kazuo Murata, S. I., Youetsu Yoshihisa, An overview of the research and development of solid polymer electrolyte batteries. *Electrochimica acta* **2000,** *45* (8-9), 1501-1508.

164. Osada, I.; de Vries, H.; Scrosati, B.; Passerini, S., Ionic-liquid-based polymer electrolytes for battery applications. *Angew Chem Int Ed Engl* **2016,** *55* (2), 500-513.

165. Tokuda, H.; Hayamizu, K.; Ishii, K.; Susan, M. A. B. H.; Watanabe, M., Physicochemical properties and structures of room temperature ionic liquids. 1. Variation of anionic species. *The Journal of Physical Chemistry B* **2004,** *108* (42), 16593-16600.

166. Zhang, S.; Sun, N.; He, X.; Lu, X.; Zhang, X., Physical properties of ionic liquids: database and evaluation. *Journal of Physical and Chemical Reference Data* **2006,** *35* (4), 1475-1517.

167. Pringle, J. M.; Golding, J.; Baranyai, K.; Forsyth, C. M.; Deacon, G. B.; Scott, J. L.; MacFarlane, D. R., The effect of anion fluorination in ionic liquids—physical properties of a range of bis(methanesulfonyl)amide salts. *New J. Chem.* **2003,** *27* (10), 1504-1510.

168. N. Llewellyn Lancaster, P. A. S., Tom Welton, and G. Brent Young, Nucleophilicity in ionic liquids. 2.1 Cation effects on halide nucleophilicity in a series of bis(trifluoromethylsulfonyl)imide ionic liquids. *The Journal of organic chemistry* **2002,** *67* (25), 8855-8861.

169. Maton, C.; De Vos, N.; Stevens, C. V., Ionic liquid thermal stabilities: decomposition mechanisms and analysis tools. *Chem Soc Rev* **2013,** *42* (13), 5963-77.

170. Ji, J.; Keen, J.; Zhong, W.-H., Simultaneous improvement in ionic conductivity and mechanical properties of multi-functional block-copolymer modified solid polymer electrolytes for lithium ion batteries. *Journal of Power Sources* **2011,** *196* (23), 10163-10168.

171. Niitani, T.; Shimada, M.; Kawamura, K.; Kanamura, K., Characteristics of new-type solid polymer electrolyte controlling nano-structure. *Journal of Power Sources* **2005,** *146* (1-2), 386-390.

172.   Park, M. J.; Choi, I.; Hong, J.; Kim, O., Polymer electrolytes integrated with ionic liquids for future electrochemical devices. *Journal of Applied Polymer Science* **2013,** *129* (5), 2363-2376.

173.   Imaizumi, S.; Kato, Y.; Kokubo, H.; Watanabe, M., Driving mechanisms of ionic polymer actuators having electric double layer capacitor structures. *J Phys Chem B* **2012,** *116* (16), 5080-5089.

174.   Seki, S.; Susan, M. A.; Kaneko, T.; Tokuda, H.; Noda, A.; Watanabe, M., Distinct difference in ionic transport behavior in polymer electrolytes depending on the matrix polymers and incorporated salts. *J Phys Chem B* **2005,** *109* (9), 3886-3892.

175.   Li, X.; Li, S.; Zhang, Z.; Huang, J.; Yang, L.; Hirano, S.-i., High-performance polymeric ionic liquid–silica hybrid ionogel electrolytes for lithium metal batteries. *Journal of Materials Chemistry A* **2016,** *4* (36), 13822-13829.

176.   Zhou, D.; Liu, R.; Zhang, J.; Qi, X.; He, Y.-B.; Li, B.; Yang, Q.-H.; Hu, Y.-S.; Kang, F., In situ synthesis of hierarchical poly (ionic liquid)-based solid electrolytes for high-safety lithium-ion and sodium-ion batteries. *Nano Energy* **2017,** *33*, 45-54.

177.   Safa, M.; Hao, Y.; Chamaani, A.; Adelowo, E.; Chawla, N.; Wang, C.; El-Zahab, B., Capacity fading mechanism in lithium-sulfur battery using poly (ionic liquid) gel electrolyte. *Electrochimica Acta* **2017,** *258*, 1284-1292.

178.   Rahman, M.; Brazel, C. S., Ionic liquids: New generation stable plasticizers for poly (vinyl chloride). *Polymer Degradation and Stability* **2006,** *91* (12), 3371-3382.

179.   McIntosh, L. D.; Kubo, T.; Lodge, T. P., Morphology, modulus, and conductivity of a triblock terpolymer/ionic liquid electrolyte membrane. *Macromolecules* **2014,** *47* (3), 1090-1098.

180.   Zhang, S.; Lee, K. H.; Frisbie, C. D.; Lodge, T. P., Ionic conductivity, capacitance, and viscoelastic properties of block copolymer-based ion gels. *Macromolecules* **2011,** *44* (4), 940-949.

181.   Stejskal, E. O.; Tanner, J. E., Spin diffusion measurements: spin echoes in the presence of a time-dependent field gradient. *The Journal of Chemical Physics* **1965,** *42* (1), 288-292.

182.   Buschmann, H.; Dolle, J.; Berendts, S.; Kuhn, A.; Bottke, P.; Wilkening, M.; Heitjans, P.; Senyshyn, A.; Ehrenberg, H.; Lotnyk, A.; Duppel, V.; Kienle, L.; Janek, J., Structure and dynamics of the fast lithium ion conductor "Li7La3Zr2O12". *Phys Chem Chem Phys* **2011,** *13* (43), 19378-19392.

183. Han, K. S.; Chen, J.; Cao, R.; Rajput, N. N.; Murugesan, V.; Shi, L.; Pan, H.; Zhang, J.-G.; Liu, J.; Persson, K. A.; Mueller, K. T., Effects of anion mobility on electrochemical behaviors of lithium–sulfur batteries. *Chemistry of Materials* **2017,** *29* (21), 9023-9029.

184. Carper, W. R., and Charles E. Keller, Direct determination of NMR correlation times from spin-lattice and spin-spin relaxation times. *The Journal of Physical Chemistry A* **1997,** *101* (18), 3246-3250.

185. Bennett, T. M.; Jack, K. S.; Thurecht, K. J.; Blakey, I., Perturbation of the experimental phase diagram of a diblock copolymer by blending with an ionic liquid. *Macromolecules* **2015,** *49* (1), 205-214.

186. Virgili, J. M.; Nedoma, A. J.; Segalman, R. A.; Balsara, N. P., Ionic liquid distribution in ordered block copolymer solutions. *Macromolecules* **2010,** *43* (8), 3750-3756.

187. Hoarfrost, M. L.; Segalman, R. A., Ionic conductivity of nanostructured block copolymer/ionic liquid membranes. *Macromolecules* **2011,** *44* (13), 5281-5288.

188. Ye, Y.-S.; Rick, J.; Hwang, B.-J., Ionic liquid polymer electrolytes. *J. Mater. Chem. A* **2013,** *1* (8), 2719-2743.

189. Li, C.; Goodman, S. L.; Albrecht, R. M.; Cooper, S. L., Morphology of segmented polybutadiene-polyurethane elastomers. *Macromolecules* **1988,** *21* (8), 2367-2375.

190. Bates, F. S.; Berney, C.; Cohen, R., Microphase structure of solvent-cast diblock copolymers and copolymer-homopolymer blends containing spherical microdomains. *Macromolecules* **1983,** *16* (7), 1101-1108.

191. Winey, K. I.; Thomas, E. L.; Fetters, L. J., Isothermal morphology diagrams for binary blends of diblock copolymer and homopolymer. *Macromolecules* **1992,** *25* (10), 2645-2650.

192. Lodge, T. P.; Xu, X.; Ryu, C. Y.; Hamley, I. W.; Fairclough, J. P. A.; Ryan, A. J.; Pedersen, J. S., Structure and dynamics of concentrated solutions of asymmetric block copolymers in slightly selective solvents. *Macromolecules* **1996,** *29* (18), 5955-5964.

193. Lai, C. J.; Russel, W. B.; Register, R. A., Phase behavior of styrene-isoprene diblock copolymers in strongly selective solvents. *Macromolecules* **2002,** *35* (3), 841-849.

194. Shibayama, M.; Hashimoto, T.; Kawai, H., Ordered structure in block polymer solutions. 1. Selective solvents. *Macromolecules* **1983,** *16* (1), 16-28.

195. King, M. R.; White, S. A.; Smith, S. D.; Spontak, R. J., Mesogel networks via selective midblock swelling of lamellar triblock copolymers. *Langmuir* **1999,** *15* (23), 7886-7889.

196.   Bates, F. S.; Fredrickson, G. H., Block copolymer thermodynamics: theory and experiment. *Annual Review of Physical Chemistry* **1990,** *41* (1), 525-557.

197.   Fredrickson, G. H.; Bates, F. S., Dynamics of block copolymers: Theory and experiment. *Annual Review of Materials Science* **1996,** *26* (1), 501-550.

198.   L.M. Carvalho; P. Guegan; H. Cheradame; Gomes, A. S., Variation of the mesh size of PEO-based networks filled with TFSILi: from an Arrhenius to WLF type conductivity behavior. *European polymer journal* **2000,** *32* (2), 401-409.

199.   Malcolm L. Williams; Robert F. Landel; Ferry., J. D., The temperature dependence of relaxation mechanisms in amorphous polymers and other glass-forming liquids. *Journal of the American Chemical Society* **1955,** *77* (14), 3701-3707.

200.   Miyamoto, T.; Shibayama, K., Free-volume model for ionic conductivity in polymers. *Journal of Applied Physics* **1973,** *44* (12), 5372-5376.

201.   Stolwijk, N. A.; Wiencierz, M.; Heddier, C.; Kosters, J., What can we learn from ionic conductivity measurements in polymer electrolytes? A case study on poly(ethylene oxide) (PEO)-NaI and PEO-LiTFSI. *J Phys Chem B* **2012,** *116* (10), 3065-3074.

202.   Corrie T. Imrie; Ingram, M. D.; McHattie, G. S., Ion transport in glassy side-group liquid crystalline polymer electrolytes. *Advanced Materials* **1999,** *11*, 832-834.

203.   C. Austen Angell; Corrie T. Imrie; Ingram, M. D., From simple electrolyte solutions through polymer electrolytes to superionic rubbers: some fundamental considerations. *Polymer International* **1998,** *47*, 9-15.

204.   Tipton, A. L., Mark C. Lonergan, Mark A. Ratner, Duward F. Shriver, Thomas TY Wong, and Keli Han, Conductivity and dielectric constant of PPO and PPO-based solid electrolytes from Dc to 6 GHz. *The Journal of Physical Chemistry B* **1994,** *98* (15), 4148-4154.

205.   Ohno, H., Norihisa Kobayashi, Shinji Takeoka, Hajime Ishizaka, and Eishun Tsuchida., Larger cations can move faster in solid polymer electrolytes. *Solid State Ionics* **1990,** *40*, 655-658.

206.   M.E. Broz, D. L. V., N.R. Washburn, Structure and mechanical properties of poly(D,L-lactic acid)/poly(ε-caprolactone) blends. *Biomaterials* **2003,** *24* (23), 4181-4190.

207.   Berne, L. M. R. a. R. A., Mechanical properties of emulsion polymer blends. *Journal of Polymer Science Part B: Polymer Physics* **2001,** *39* (11), 1093-1106.

208.   Wu, W. Y. H. S., Percolation behavior in morphology and modulus of polymer blends. *Polymer Engineering & Science* **1993,** *33* (5), 293-302.

209. Lionel Flandin , Y. B., and J.-Y. Cavaille, Electrically conductive polymer nanocomposites as deformation sensors. *Composites Science and Technology* **2001,** *61* (6), 895-901.

210. Basile, A.; Bhatt, A. I.; O'Mullane, A. P., Stabilizing lithium metal using ionic liquids for long-lived batteries. *Nature Communiations* **2016,** *7* (1), 1-11.

211. Diederichsen, K. M.; McShane, E. J.; McCloskey, B. D., Promising routes to a high Li+ transference number electrolyte for lithium ion batteries. *ACS Energy Letters* **2017,** *2* (11), 2563-2575.

212. Kim, D.-H.; Hwang, S.; Cho, J.-J.; Yu, S.; Kim, S.; Jeon, J.; Ahn, K. H.; Lee, C.; Song, H.-K.; Lee, H., Toward fast operation of lithium batteries: ion activity as the factor to determine the concentration polarization. *ACS Energy Letters* **2019,** *4* (6), 1265-1270.

213. Park, S. K.; Han, K. S.; Lee, J. H.; Murugesan, V.; Lee, S. H.; Koo, C. M.; Lee, J. S.; Mueller, K. T., Evolution of ion–ion interactions and structures in smectic ionic liquid crystals. *The Journal of Physical Chemistry C* **2019,** *123* (33), 20547-20557.

214. Sandhya, C.; John, B.; Gouri, C., Lithium titanate as anode material for lithium-ion cells: a review. *Ionics* **2014,** *20* (5), 601-620.

215. Chen, Z.; Belharouak, I.; Sun, Y. K.; Amine, K., Titanium-based anode materials for safe lithium-ion batteries. *Advanced Functional Materials* **2013,** *23* (8), 959-969.

216. Inda, Y.; Katoh, T.; Baba, M., Development of all-solid lithium-ion battery using Li-ion conducting glass-ceramics. *Journal of Power Sources* **2007,** *174* (2), 741-744.

217. Aliahmad, N.; Shrestha, S.; Varahramyan, K.; Agarwal, M., Poly(vinylidene fluoride-hexafluoropropylene) polymer electrolyte for paper-based and flexible battery applications. *AIP Advances* **2016,** *6* (6), 065206.

218. Heres, M.; Cosby, T.; Mapesa, E. U.; Liu, H.; Berdzinski, S.; Strehmel, V.; Dadmun, M.; Paddison, S. J.; Sangoro, J., Ion transport in glassy polymerized ionic liquids: unraveling the impact of the molecular structure. *Macromolecules* **2018,** *52* (1), 88-95.

219. Zhao, J.; Lei, Q.; He, F.; Zheng, C.; Liu, Y.; Zhao, X.; Yin, J., Nonmonotonic influence of size of quaternary ammonium countercations on micromorphology, polarization, and electroresponse of anionic poly(ionic liquid)s. *J Phys Chem B* **2020,** *124* (14), 2920-2929.

220. Doughty, B.; Genix, A. C.; Popov, I.; Li, B.; Zhao, S.; Saito, T.; Lutterman, D. A.; Sacci, R. L.; Sumpter, B. G.; Wojnarowska, Z.; Bocharova, V., Structural correlations tailor conductive properties in polymerized ionic liquids. *Phys Chem Chem Phys* **2019,** *21* (27), 14775-14785.

221.	Monroe, C.; Newman, J., The impact of elastic deformation on deposition kinetics at lithium/polymer interfaces. *Journal of The Electrochemical Society* **2005,** *152* (2).

222.	Croce, F.; Sacchetti, S.; Scrosati, B., Advanced, lithium batteries based on high-performance composite polymer electrolytes. *Journal of Power Sources* **2006,** *162* (1), 685-689.

223.	Bronstein, L. M.; Karlinsey, R. L.; Ritter, K.; Joo, C. G.; Stein, B.; Zwanziger, J. W., Design of organic–inorganic solid polymer electrolytes: synthesis, structure, and properties. *J. Mater. Chem.* **2004,** *14* (12), 1812-1820.

224.	Croce, F.; Settimi, L.; Scrosati, B., Superacid ZrO2-added, composite polymer electrolytes with improved transport properties. *Electrochemistry Communications* **2006,** *8* (2), 364-368.

225.	Howlett, P. C.; Brack, N.; Hollenkamp, A. F.; Forsyth, M.; MacFarlane, D. R., Characterization of the lithium surface in N-Methyl-N-alkylpyrrolidinium bis(trifluoromethanesulfonyl)amide room-temperature ionic liquid electrolytes. *Journal of The Electrochemical Society* **2006,** *153* (3).

226.	Kaneko, F.; Wada, S.; Nakayama, M.; Wakihara, M.; Koki, J.; Kuroki, S., Capacity fading mechanism in all solid-state lithium polymer secondary batteries using PEG-borate/aluminate ester as plasticizer for polymer electrolytes. *Advanced Functional Materials* **2009,** *19* (6), 918-925.

227.	Haber, S.; Leskes, M., What can we learn from solid state NMR on the electrode-electrolyte interface? *Adv Mater* **2018,** *30* (41), e1706496.

228.	Pecher, O.; Carretero-González, J.; Griffith, K. J.; Grey, C. P., Materials' methods: NMR in battery research. *Chemistry of Materials* **2016,** *29* (1), 213-242.

229.	Li, N. W.; Shi, Y.; Yin, Y. X.; Zeng, X. X.; Li, J. Y.; Li, C. J.; Wan, L. J.; Wen, R.; Guo, Y. G., A flexible solid electrolyte interphase layer for long-life lithium metal anodes. *Angew Chem Int Ed Engl* **2018,** *57* (6), 1505-1509.

230.	Choi, U.; Runt, J., Structures in ion-containing polymers. *Encyclopedia of Polymeric Nanomaterials* **2015**, 2345-2351.

231.	Cullity, B. D., *Elements of X-ray Diffraction*. Addison-Wesley Publishing: 1956.

232.	Mai, Y.; Eisenberg, A., Self-assembly of block copolymers. *Chem Soc Rev* **2012,** *41* (18), 5969-5985.

233.	Bates, F. S.; Fredrickson, G. H., Block copolymers—designer soft materials. *Physics Today* **1999,** *52* (2), 32-38.

146

234. Glatter, O.; Kratky, O., *Small angle X-ray scattering*. Academic Press: New York: 1982.

235. Percus, J. K.; Yevick, G. J., Analysis of classical statistical mechanics by means of collective coordinates. *Physical Review* **1958,** *110* (1), 1.

236. Kinning, D. J.; Thomas, E. L., Hard-sphere interactions between spherical domains in diblock copolymers. *Macromolecules* **1984,** *17* (9), 1712-1718.

237. Han, K. S.; Wang, X.; Dai, S.; Hagaman, E. W., Distribution of 1-butyl-3-methylimidazolium bistrifluoromethylsulfonimide in mesoporous silica as a function of pore filling. *The Journal of Physical Chemistry C* **2013,** *117* (30), 15754-15762.

A1. Materials and Synthesis Scheme for PIL Diblock Copolymers

A1.1 Materials

2-cyanobutanyl-2-yl 3,5-dimethyl-1H-pyrazole-1-carbodithioate (chain transfer agent (CTA), ≥95%, Boron Molecular), tetrahydrofuran (THF, anhydrous, ≥99.9%, inhibitor-free, Sigma-Aldrich), tetrahydrofuran (HPLC THF, inhibitor-free, for HPLC, ≥99.9%, Sigma-Aldrich), chloroform-d (CDCl$_3$, 99.96 atom % D , Sigma-Aldrich), dimethyl sulfoxide-d$_6$ (DMSO-d$_6$, 99.96 atom % D, Sigma-Aldrich), *N*-methylimidazole (≥99%, purified by redistillation, Sigma-Aldrich), *N*-methylpyrrolidine (≥98% (GC), Sigma-Aldrich), *N,N*-dimethylformamide (DMF, anhydrous, 99.8%, Sigma-Aldrich), bis(trifluoromethane)sulfonimide lithium salt (Li-TFSI, 99.95%, trace metal basis, Sigma-Aldrich), lithium bis(fluorosulfonyl)imide (Li-FSI, >98%, TCI America), hexane (anhydrous, 95%, Sigma-Aldrich), acetone (ACS reagent, ≥99.5%, Sigma-Aldrich), and methanol (MeOH, ACS reagent, ≥99.8%, Sigma-Aldrich) were used as received. 1,1'-azobis(cyclohexanecarbonitrile) (Vazo-88, 98%, Sigma-Aldrich) was purified *via* recrystallization twice from methanol. Styrene (S, ≥99%, contains 4-*tert*-butylcatechol as stabilizer, Sigma-Aldrich) and vinylbenzyl chloride (VBC, mixture of 3- and 4-isomers, 97%, contains 700-1000 ppm nitromethane as inhibitor, 50-100 ppm *tert*-butylcatechol as inhibitor, Sigma-Aldrich) were purified by passing dropwise through a hollow glass tube packed with aluminum oxide (Sigma-Aldrich). Ultrapure deionized (DI) water was used as appropriate.
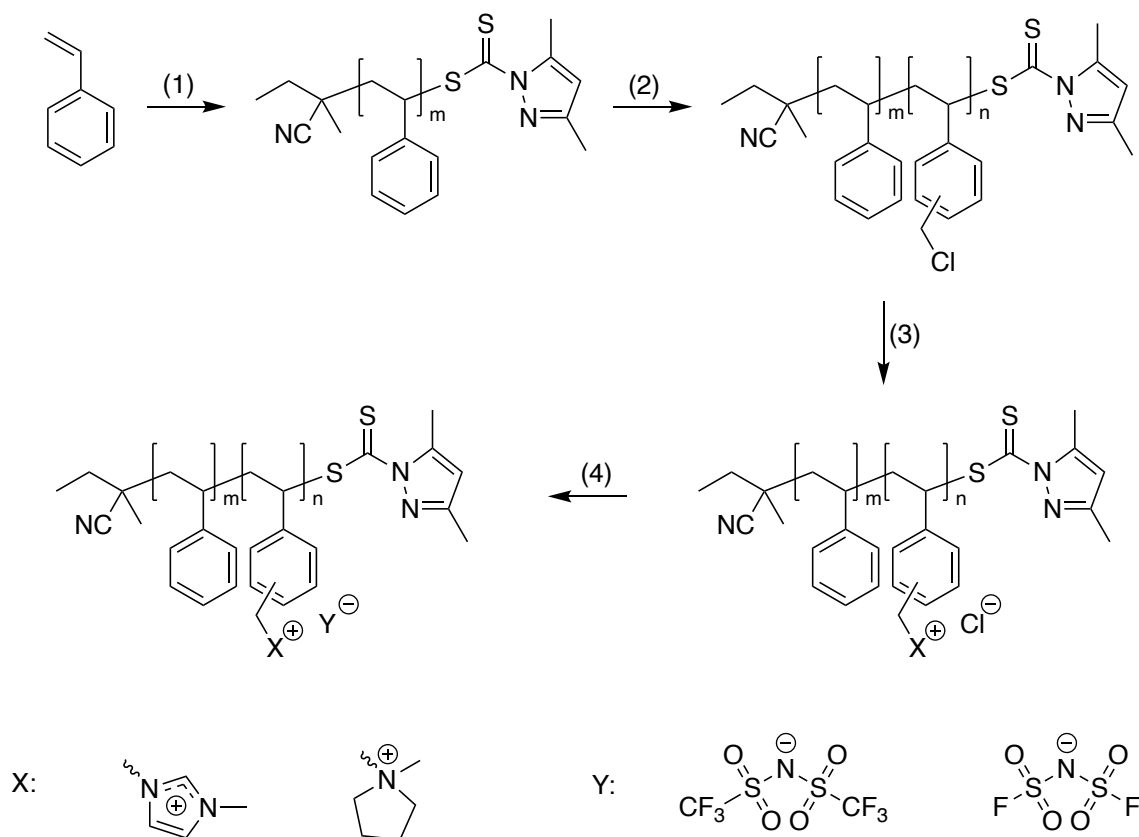
Figure A1. Synthesis of PIL diblock copolymers: (1) 2-cyanobutanyl-2-yl 3,5-dimethyl-1H-pyrazole-1-carbodithioate, Vazo-88, THF, reflux, 22 h; (2) vinylbenzyl chloride, Vazo-88, THF, reflux, 5 h; (3) n-methylimidazole or n-methylpyrrolidine, DMF, 80 °C, 48 h; (4) Li-TFSI or Li-FSI, DMF, 50 °C, 48 h.

A2. Synthesis of PS Macro-CTA

The synthesis of poly(styrene) (PS) macro-chain transfer agent (Macro-CTA) is shown in Figure A1(1). 260.8916 g (2504.9 mmol) of styrene and 5.0048 g (197.5 mmol) of CTA were mixed with 250.3548 g of THF in a 1000 mL three-neck round-bottom-flask, where the central neck of the flask was connected to a reflux column (connected to a bubbler and a nitrogen source from a Schlenk line) and the other two necks of the flask were sealed with rubber septa. The reacting mixture was degassed by bubbling nitrogen gas through

the mixture for 1 h. After degassing, the reactor was placed into an oil bath, covered in aluminum foil, and heated to reflux. In a separate 10 mL vial sealed with a septum, 0.4857 g (19.8 mmol) of Vazo-88 was dissolved into 5.1928 g of THF and degassed by bubbling nitrogen gas through the solution for 5 min. At the first sign of reflux, the degassed Vazo-88 solution was injected into the reacting mixture. The reaction was performed under reflux for 22 h. The resulting polymer was twice precipitated into methanol, filtered, and then dried under dynamic vacuum in an oven at room temperature for 24 h. Yield: 112.86 g of yellow powder (95.25% yield). ^{1}H NMR (400 MHz, CDCl$_3$, 23 °C) δ (ppm): 7.22-6.28 (m, 5H, C$_6$H$_5$), 2.40-1.66 (m, 1H, CH$_2$CH), 1.66-1.12 (m, 2H, CH$_2$CH) (^{1}H NMR, Figure A3(IV)); SEC (THF, 40 °C): M$_n$ = 4,534 Da, M$_w$/M$_n$ = 1.16 (against PS standards) (SEC, Figure A2).

A3. Synthesis of Diblock Copolymer Poly(S-*b*-VBC)

The synthesis of diblock copolymer poly(S-*b*-VBC) is shown in Figure A1(2). 50.4893 g (330.8 mmol) of VBC and 15.0018 g (3.3 mmol) of PS Macro-CTA were mixed with 50.0078 g of THF in a 500 mL three-neck round-bottom-flask, where the central neck of the flask was connected to a reflux column (connected to a bubbler and a nitrogen source from a Schlenk line) and the other two necks of the flask were sealed with rubber septa. The reacting mixture was degassed by bubbling nitrogen gas through the mixture for 30 min. After degassing, the reactor was placed into an oil bath, covered in aluminum foil, and heated to reflux. In a separate 10 mL vial sealed with a septum, 0.1627 g (0.7 mmol) of Vazo-88 was dissolved into 0.5016 g of THF and degassed by bubbling nitrogen gas

through the solution for 5 min. At the first sign of reflux, the degassed Vazo-88 solution was injected into the reacting mixture. The reaction was performed under reflux for 22 h. The resulting polymer was twice precipitated into methanol, filtered, and then dried under dynamic vacuum in an oven at room temperature for 24 h. Yield: 31.2392 g of yellow powder (85.09% yield). ^{1}H NMR (400 MHz, CDCl$_3$, 23 °C) δ (ppm): 7.22-6.28 (m, 9H, C$_6$$H_5$ & C$_6$$H_4$), 4.66-4.08 (m, 2H, C$H_2$Cl), 2.40-1.66 (m, 1H, CH$_2$CH), 1.66-1.12 (m, 2H, CH_2CH) (^{1}H NMR, Figure A3(III)); SEC (THF, 40 °C): M$_n$ = 8,054 Da, M$_w$/M$_n$ = 1.24 (against PS standards) (SEC, Figure A2)

A4. Synthesis of PIL Diblock Copolymer Poly(S-*b*-VBMIm-Cl)

The synthesis of PIL diblock copolymer poly(S-*b*-VBMIm-Cl) is shown in Figure A1(3). 10.0897 g (0.9 mmol) of poly(S-*b*-VBC) and 15.5572 g (189.5 mmol) of *N*-methylimidazole were dissolved into ~40 mL of DMF in a 125 mL flask which was subsequently sealed with a rubber septum. The sealed flask was then placed into an oil bath at 80 °C and left to stir for 48 h. The resulting polymer was precipitated into hexane, then washed extensively in hexane, then washed extensively in acetone, then dried under dynamic vacuum in an oven at room temperature for 24 h. Yield: 12.3049 g of solid particles (93.12% yield). ^{1}H NMR (400 MHz, CDCl$_3$, 23 °C) δ (ppm): 10.37-9.46 (s, 1H NCHN), 8.28-7.58 (m, 2H, NCHCHN), 7.58-5.95 (m, 9H, C$_6$$H_5$ & C$_6$$H_4$), 5.82-4.97 (m, 2H, C$H_2$N), 4.22-3.64 (s, 3H, NC$H_3$), 2.42-1.71 (m, 1H, CH$_2CH$), 1.71-0.61 (m, 2H, C$H_2$CH) (^{1}H NMR, Figure A3(II)).

A5. Synthesis of PIL Diblock Copolymer Poly(S-*b*-VBMPyr-Cl).

The synthesis of PIL diblock copolymer poly(S-*b*-VBMPyr-Cl) is shown in Figure A1(3). 7.0059 g (0.6 mmol) of poly(S-*b*-VBC) and 11.5421 g (135.6 mmol) of *N*-methylpyrrolidine were dissolved in ~28 mL of DMF in a 125 mL flask which was subsequently sealed with a rubber septum. The sealed flask was then placed into an oil bath at 80 °C and left to stir for 48 h. The resulting polymer was precipitated into hexane, then washed extensively with hexane, then washed extensively with acetone, then dried under dynamic vacuum in an oven at room temperature for 24 h. Yield: 8.7241 g of solid particles (94.25% yield). ^{1}H NMR (400 MHz, CDCl$_3$, 23 °C) δ (ppm): 7.82-5.98 (m, 9H, C$_6$*H*$_5$ & C$_6$*H*$_4$), 5.39-4.30 (m, 2H, C*H*$_2$N), 3.91-3.14 (m, 4H, NC*H*$_2$CH$_2$CH$_2$C*H*$_2$N), 3.14-2.62 (s, 3H, NC*H*$_3$), 2.32-1.96 (m, 4H, NCH$_2$C*H*$_2$C*H*$_2$CH$_2$N), 1.96-1.70 (m, 1H, CH$_2$C*H*), 1.70-0.61 (m, 2H, C*H*$_2$CH) (^{1}H NMR, Figure A3(I)).

A6. Synthesis of PIL Diblock Copolymer Poly(S-*b*-VBMIm-TFSI)

The synthesis of PIL diblock copolymer poly(S-*b*-VBMIm-TFSI) is shown in Figure A1(4). 7.0043 g (0.5 mmol) of poly(S-*b*-VBMIm-Cl) and 29.01 g (101.0 mmol) of Li-TFSI were dissolved in ~45 mL of DMF in a 125 mL flask, which was subsequently sealed with a rubber septum. The sealed flask was then placed into an oil bath at 50 °C and left to stir for 48 h. The resulting polymer was precipitated into a methanol/DI water mixture (50/50 (v/v)), then washed extensively with DI water, then dried under dynamic vacuum in an oven at room temperature for 24 h. Yield: 9.9324 g of solid particles (83.18% yield). ^{1}H NMR (400 MHz, CDCl$_3$, 23 °C) δ (ppm): 9.32-8.96 (s, 1H NC*H*N), 7.77-7.31 (m, 2H,

NC*HCH*N), 7.31-5.90 (m, 9H, C$_6$*H*$_5$ & C$_6$*H*$_4$), 5.41-4.72 (m, 2H, C*H*$_2$N), 4.03-3.55 (s, 3H, NC*H*$_3$), 2.23-1.71 (m, 1H, CH$_2$C*H*), 1.71-0.61 (m, 2H, C*H*$_2$CH) ([^{1}]H NMR, Figure A4(IV)). Elemental analysis (EA) calculated: C, 47.57; H, 4.01; N, 7.26; S, 11.09; F, 19.26; Cl, 0.00. Found: C, 48.40; H, 4.06; N, 7.11; S, 10.99; F, 18.94; Cl, 0.00.

A7. Synthesis of PIL Diblock Copolymer Poly(S-*b*-VBMIm-FSI)

The synthesis of PIL diblock copolymer poly(S-*b*-VBMIm-FSI) is shown in Figure A1(4). 3.0213 g (0.2 mmol) of poly(S-*b*-VBMIm-Cl) and 7.868 g (42.1 mmol) of Li-FSI were dissolved in ~15 mL of DMF in a 40 mL vial. The sealed vial was then placed into an oil bath at 50 °C and left to stir for 48 h. The resulting polymer was precipitated into a methanol/DI water mixture (50/50 (v/v)), then washed extensively with DI water, then dried under dynamic vacuum in an oven at room temperature for 24 h. Yield: 3.8769 g of solid particles (90.81% yield). ^{1}H NMR (400 MHz, CDCl$_3$, 23 °C) δ (ppm): 9.42-8.96 (s, 1H NC*H*N), 7.79-7.33 (m, 2H, NC*HCH*N), 7.33-5.90 (m, 9H, C$_6$*H*$_5$ & C$_6$*H*$_4$), 5.39-4.83 (m, 2H, C*H*$_2$N), 4.11-3.56 (s, 3H, NC*H*$_3$), 2.22-1.71 (m, 1H, CH$_2$C*H*), 1.71-0.61 (m, 2H, C*H*$_2$CH) ([^{1}]H NMR, Figure A4(III)). Elemental analysis (EA) calculated: C, 52.36; H, 4.82; N, 8.74; S, 13.34; F, 7.73; Cl, 0.00. Found: C, 53.16; H, 4.95; N, 8.46; S, 12.82; F, 7.59; Cl, 0.00.

A8. Synthesis of PIL Diblock Copolymer Poly(S-*b*-VBMPyr-TFSI)

The synthesis of PIL diblock copolymer poly(S-*b*-VBMPyr-TFSI) is shown in Figure A1(4). 3.0259 g (0.2 mmol) of poly(S-*b*-VBMPyr-Cl) and 12.3225 g (42.9 mmol) of Li-

TFSI were dissolved in ~19 mL of DMF in a 40 mL vial. The sealed vial was then placed into an oil bath at 50 °C and left to stir for 48 h. The resulting polymer was precipitated into a methanol/DI water mixture (50/50 (v/v)), then washed extensively in DI water, then dried under dynamic vacuum in an oven at room temperature for 24 h. Yield: 4.7614 g of solid particles (91.83% yield). ^{1}H NMR (400 MHz, CDCl$_3$, 23 °C) δ (ppm): 7.49-6.05 (m, 9H, C$_6$*H*$_5$ & C$_6$*H*$_4$), 4.67-3.88 (m, 2H, C*H*$_2$N), 3.67-2.91 (m, 4H, NC*H*$_2$CH$_2$CH$_2$C*H*$_2$N), 2.91-2.42 (s, 3H, NC*H*$_3$), 2.42-1.92 (m, 4H, NCH$_2$C*H*$_2$C*H*$_2$CH$_2$N), 1.92-1.71 (m, 1H, CH$_2$C*H*), 1.71-0.61 (m, 2H, C*H*$_2$CH) (^{1}H NMR, Figure A4(II)). Elemental analysis (EA) calculated: C, 49.26; H, 5.00; N, 4.86; S, 11.01; F, 19.13; Cl, 0.00. Found: C, 49.86; H, 5.00; N, 4.75; S, 10.87; F, 19.31; Cl, 0.00.

A9. Synthesis of PIL Diblock Copolymer Poly(S-*b*-VBMPyr-FSI)

The synthesis of PIL diblock copolymer poly(S-*b*-VBMPyr-FSI) is shown in Figure A1(4). 3.0017 g (0.2 mmol) of poly(S-*b*-VBMPyr-Cl) and 8.0121 g (42.8 mmol) of Li-FSI were dissolved in ~19 mL of DMF in a 40 mL vial. The sealed vial was then placed into an oil bath at 50 °C and left to stir for 48 h. The resulting polymer was precipitated into a methanol/DI water mixture (50/50 (v/v)), then washed extensively in DI water, then dried under dynamic vacuum in an oven at room temperature for 24 h. Yield: 3.8734 g of solid particles (91.32% yield). ^{1}H NMR (400 MHz, CDCl$_3$, 23 °C) δ (ppm): 7.41-6.13 (m, 9H, C$_6$*H*$_5$ & C$_6$*H*$_4$), 4.58-3.95 (m, 2H, C*H*$_2$N), 3.66-2.92 (m, 4H, NC*H*$_2$CH$_2$CH$_2$C*H*$_2$N), 2.92-2.35 (s, 3H, NC*H*$_3$), 2.35-1.92 (m, 4H, NCH$_2$C*H*$_2$C*H*$_2$CH$_2$N), 1.92-1.71 (m, 1H, CH$_2$C*H*), 1.71-0.61 (m, 2H, C*H*$_2$CH) (^{1}H NMR, Figure A4(I)). Elemental analysis (EA)

calculated: C, 54.35; H, 6.00; N, 5.85; S, 13.23; F, 7.66; Cl, 0.00. Found: C, 55.13; H, 5.75; N, 5.64; S, 12.89; F, 7.47; Cl, 0.00.

A10. SEC Chromatograms for PS Macro-CTA and poly(S-*b*-VBC)
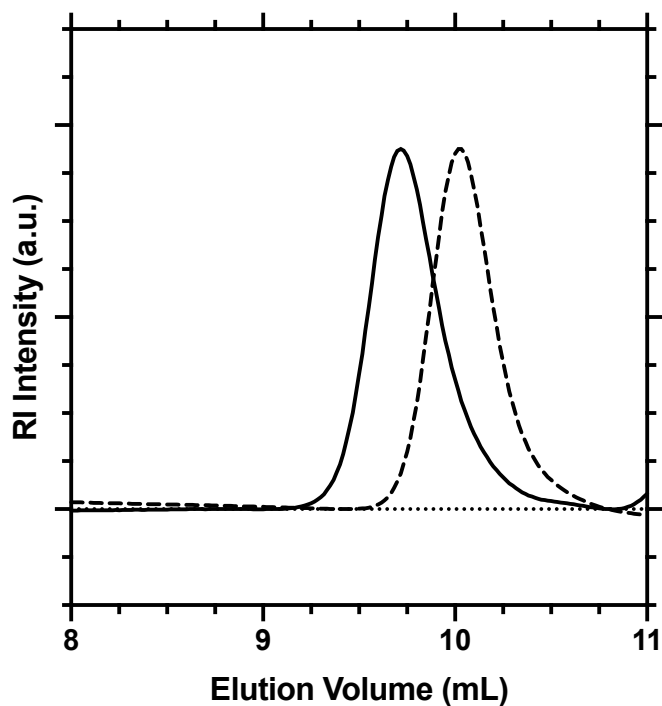

Figure A2. SEC chromatograms for PS Macro-CTA (dash line) and poly(S-*b*-VBC) (solid line) *versus* time. Chromatograms have been scaled for easier comparison**.**

The molecular weights and molecular weight distributions of PS Macro-CTA and poly(S-*b*-VBC) were determined by size exclusion chromatography (SEC) using a Waters Gel Permeation Chromatography (GPC) system equipped with a THF Styragel column (Styragel@HR 5E, effective separation of molecular weight range: 2-4000 kg mol^{-1}) and a 2414 reflective index (RI) detector. All measurements were performed at 40 °C, where

THF was used as the mobile phase at a flow rate of 1.0 mL min^{-1}. PS standards (Shodex, Japan) with molecular weights ranging from 2.97 to 983 kg mol^{-1} were used for calibration. Figure A2 shows the SEC chromatogram profiles for PS Macro-CTA and poly(S-*b*-VBC). Molecular weights and dispersities were calculated and are listed in the corresponding synthesis sections for each polymer. PS Macro-CTA molecular weight corresponds to 44 repeat units of styrene. The peak of the SEC chromatogram for poly(S-*b*-VBC) occurs at an earlier elution volume than the peak of the SEC chromatogram for PS Macro-CTA, indicating an increase in molecular weight. The breadth of both peaks is narrow, indicating low dispersity values and well-controlled RAFT polymerization. SEC chromatograms are not available for any charged polymers.

A11. ^{1}H NMR of poly(S-*b*-VBMPyr-Cl), poly(S-*b*-VBMIm-Cl), poly(S-*b*-VBC), and PS Macro-CTA

(I) poly(S-*b*-VBMPyr-Cl)

(II) poly(S-*b*-VBMIm-Cl)

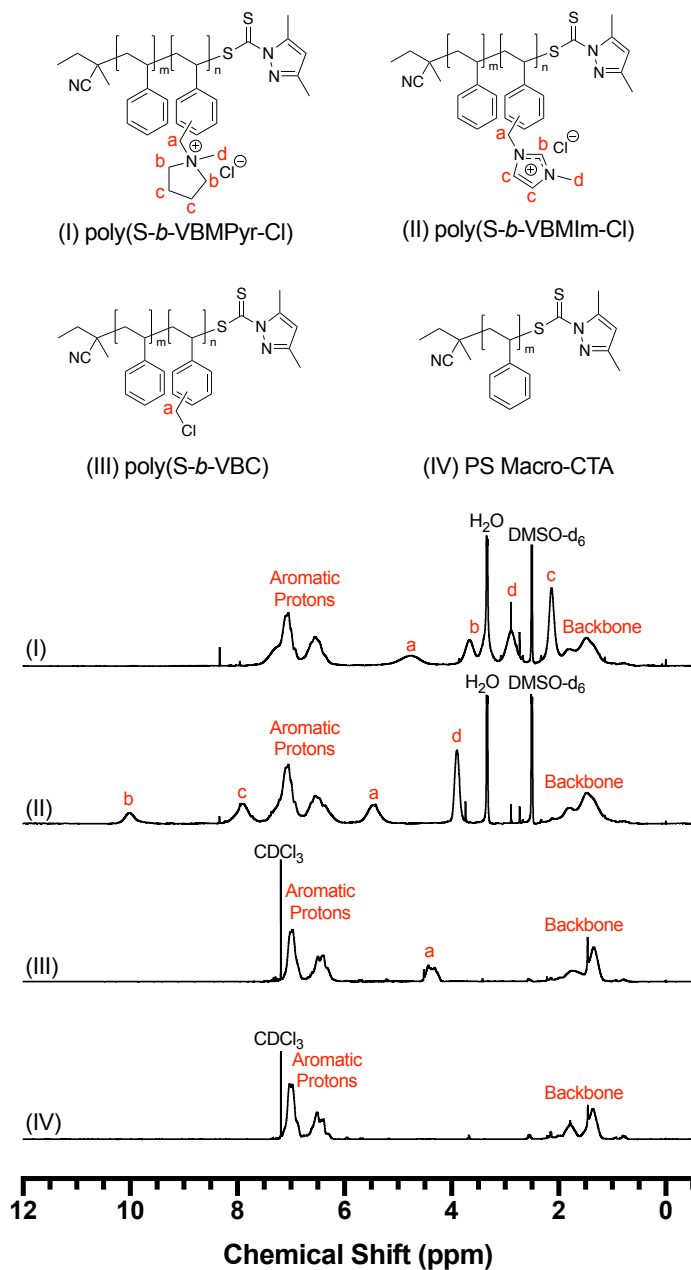(III) poly(S-*b*-VBC)

(IV) PS Macro-CTA

Figure A3. ^{1}H NMR spectra and peak assignments of all precursor polymers: (I) poly(S-*b*-VBMPyr-Cl), (II) poly(S-*b*-VBMIm-Cl), (III) poly(S-*b*-VBC), and (IV) PS Macro-CTA. The H$_2$O and DMSO-d$_6$ peaks in spectra (I) and (II) have been cut to improve the visibility of all other peaks

157

Chemical structures of all polymers were characterized by ^{1}H NMR (Nuclear Magnetic Resonance) Spectroscopy using a Bruker Avance 400 MHz spectrometer at 23 °C. PS Macro-CTA and poly(S-*b*-VBC) used $CDCl_3$ as the solvent with chemical shifts referenced to chloroform at 7.27 ppm. All ionic polymers used DMSO-d_6 as the solvent with chemical shifts referenced to DMSO at 2.50 ppm. Elemental Analysis (EA) was performed by Atlantic Microlab (Norcross, GA, USA). Figure A3 shows the ^{1}H NMR spectra of all precursor polymers used to synthesize the final polymerized ionic liquid block copolymers in this study. Specific peak assignments are listed in the corresponding synthesis section for each polymer. Broad ^{1}H NMR peaks are common in spectra of polymers. In all spectra except the spectra of PS Macro-CTA (Figure A3 (IV)), peak a represents the protons on the carbon in the 3 or 4 position of the benzene ring on the VBC block. The integration ratio between the aromatic peaks and peak a gives a polymer composition of 44 repeat units of styrene and 43 repeat units of the VBC based block. Peak shifts from 4.66-4.08 ppm in the spectra for poly(S-*b*-VBC) (Figure A3 (III)) to 5.82-4.97 ppm in the spectra for poly(S-*b*-VBMIm-Cl) (Figure A3(II)) indicating functionalization of the *N*-methylimidazole occurs. Additionally, the integration ratio between the aromatic protons and peaks a, b, c, and d all indicate 100% functionalization to poly(S-*b*-VBMIm-Cl). Peak shifts from 4.66-4.08 ppm in the spectra of poly(S-*b*-VBC) (Figure A3(III)) to 5.39-4.30 ppm in the spectra for poly(S-*b*-VBMPyr-Cl) (Figure A3(I)), indicating functionalization of the *N*-methylpyrrolidine occurs. The integration ratio between aromatic protons and peaks a, b, c, and d all indicate 100% functionalization to poly(S-*b*-VBMPyr-Cl).

158

A12. **[1]H** **NMR** **of** **poly(S-*b*-VBMPyr-FSI),** **poly(S-*b*-VBMPyr-TFSI),** **poly(S-*b*-VBMIm-FSI), and poly(S-*b*-VBMIm-TFSI).**
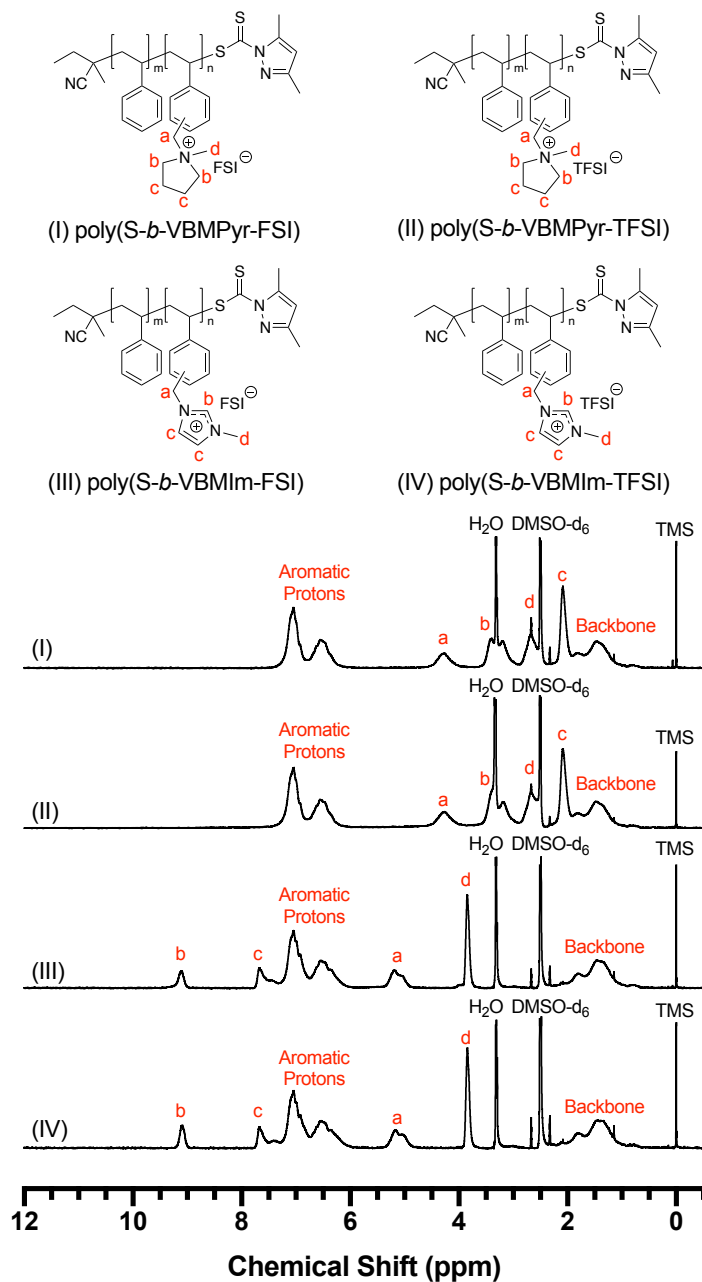

Figure A4. ^{1}H NMR spectra and peak assignments of all final polymers: (I) poly(S-*b*-VBMPyr-FSI), (II) poly(S-*b*-VBMPyr-TFSI), (III) poly(S-*b*-VBMIm-FSI), and (IV) poly(S-*b*-VBMIm-TFSI). The H_2O and DMSO-d_6 peaks in all spectra have been cut to improve the visibility of all other peaks.

Figure A4 shows the ^{1}H NMR spectra of all final polymerized ionic liquid block copolymers in this study. Specific peak assignments are listed in the corresponding synthesis section for each polymer. Broad ^{1}H NMR peaks are common in spectra of polymers. Slight shifts in peaks a, b, c, and d of all Figure A4 spectra relative to the peak positions of the precursors (Figure A3(I) and Figure A3(II)) indicate successful ion exchange. Elemental analysis results for each polymer (listed in the corresponding synthesis section) confirm 100% ion exchange to the TFSI and FSI forms.

APPENDIX B

B1. Calculations of PIL Pentablock Terpolymer and SPE Volume Fractions

The volume fractions corresponding to the PIL composition in pentablock terpolymers are calculated by the equation

$$\phi_{PIL} = x_{PIL} \frac{MW_{IL}}{MW_{cp}} \frac{\rho_{cp}}{\rho_{IL}} \tag{B1.1}$$

where x_{PIL} is the PIL composition (mole fraction) in the PIL pentablock terpolymer determined from theoretical molecular weight, MW_{cp} is the average molecular weight of the repeat unit of the copolymer, and MW_{IL} is the molecular weight of IL monomeric unit ($MW_{VBMIm-TFSI} = 479.42$ g mol^{-1}). The ρ_{cp} is the density of the copolymer, which is given by

$$\frac{1}{\rho_{cp}} = \frac{w_{PS}}{\rho_{PS}} + \frac{w_{E/P}}{\rho_{E/P}} + \frac{w_{IL}}{\rho_{IL}} + \frac{w_{E/P}}{\rho_{E/P}} + \frac{w_{PS}}{\rho_{PS}} \tag{B1.2}$$

where w_S , $w_{E/p}$, and w_{IL} are the weight fraction of polystyrene, poly(ethylene-r-propylene), and PIL, respectively; and ρ_{PS}, $\rho_{E/P}$, and ρ_{IL} are the densities of polystyrene ($\rho_{PS} = 1.04$ g cm^{-3}), poly(ethylene-r-propylene) ($\rho_{E/P} = 0.9$ g cm^{-3}), and PIL. The ρ_{IL} were estimated from the work done by Shreeve *et al.*[103] with $\rho_{VBMIm-TFSI} = 1.447$ g mol^{-1}. In this study, the calculated PILPTP density, $\rho_{cp} = 1.338$ g mol^{-1}.

The conducting phase volume fraction (*i.e.*, volume fraction of PIL block + IL + salt) was calculated by the method described in ref [114]:

$$\phi_c = \frac{\frac{W_{salt}}{W_{cp}} \frac{\rho_{cp}}{\rho_{salt}} + \frac{W_{IL} \rho_{cp}}{W_{cp} \rho_{IL}} \phi_{PIL}}{1 + \frac{W_{salt}}{W_{cp}} \frac{\rho_{cp}}{\rho_{salt}} + \frac{W_{IL} \rho_{cp}}{W_{cp} \rho_{IL}}} \tag{B1.3}$$

where ρ_{salt} and ρ_{IL} are the density of lithium salt ($\rho_{Li-TFSI}$ = 1.33 g cm⁻³) and IL ($\rho_{EMIm-TFSI}$ = 1.52 g cm⁻³). W_{salt}, W_{IL}, and W_{cp} are lithium salt, IL and block copolymer weights in the electrolyte, respectively. ϕ_{PIL} is the PIL volume fraction calculated from Equation B1.1.

B2. Small Angle X-ray Scattering Characterization

Figure B1 shows the SAXS data after background corrections and scales vertically for clarity. The y-axis is on an absolute intensity scale (cm^{-1}) for reference. All the samples show a strong scattering maximum, located at $q^* \approx 0.02$ Å^{-1}, with multiple higher-ordered features at higher angles and the intensity decreases to a flat background before increasing slightly at the highest q. The increase intensity of high-q is close to the leading edge of a "polymerization peak" resulting from interchain scattering.[230]
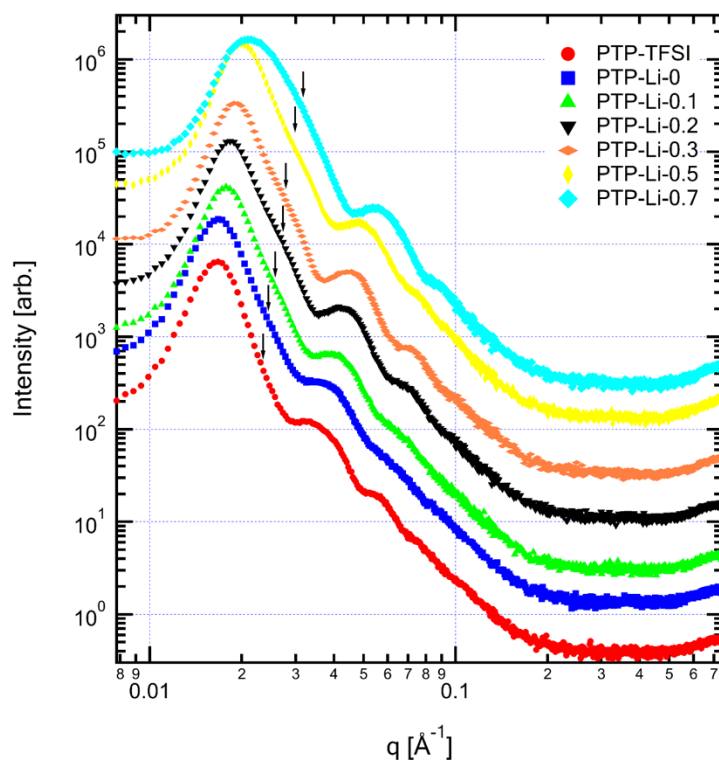

Figure B1. Combined SAXS data, showing strong form factor scattering, as well as a strong Bragg diffraction maximum. Arrows indicate the calculated position of the second Bragg diffraction peak from a body-centered cubic (BCC) structure.

To successfully fit the data, one assumed all the features were Bragg diffraction maxima. The positions and shapes of the higher order features do not correspond to those known morphologies of microphase separated block copolymers. However, samples with r = 0.2, 0.3, and 0.5 show a shoulders on their primary diffraction maxima that correspond well to the predicted position of the second Bragg peak from a body-centered cubic (BCC) structure.[231] The BCC structure is a common morphology for well-defined block copolymers having a minority component volume fraction, ϕ, of roughly 0.2, depending on a number of factors including the degree of immiscibility between blocks and molecular weights.[232-233] In present study, the organization of the microphase separated block copolymer domains would be best characterized as weak-ordered, but suggestive of a BCC structure. Table B1 lists both domain spacing, $d^* = 2\pi/q^*$ and the BCC lattice constant, a under room temperature for each sample.

In the absence of a strong fit by using Bragg diffraction, the data were fit using combinations of form and structure factors.[234] Based on the volume fraction of polystyrene (PS) in the samples (*i.e.*, $\phi_{PS} \approx 0.25$, from Table 4.2), the data were fit using form factors for either PS spheres or PS cores with thin poly(ethylene-*r*-propylene) (PEP) shells in a matrix of PIL and PIL/IL/salt. Satisfactory fits to the higher order fringes were obtained using both form factors for PTP-TFSI and PTP-Li-0 samples. In the case of PTP-Li-r samples, the core-shell form factor returned a PEP shell with thickness of zero. These results agree with the composition of PTP-TFSI polymer that the PEP block has a relatively smaller M_n compared to the PS and PIL blocks (2 to 20 and 44 kg mol^{-1}, respectively). Both the Percus-Yevick hard-sphere structure factor and Zernike-Prins

structure factor were combined with the best form factor fits, but were unable to reproduce the sharp primary scattering maximum.[235-236] This is mostly likely due to the further organization of PS spheres into a weak cubic lattice. Table B1 lists the PS sphere radius and standard deviations obtained using a sphere form factor.

Table B1. SAXS Analysis from Figure B1.

Sample	[a] d* (Å)	[b] a (Å)	Sphere Radius (Å)
PTP-TFSI	378	534	165 ± 15.9
PTP-Li-0	373	528	146 ± 20.8
PTP-Li-0.1	352	498	138 ± 18.8
PTP-Li-0.2	341	483	131 ± 16.1
PTP-Li-0.3	328	464	126 ± 14.9
PTP-Li-0.5	312	441	113 ± 14.9
PTP-Li-0.7	293	415	100 ± 12.6

[a] domain spacing, $d^* = 2\pi/q^*$
[b] BCC lattice constant

Overall, the SAXS data strongly suggests a morphology of PS-PEP core-shell spheres on a poorly ordered BCC lattice.[190] This interpretation is supported by comparing the volume fractions of the conducting phase (*i.e.,* PIL + Li-TFSI + IL) and non-conducting phases (PS + PEP) derived from the SAXS analysis ($\phi_{conducting,SAXS}$ and $\phi_{PS+PEP,SAXS}$) with those calculated based on molecular weight and density data ($\phi_{conducting}$ and ϕ_{PS+PEP}, from Table 4.2) in Figure B2. The values calculated from the SAXS analysis track very closely with those calculated from the known composition of the samples, supporting the hypothesis that the morphology is PS-PEP domains on a roughly BCC lattice.
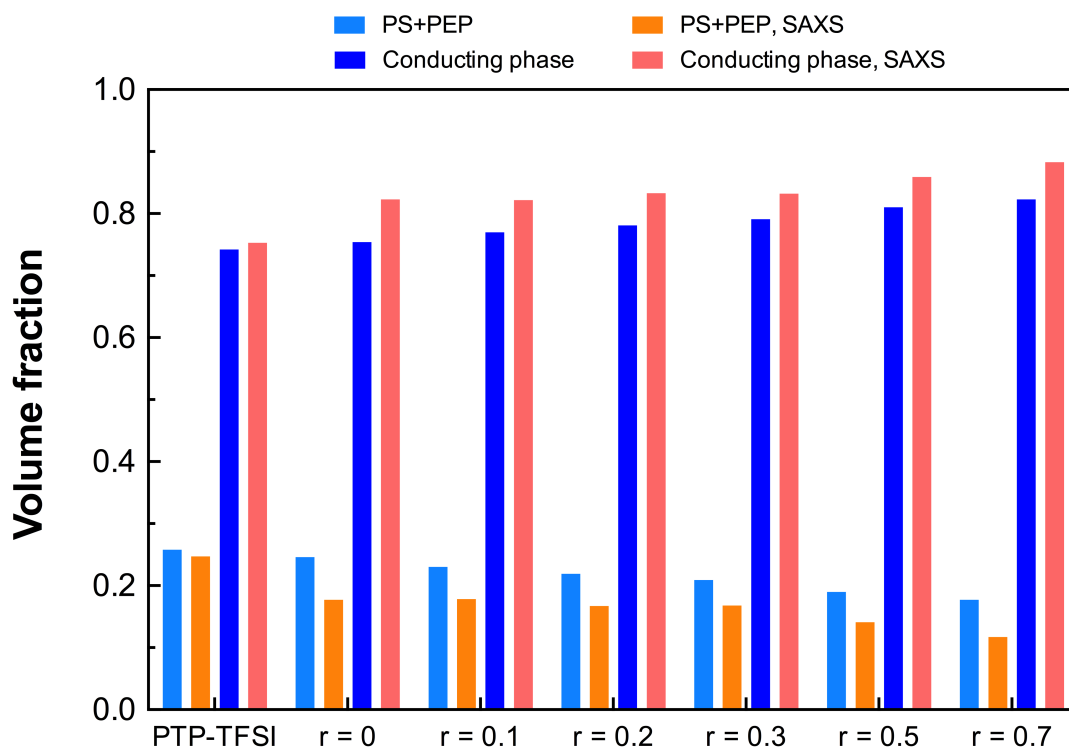
Figure B2. Comparison of volume fractions of conducting phase (PIL + Li-TFSI + IL) and non-conducting phase (PS + PEP) as derived from the SAXS data using a BCC lattice and the calculated volume fractions from the compositions in Table 2.

B3. Pulsed-Field Gradient Nuclear Magnetic Resonance (PFG-NMR) Characterization

The apparent diffusion coefficients, D_{app}, of Li^+, $EMIm^+$ and $TFSI^-$ ions confined in the PTP-Li-0.5 and PTP-Li-0.7 SPEs are obtained as a function of diffusion delay, Δ (Figure S3). D_{app} shows a gradual decrease and then became a plateau with the increase of Δ as similar to the diffusion of molecules confined in the pore of porous materials.[237] For PTP-Li-0.2, it is not possible to obtain Δ dependent D_{app} due to the limit of relaxation times. In PTP-Li-0.7, $D_{Li+} > D_{TFSI-}$ for all measured D_{app} and the restricted diffusion behavior is dominant on Li^+ and $TFSI^-$ compared with that of $EMIm^+$, suggesting that Li^+ and $TFSI^-$ ions are located closer to the polymer surface than $EMIm^+$. It is possible to estimate the geometry of the channel for ion diffusion as defined to the tortuosity, $T \equiv D_0/D_\infty$, where D_∞ is the steady state diffusion coefficient, which is equal to D_{app} at a plateau when $\Delta = \infty$. In PTP-Li-0.7, it shows $T = 6$ and 4 for Li^+ and $TFSI^-$, respectively; while in PTP-Li-0.5, $T = 5$ and 4 for Li^+ and $EMIm^+$, respectively. The larger T values obtained from Li^+ comparing with those from $TFSI^-$ and $EMIm^+$ suggesting that Li^+ ions are distributed more closer to the surface of polymer domain than $TFSI^-$ and $EMIm^+$ in these PILPTP solid electrolytes. Also, it shows the larger T in PTP-Li-0.7 comparing with that of PTP-Li-0.5 may due to the smaller domain spacing of PTP-Li-0.7 (Table B3). The diffusion coefficients in present study compared D_0 rather than D_∞ because the time as well as the spatial scale of relaxation measurement are much shorter than those of PFG-NMR measurement. The D_{TFSI-} estimated from the relaxation measurements is closer to D_0. All diffusion coefficients are D_0 except D_{TFSI-} for PTP-Li-0.2 and PTP-Li-0.5. The D_{TFSI-} for

PTP-Li-0.2 and PTP-Li-0.5 were determined from relaxation measurements. The D_0 of Li$^+$ and EMIm$^+$ for PTP-Li-0.2 were estimated based on the assumption that the variation of D_{app} in the early stage of Δ are similar with that shown in PTP-Li-0.5.
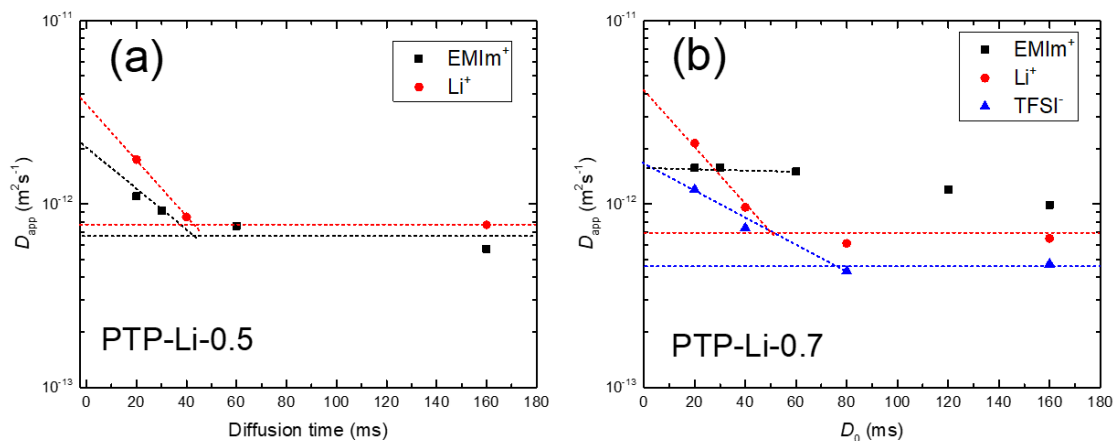

Figure B3. Apparent diffusion coefficients, D_{app} of Li$^+$, TFSI$^-$ and EMIm$^+$ obtained as a function of diffusion delay, Δ from (a) PTP-Li-0.5 and (b) PTP-Li-0.7. In (a) $D_{app,TFSI}$ is not available because the short ^{19}F relaxation times prohibit performing ^{19}F PFG-NMR in PTP-Li-0.5. D_0 where D_{app} at Δ=0 is determined from the extrapolation of the data. Both samples show D_0 of Li$^+$ is about twice of D_{app} at Δ = 20 ms.